University of Nevada, Reno

Numerical study of γ-ray production in ultra-intense laser - plasma interaction

A dissertation submitted in partial fulfillment
of the degree requirements for the degree of
PhD in Physics

by
Rishi R. Pandit

Dr. Yasuhiko Sentoku, Advisor

May 2015

ProQuest LLC.
789 East Eisenhower Parkway
P.O. Box 1346
Ann Arbor, MI 48106 - 1346

THE GRADUATE SCHOOL

We recommend that the dissertation
prepared under our supervision by

RISHI RAM PANDIT

Entitled

Numerical study of γ-ray production in ultra-intense laser - plasma interaction

be accepted in partial fulfillment of the
requirements for the degree of

DOCTOR OF PHILOSOPHY

Yasuhiko Sentoku, Ph.D., Advisor

Hiroshi Sawada, Ph.D., Committee Member

Radu Presura, Ph.D., Committee Member

Roberto C. Mancini, Ph.D., Committee Member

David M. Leitner, Ph.D., Graduate School Representative

David W. Zeh, Ph. D., Dean, Graduate School

May, 2015

Abstract

Recent advances in the development of intense short pulse lasers are significant. It is available now to access laser with intensity $\sim 10^{21}$ W/cm^2 by focusing a petawatt class laser, at which intensity hot dense plasmas with relativistic electrons, energy greater than 100 MeV, are produced. High energy x-rays, so called γ-rays, are emitted strongly from such plasmas via Bremsstrahlung.

In a few years the laser intensity is expected to exceed 10^{22} W/cm^2. In such extreme intense laser-matter interaction, the radiative damping is significant, namely, electrons accelerated by the laser fields lose their energies and emit γ-rays. So that we will see intense γ-ray flash from the laser produced plasmas via two competing processes, Bremsstrahlung and radiative damping. However It is not clearly understood which process is dominant at what laser or what target conditions. My research is focus on making the radiation models to understand the γ-ray emissions and studying the extremely intense laser-matter interaction to optimize the γ-ray emissions under the given laser and target conditions.

Since these relativistic plasmas are non-thermal and non-equilibriated, it is necessary to develop a kinetic plasma code with the radiation physics. We had developed a collisional particle-in-cell code, PICLS, coupled to a radiation transport module to consider the γ-ray emissions. The emissivities of γ-rays had been derived for the relativistic Bremsstrahlung and the radiative damping. In the radiative damping, especially, not only the first order damping term, but up to 4-th order damping terms had been derived from the Lorentz-Dirac equation for the first time. Especially, the 2nd term is found to be important since it is a damping term of the Lorentz force, indicating the particle acceleration including ions would be much less efficient than that what we expected when the laser intensity become greater than $10^{23}\,\mathrm{W/cm^2}$.

The laser energy dependence of the γ-ray energy and the intensity dependence of the angular distribution of γ-rays are studied. By solving the emission and transport of γ-ray it was found that the radiative damping is not significant until the laser intensity exceeds $10^{23}\,\mathrm{W/cm^2}$. While the Bremsstrahlung is dominant γ-rays emission process, which can also boost by changing the target with higher Z material or increasing the mass (volume) of the target. As an application of γ-ray production, the pair creation, forming a pair plasma, is attractive. The number of positrons via pair creation from the Bethe-

Heitler process is also computed in the code. The optimal parameters of laser and target to increase γ-ray yields as well as positrons yields are identified.

ACKNOWLEDGEMENT

First and foremost, I would like to express my profound gratitude to my advisor Dr. Yasuhiko Sentoku, for his support, patience, invaluable guidance and encouragement. I would like to express my sincere thanks to my committee members for their time, guidance and valuable suggestions: Dr. Hiroshi Sawada, (UNR Department of Physics), Dr. Radu Presura, (UNR Department of Physics), Dr. Roberto C. Mancini, (UNR Department of Physics) and Dr. David M. Leitner, (UNR Department of Chemistry). I would like to thank to all my instructors, professors, colleagues, friends and my families for their constant encouragement and support. I would like to thank Department of Physics and NTF administration for their support. I would like to thank my father Tulsi Prasad Pandit and my mother Krishna Maya Pandit for their help. I would like to thank my beloved wife Pratima Pandit, my daughter Prashika Pandit and my son Ritik Pandit for their constant help. Work Supported by US DOE OFES DE-SC0008827.

Contents

List of Figures

Chapter 1 Introduction

1.1 Progress of Laser Technology.

Lasers (an acronym of **L**ight **A**mplification by **S**timulated **E**mission of **R**adiation) emit amplified electromagnetic radiation with a monochromatic frequency. The range of that radiation from the long infrared region up through the visible region and extending to the ultraviolet and even to the X-ray region. There is a specific mechanism for laser amplification. After the invention of laser light in about 1960, intensity of lasers has been increasing day by day. Figure 1.1 represents the laser intensity versus the year [2]. There is a steep slope in intensities that occured during the 1960s. This period corresponded to the discovery of most nonlinear optical effects due to the bound electron. The rapid evolution in intensity was due to the introduction of Q-switching and mode locking. Q-switching is the technique by which a laser can be made to produce a pulsed output beam. Mode-locking is the technique in optics by which laser light can be made to produce pulses of light with a short duration(nano-second). During 1980s the chirped pulse amplification(CPA) technique had been introduced. Pulse dura-

tions have come down from a picosecond ($10^{-12}s$) to few femtoseconds ($10^{-15}s$); whereas focused intensities have increased by six orders of magnitudes. The CPA technique became capable of delivering intensities almost $10^5 - 10^6$ times higher than those available before the CPA technique. Plasma with very hot electrons is produced by the field. Electrons in plasma are accelerate and their energies become relativistic when the laser intensity is greater than 10^{18} W/cm^2. Such relativistic electrons produce potentially radiation as well as electron positron pairs, so called the positron-electron era. Now the highest laser intensity achieved is $\sim 10^{22}$ W/cm^2. ELI and ILE Apollon projects are still working to increase laser intensity. Hopefully, In a few years, laser intensity will exceed 10^{23} W/cm^2, thus the strong relativistic plasma will be formed.

1.2 Physics in Intense Laser Produced Dense Plasma

The interaction of high power laser radiation with matter results in the production of plasmas with extremely hot electrons (>100 MeV) as shown in figure 1.2 , where the quantum effects are important. Self consistent electric fields confine these electrons in the target in picoseconds time scale. Then the atomic processes such as collision, ionization and the radiation effects, i.e. Bremsstrahlung become very

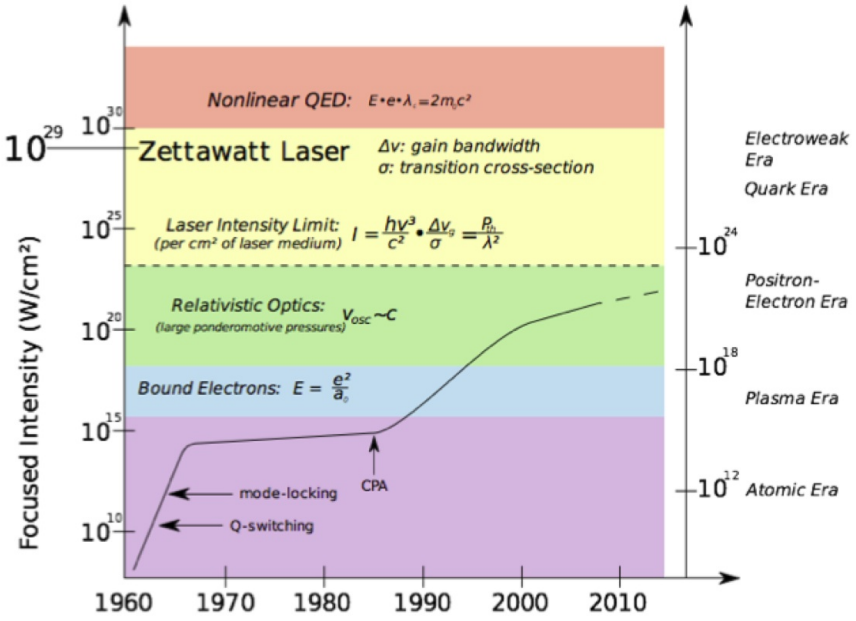

Figure 1.1: Progress of laser technology [2].

crucial. When relativistic electrons interact with the matter, electron-positron pairs are also produced which is known as pair production. Intense laser produced high energy density plasma are not equilibrated, the electrons excite plasma waves via kinetic instabilities so that the atomic processes, plasma instabilities, and radiations are competing to thermalize the plasma. In laser-plasma interaction, laser-plasma has a tremendous potential as a primary sources of photons, electrons and ions which can be used for other purposes [3]. They have the properties of compactness, high brightness, low emittance, short duration and so on. Applications of short-pulse laser-matter interactions include particle accelerators, fast ion sources, soft and hard x-ray sources, elec-

tron microscope, lithography, biomedical imaging [3]. It is crucial to understand the physics in the laser-plasma interaction to realize the applications mentioned above.

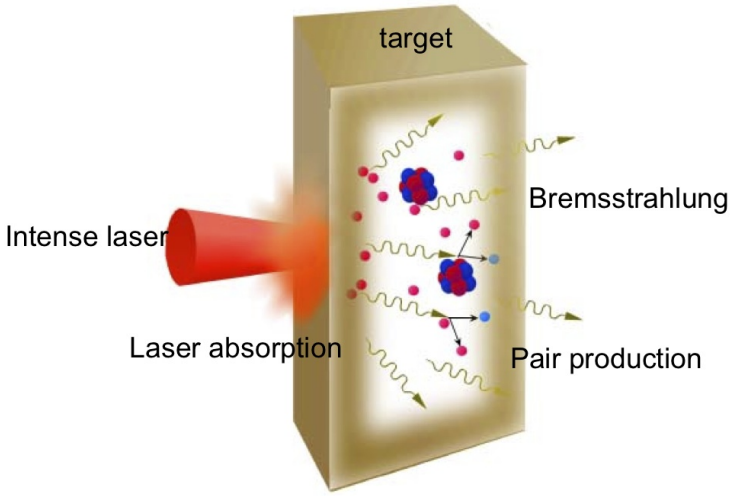

Figure 1.2: Laser plasma interaction.

1.3 Synchrotron radiation

In the development of particle accelerators there has been different types of accelerators developed. One of the most important particle accelerators is the synchrotron. It runs charged particles in a confined, near-circular path by means of magnetic fields. When charged particles are accelerated in a curved path or orbit by a magnetic field, they emit radiation which is known as synchrotron radiation. In this radiation, the accelerated charged particles emit electro-magnetic radiation. When a fast-moving charge, for example an electron, propagates

through magnetic field in space, the synchrotron radiation occurs naturally i.e. neutron star [4].

In the magnetic field, the electron's orbit is bent by the $\mathbf{v} \times \mathbf{B}$ force. The force is always perpendicular to the velocity, that is why the electron circles. Radiation is produced along the curved path continuously. The emission power depends on the strength of the magnetic field and the particle velocity.

In theoretical point of view, for a charge e with momentum $\mathbf{P}$ (here $\mathbf{P} = \gamma m \mathbf{V}$, m as mass, $\mathbf{V}$ as velocity) the acceleration by a magnetic field $\mathbf{B}$ is given by the Lorentz force $\mathbf{F_L}$ [5]

$$\mathbf{F_L} = e\,(\mathbf{E} + \mathbf{V} \times \mathbf{B}). \tag{1.1}$$

Where relativistic factors β and γ are $\beta = \frac{v}{c}$ and $\gamma = \frac{1}{\sqrt{1-\beta^2}}$. Here, v is the velocity of the particle and c is the speed of light. The normalized amplitude of the electric field, a , is given by $a = eE/mc\omega_0$

Where, E is the peak laser amplitude of electric field ω_0 is the laser frequency. The normalized amplitude of magnetic field, b , is given by

$$b = eB_0/mc\omega_0 = \omega_{c0}/\omega_0 = \bar{\omega}_{c0}$$

Where, ω_{c0} is the cyclotron frequency. $\bar{\omega}_{c0}$ is the normalized cyclotron frequency and B_0 is the peak laser amplitude of magnetic field.

1.4 Types of transitions in radiation transfer.

When super intense laser is incident on a solid target, very hot plasma with temperature $\sim$ KeV is produced. Plasmas are the fourth state of matter which are made up of highly energetic electrons, ions, atoms etc. When highly energetic charged particles interact with each other, radiations are produced. The radiations are produced from different processes dynamically. As the particles involved must loose energy and release photons to uphold energy conservation. In essence sources of radiation are categorized into three generic processes: bound-bound, free-bound and free-free transitions [6, 7, 8, 27]. For a given temperature and density, each species will contribute many different energy levels according to their own ionization levels. The higher the temperature, the greater the average ionization will be for each species. This provides a rich energy structure for electrons to perform energy transitions. As the electron kinetic energy can be very high in plasmas, free electrons may collide at great velocities with bound electrons. These collisions cause changes in the energy of the electrons that are bound to the ions involved. Then, they become excited and pushed to a higher energy level. Usually, these excited states are unstable. After a period of time, electrons will relax back to a lower energy level and emit a photon. This is known as bound-bound type of transition since both

the initial and final state of electrons bound on an unoccupied orbital state. The number of possible transitions that can occur in this case can be quite large due to the large number of energy levels available. The second source of radiation is from free bound transitions. Plasmas can be divided into positively charged ions and negatively charged electrons. As the temperature of plasma increases, electrons begin to be freed from their bound states. The higher the temperature, the greater the free electron population. In plasmas, electrons and ions are continuously interacting with each other. So, it is possible for electrons to be recaptured by ions. This process is called recombination. In this type of transitions, two cases are possible. A free electron may directly decay to a bound state in a one step process. The other process is through a two steps dielectronic recombination. The third category of transition is free-free transition. This emission of energy comes from the acceleration or deceleration of charged particles when subjected to an external force. In this instance, the external force that is being applied is emanating from all the surrounding ions and electrons which are generating strong electric and magnetic fields. Bremsstrahlung and radiation reaction (radiative damping) include in this type of transition. In this process, electron loses energy by emitting radiation.

1.5 Bremsstrahlung

Bremsstrahlung is the electromagnetic radiation produced by the acceleration or deceleration of a charged particle, such as an electron when deflected (scattered) by another charged particle such as an atomic nucleus. The moving electron loses kinetic energy and emit photons due to the acceleration of electron. In the low density steady-state plasmas, free-free or Bremsstrahlung radiation becomes a dominant mechanism of emission at high temperatures. Current driven plasmas are already a significant source of Bremsstrahlung as the energy deposition is high in such devices. The other side of high energy density physics showcasing extreme temperatures is in the area of ultra-fast ultra-short laser-matter interactions. With current lasers capable of delivering of the order of $10^{22}\,\mathrm{W/cm^2}$ of intense laser light and with more powerful laser on the horizon, extreme temperatures are encountered in such interactions and it has been predicted that Bremsstrahlung radiation will be the dominant cooling mechanism at these intensities. In chapter 3, we discuss more about Bremsstrahlung radiation generated by intense laser produced energetic electrons.

1.6 Radiative damping

Every charged particle emits radiation when it is accelerated. Especially, electrons emit radiation most strongly during acceleration due to the small charge/mass ratio, and then the electron loses some of its energy. This is known as radiative damping. Laser intensity is predicted exceed to 10^{22} W/cm^2 in a few years. In this irradiance, electrons can theoretically reach the strong relativistic energy regime, where then radiation damping is also very important in laser plasma interaction. A plasma can be divided into two types; underdense plasma and overdense plasma. Radiation damping is less efficient in overdense plasmas because the laser field usually is not strong enough for radiation to dominate the particle motion . While in the underdense plasma, the radiation damping is important because the laser field is strong enough for radiation to dominate the particle motion. A free electron accelerated by a plane wave does not radiate. So, the radiation damping effect is very small in a simple plane wave [12]. But the radiation damping effect is not small for Gaussian pulse or other types of pulses. In chapter 4, we discuss the effect of radiation damping in laser plasma interaction.

1.7 Laser Plasma Interaction

Plasma is the fourth state of matter. Plasma is an ionized gas. Heating a gas may ionize its molecules or atoms, thus turning it into a plasma, which contains electrons or ions. Ionization can be induced by other means, such as strong electromagnetic field applied with a laser. Plasmas are the most common state of matter in the universe. They are even common here on earth. Essentially, the sun, like most stars, is a great big ball of plasma.

When laser light is incident into the plasma, laser energy is absorbed near the critical surface. It means that a large fraction of laser energy is absorbed in the preformed plasma in front of the overdense plasma. Specially electrons in the plasma absorb most of that energy. Electrons which interact with a laser field and gain energy directly are called hot electrons. The field strength is so strong that the motion of the electrons becomes relativistic when the laser intensity is greater than 10^{18} W/cm^2. This phenomenon particularly makes the $J \times B$ absorption mechanism to be dominant in the case of normal incidence of laser light on a steep density plasma [13]. The electron motion is very important because it creates the various nonlinear processes occuring inside the plasma such as high electric and magnetic field generation

[14], ion acceleration [15],[16],[17].

At 1-2ns ahead of the main pulse of the laser light with an intensity above 10^{12} W/cm^2 , there is a prepulse by set up or naturally. The prepulse is intense enough to ablate the irradiating surface. Therefore, the low density plasma is created at the interaction surface. The density scale length of this finite length plasma in front of solid is given by [1]

$$L_s = n\frac{dx}{dn} \tag{1.2}$$

The main pulse interacts with the preformed plasma . This laser light propagates in the preplasma and stops at the density where the plasma frequency is equal to the laser frequency. Then the laser is damped over a distance called the skin depth [3] $l_s = c/\omega_p$ where ω_p is plasma frequency and is given by,

$$\omega_p = \sqrt{\frac{4\pi e^2 n_e}{m_e}} \tag{1.3}$$

The dispersion relation is given by [18]

$$kc = \sqrt{\frac{\omega_p^2}{\gamma} - \omega_0^2} \qquad where \quad \gamma = \sqrt{1 + p_{osc}^2/m_e^2c^2} \tag{1.4}$$

where ω_0 and ω_{pe} are laser and plasma frequency. The case is non

relativistic when the intensity of laser is less than or equal to 10^{18} W/cm^2, and in this case $\gamma = 1$. Above this intensity, the case is relativistic and γ is greater than 1. When $\omega_{pe} = \omega_0$ laser light reflect for non relativistic case and this density is known as critical density which is given by [18]

$$n_{cr} = \gamma \frac{1.1 \times 10^{21}}{\lambda_\mu^2} \ cm^{-3} \tag{1.5}$$

Here λ_μ is the wavelength in micron unit.

For a relativistic case $\gamma > 1$ laser light can propagate even further into the overdense plasma due to the fact that electron mass increases in the plasma frequency equation (1.4) as their motion become relativistic.

1.7.1 Relativistic J $\times$ B Heating

For the relativistic case, $J \times B$ heating mechanism is very important for electron motion. It is caused by the electrostatic field driven by the oscillating component of the ponderomotive force of the laser light [19]. For an intense relativistic flux ($I > 10^{18}$ W/cm^2) of laser light, the magnetic component of Lorentz force is very strong and can excite longitudinal oscillations. Ponderomotive force is exerted by the laser light to the plasma. In such a case, many plasma electrons are heated

by the oscillating component of the ponderomotive force [19]. The equation of motion of the electrons near the vacuum plasma interface with velocity $\mathbf{v}$ and momentum $\mathbf{p}$ is given by [19]

$$\frac{\delta \mathbf{p}}{\delta t} + \mathbf{v} \cdot \nabla \mathbf{p} = -e \left[\mathbf{E} + \frac{\mathbf{v} \times \mathbf{B}}{c} \right] \tag{1.6}$$

Where $\mathbf{E}$ is the electric field and $\mathbf{B}$ is the magnetic field.

Longitudinal component of this momentum is described as [19]

$$\frac{\delta \mathbf{p_l}}{\delta t} = e\nabla\phi - m_0 c^2 \nabla(\gamma - 1) \tag{1.7}$$

The first term of the above equation is the electrostatic force driven by the charge separation on the surface, and the second term is the ponderomotive force, which is defined as [19]

$$f_p = -m_0 c^2 \nabla(\gamma - 1) \tag{1.8}$$

Ponderomotive force is the negative gradient of the ponderomotive potential. The force tends to push electrons away from regions of locally higher intensity. Therefore, electrons will drift away from the center of focused laser beam.

The oscillatory energy of the electron is then given by [19]

$$\varepsilon_h = -m_0 c^2 (\gamma - 1) \tag{1.9}$$

where γ is the relativistic gamma factor in the laser field,

$$\gamma = \sqrt{1 + \frac{a_0^2}{2}}, \tag{1.10}$$

and a_0 is normalized laser amplitude.

1.7.2 Inverse Bremsstrahlung

The inverse Bremsstrahlung process is the main absorption mechanism of laser energy in underdense plasma for the laser intensity below 10^{15} W/cm^2. In this process an electron absorbs energy from the laser beam during a collision with an ion or atomic nucleus. According to the Dirac theory of the electron, both positive - energy and negative - energy electrons may exist. We estimate the opacity of inverse Bremsstrahlung for which it becomes significant. The opacity of inverse Bremsstrahlung is [10, 11]

$$k_\nu = 2.42 \times 10^{-37} Z^2 n_i n_e \frac{1}{(k_B T_e)^{1/2}} \frac{1}{(h\nu)^3}, \tag{1.11}$$

where opacity, k_ν, is in 1/cm , number densities of electron(ion), $n_{e(i)}$, are in 1/cm^3, photon energy, $h\nu$, is in eV, and the electron temperature, $k_B T_e$, is also in eV. From Eq. 1.11 we know that in intense laser matter interaction with $k_B T_e \sim 1000$ eV, $n_e \sim 10^{21}$ $1/cm^3$, $n_i \sim 10^{23}$ 1/cm^3

and $h\nu \sim 10^6\ eV$, opacity of inverse Bremsstrahlung is 3217.96×10^{-11} $1/cm$ which is negligible.

In the next section, we discuss about particle in cell simulation and radiation transport model. Bremsstrahlung and pair production are analyzed in chapter 3. In chapter 4, we discuss about radiative damping. Chapter 5 contains the discussion and summary.

Chapter 2 Numerical Modeling

2.1 Particle-in-Cell simulation

Particle in cell code is very powerful tool to model the interaction of charged particles with surrounding electrostatic and magnetic fields. It depends upon Maxwell's equations and the Lorentz force. Charged particles in the plasma are represented in PIC simulations as macro-particles. Number of particles in a real plasma is on the order of Avogadros number (6.02×10^{23}). Due to a limitation of computer memory, the number of particles we can deal is an order of 10^{10} as the maximum. In a plasma, particles interact both with each other and with an external electric and magnetic fields. So, it is very expensive to solve Maxwell equation directly between each pair of particles computationally. To solve Maxwell's equations numerically, spatial resolution of the solution to Maxwell's equations must be finite [20]. The simulation region is divided into a grid of cells. These elements are interchangeably referred to as 'cell', 'mesh' and 'grid'. At each cell vertex, the densities and currents from macro-particle masses and motions are evaluated alongside Maxwell's equations. Thus macro-particles in a Particle-in-

Cell simulation interact indirectly via the fields calculated on grids, rather than through direct electrodynamic particle-particle interactions [20]. Kinetic processes in plasmas are well suited to Particle-in-Cell simulations.

In a plasma, Debye length is the measure of a charge carrier's net electrostatic effect in solution, and how far those electrostatic effects persist. Debye sphere is a volume whose radius is the Debye length and outside of which charges are electrically screened. Debye length is

$$\lambda_D = \frac{v_{\text{thermal}}}{\omega_p} \tag{2.1}$$

Therefore macro-particle interactions only need to be evaluated within a local region, the collision-less plasma skin depth, $\frac{c}{\omega_p}$. This allows macro-particles to contribute to currents and densities at grid vertices only in the nearby regions.

A collision model using equally weighted particles was first described by Shanny et al. [21]. This was extended to exactly conserve non-relativistic momentum and energy in multi-component plasmas by Takizuka and Abe [22]. A relativistic correction was subsequently introduced by Sentoku [23]. Monte-Carlo techniques were introduced by Miller and Combi [24]and extended to unequal particle weights by Nanbu and Yonemura [25].

The collision frequency depends on the relative velocity of the pairing particles and collisions of the same species and interspecies could be considered. The extended model is different in the way that exchange of energy and momentum in the fully relativistic mechanics. The relativistic extension is essential to study the laser isochoric heating, where the laser produced relativistic electrons are colliding the target plasmas.

In PIC codes, the meshes of thousands to millions of interacting plasma electrons and ions are followed in time as the particles move in electromagnetic fields calculated self-consistently from the charge and current densities created by these same plasma particles. In the simplest kinetic description of a plasma one usually start with single-particle velocity distribution function $f(\mathbf{r}, \mathbf{v})$, which evolves according to Vlasov Equation (Elliot, 1993) [26]

$$\frac{\delta f}{\delta t} + \mathbf{v} \cdot \frac{\delta f}{\delta \mathbf{x}} + q(\mathbf{E} + \frac{\mathbf{v}}{c} \times \mathbf{B}) \cdot \frac{\delta f}{\delta \mathbf{p}} = 0 \tag{2.2}$$

The distribution function $f(\mathbf{r}, \mathbf{v})$ is 6-dimensional, so the general solution is intractable for most practical purposes. PIC code is simpler and based on the following facts

- Distribution function is represented by finite-sized particle each

carrying charge q_i and mass m_i.

- These finite sized particle called super particle or macro particle is treated as real particle
- The size of cell is $\sim$ Debye length.
- The coulomb field from other particle (outside the cell) is shielded but the collective effects remain.

Precisely saying that first step in PIC simulation is defining grids and distributing the particles all over the grids, Fig-2.1, and the number of particles in each cell are decided by the density of material which is being irradiated.

The particles are moved individually in Lagrangian fashion according to Lorentz equation:

$$\begin{aligned} \frac{d}{dt}(\gamma \mathbf{v}) &= \frac{q}{m}(\mathbf{E} + \frac{\mathbf{v}}{c} \times \mathbf{B}) \\ \gamma &= \left(1 - \frac{v^2}{c^2}\right)^{-1/2} \end{aligned} \tag{2.3}$$

Here laser light which is a linearly polarized electromagnetic wave, shown in Fig-2.2, having electromagnetic and electrostatic component propagting along x; no variation in y or z. The Maxwell quations for the transverse fields

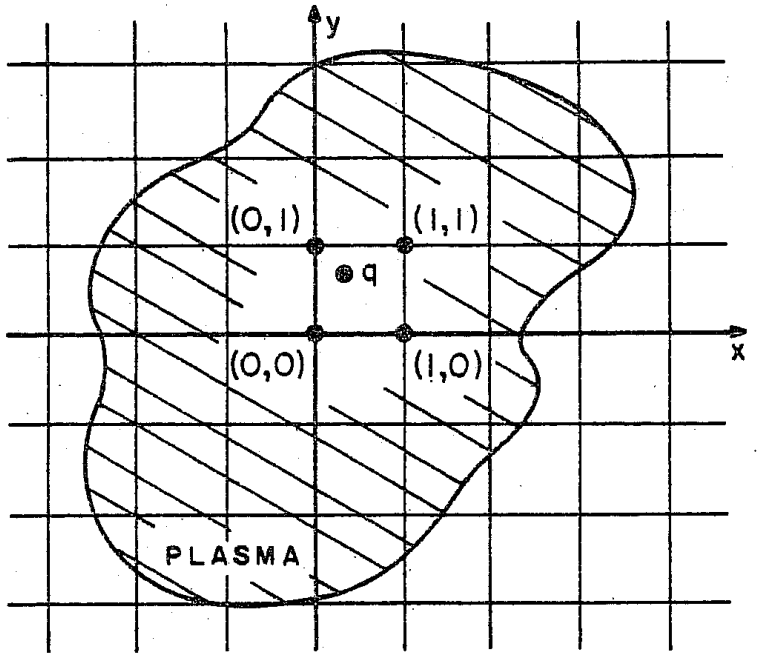

Figure 2.1: Mathematical grid set into the plasma region, charged particle q at(x,y) is counted in terms of ρ at the nearby grids and in terms of J at the faces between these points

$$\frac{\partial \mathbf{E}}{\partial t} = c\nabla \times \mathbf{B} - \mathbf{J} \tag{2.4}$$

$$\frac{\partial \mathbf{B}}{\partial t} = -c\nabla \times \mathbf{E} \tag{2.5}$$

By adding and substracting these equations, for E_y, B_z, and J_y, we obtain the following convection eqaution,

$$\left[\frac{\partial}{\partial t} \pm c\frac{\partial}{\partial x}\right] F^{\pm} = -\frac{1}{2}J_y \tag{2.6}$$

for the left and right going field quantities,

$$F^{\pm} \equiv \frac{1}{2}\left(E_y \pm B_z\right) \tag{2.7}$$

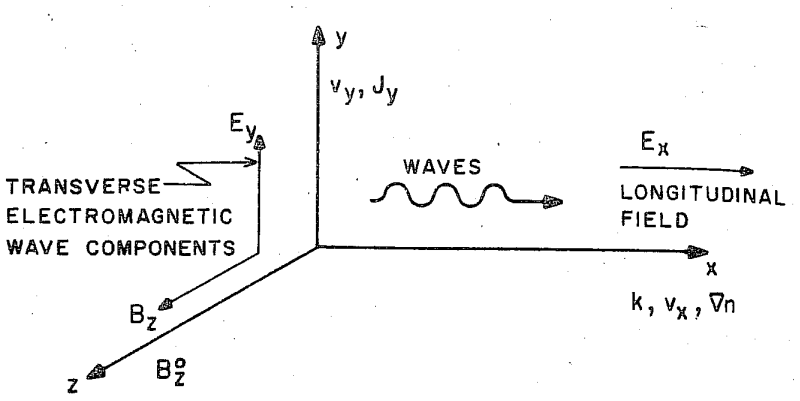

Figure 2.2: Location of the particle and field quantities for linearly polarized 1-D electromagnetic code

the transverse can be recovered from $F^{\pm}$ by

$$E_y = F^+ + F^- \tag{2.8}$$

$$B_y = F^+ - F^- \tag{2.9}$$

Eq-(2.6) can be solved very easily when $c \cdot \Delta t = \Delta x$ by discretizing the following way (Δt is small time step and Δx is small distance)

$$\frac{F^{\pm}\left(t + \Delta t, x \pm c\Delta t\right) - F^{\pm}\left(t, x\right)}{\Delta t} = -\frac{1}{2} J_y^{\pm}\left[t + \frac{\Delta t}{2}, x \pm c\frac{\Delta t}{2}\right] \tag{2.10}$$

Where $J_y^{\pm}$ is an appropriately-averaged current, space- and time-centered and can be obtained by mapping the local particle positions and velocities onto a grid. Following are the velocity and position differential equations;

$$v_i^{n+\frac{1}{2}} = v_i^{n-\frac{1}{2}} + \frac{q_i}{m_i}\left[(E_y)^n + \frac{v_i^{n-1/2}}{c} \times (B_z)^n\right]\Delta t \tag{2.11}$$

$$x_i^{n+1} = x_i^n + v_i^{n+\frac{1}{2}}\Delta t \tag{2.12}$$

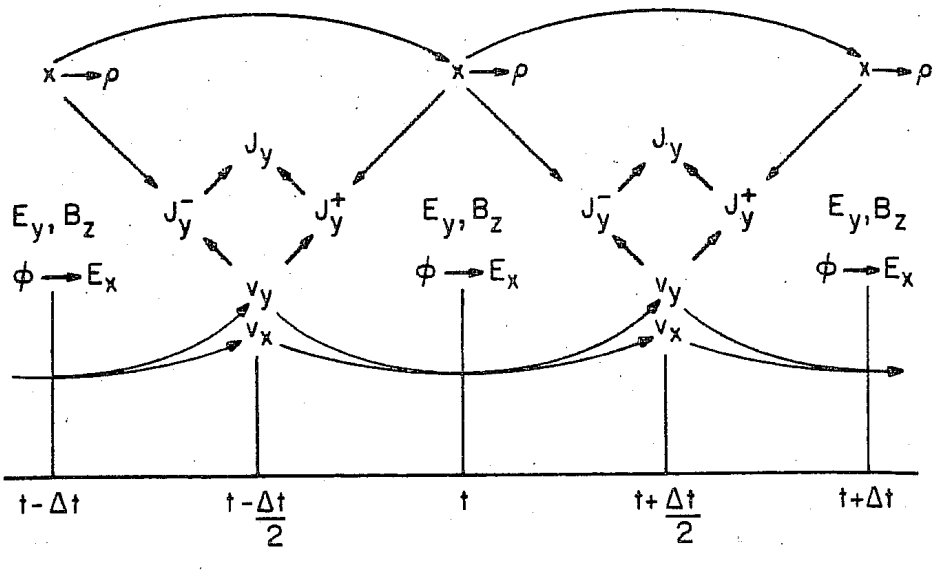

Figure 2.3: Time stepping for 1-D electromagnetic program. Particles are advanced by leap-frog method shown by curved lines.

The current densities J_y^- and J_y^+ are computed from velocities $v_y^{n+1/2}$ assigned to the grid by linear weighting to positions x^n and x^{n+1} respectively. This says that fields at $j \mp 1$ propogate to j affected by the source term as shown in Fig-2.3;

$$(j_y^{\pm})^{n+1/2} = \sum_i q_i v_i^{n+1/2} \frac{1}{2} \left[S(X_{j\pm1/2} - x_i^{n+1}) + S(X_{j\pm1/2} - x_i^n) \right] \quad (2.13)$$

The field at grid j, time $n+1$, is;

$$(F_j^{\pm})^{n+1} = (F_{j\mp1}^{\pm})^n - \frac{\Delta t}{4}((J_y^-)_{j\mp1}^{n+1/2} + (J_y^+)_j^{n+1/2}) \quad (2.14)$$

Each simulation cycle increments a time step counter, moving

the simulation clock forward by one time step (Δt).

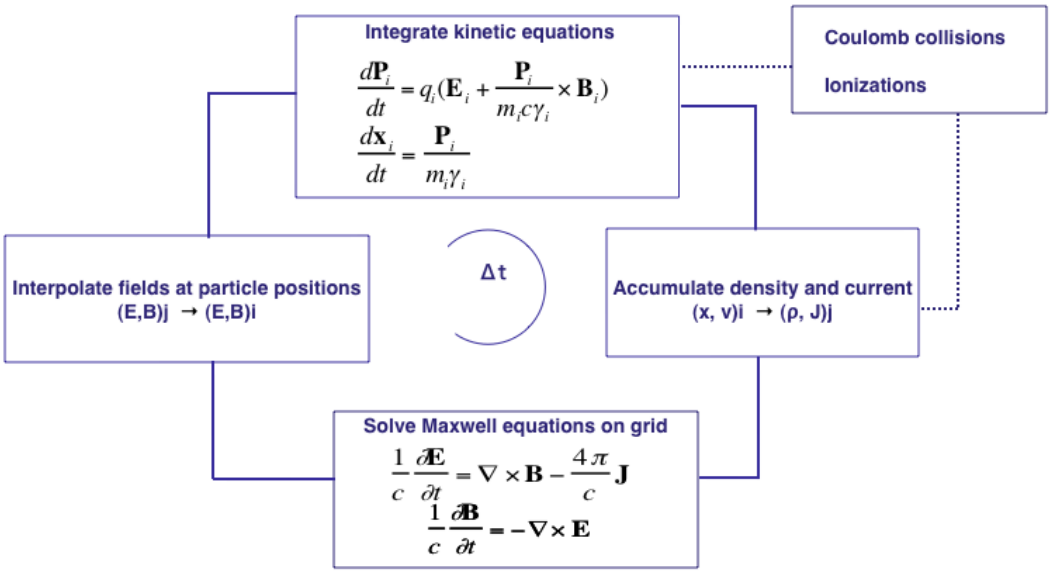

Figure 2.4: General PIC solver overview

The scheme depicted in Fig. 2.4 is an iterative process which follows the procedure,

1. Integrate macro-particle kinetic equations from relativistically corrected Newtonian mechanics

2. Accumulate(Collect) densities and currents at grid points using interpolation from macro-particle positions

3. Randomize and collide macro-particles with neighbors in the same cell

4. Evaluate ionization conditions and distribute any ionization product macro-particles

5. Solve Maxwell equations on grid using directionally split representation by shifting fields and accumulating currents
6. Interpolate fields at macro-particle positions using field solutions from grid
7. Increment simulation time and repeat

2.2 Discussion and conclusion of Particle-in-Cell simulation

The Particle-in-Cell simulation model of plasma simulation is well established, with continuous innovation pushing the model into new areas. As a kinetic solver, it directly evaluates the field-particle interactions, providing insight into electromagnetic instabilities and the effect of their growth on the larger scale physics of laser produced plasma experiments.

The PICLS implementation provides an advanced solver for many simulation aspects

- Directional splitting of Maxwell's equations provides a simple copy-and-accumulate scheme which cleanly decouples dimensions in up to 3D simulations.
- Particle motions are relativistically accurate.

- Monte Carlo collisions are relativistically accurate and provide exact energy conservation.
- High density plasmas are collisionally simulated without prohibitive computation requirements.

PICLS [50] resolves the relevant physics of particles and electromagnetic fields required to accurately model laser plasma interactions, energy transport, and collisional heating.

2.3 Radiation Transport Code

Laser interacting with high-Z target materials generate hot, dense, radiating plasmas for which radiation effects could be very important, becoming one of the dominating energy-exchange mechanisms. In order to evaluate the effect of radiation on the laser-produced plasma development, a radiation transport model is developed. The following radiation transport equation is integrated over the photon energy and for each angle [27],

$$\left(\frac{1}{c}\frac{\partial}{\partial t} + \ \mathbf{n}\cdot\nabla\right) I(r,\Omega,\nu,t) = \eta(r,\Omega,\nu,t) - \chi(r,\Omega,\nu,t) I(r,\Omega,\nu,t) \tag{2.15}$$

where $I(r,\Omega,\nu,t)$ is the intensity $[erg/cm^2/Hz/srad]$, Ω is the solid angle, $\eta(r,\Omega,\nu,t)$ is the emissivity $[erg/cm^3/s/Hz/srad]$ and $\chi(r,\Omega,\nu,t)$

is the opacity $[1/cm]$.

In general, emissivity and opacity have three contributions: bound-bound or line transitions, bound-free associated with ionization/recombination, free-free associated with transitions between continuum states.

Radiation energy is divided into groups of finite energy width i.e. the X-ray photons are grouped in non-uniform energy bins in the 1-10,000 eV range, which are adaptively selected to capture the emission lines in the spectrum. The transport equation is integrated over the energy width for each group, then solved to obtain the radiation intensity for each group, I_g . Discrete ordinate method is applied for the angular variables (polar angle θ and ϕ) [30]. The transport equation is solved for each discrete direction (m,n) to obtain the radiation intensity in that direction, $I_{m,n}$. The constrained interpolation (CIP) scheme having 3rd order spatial accuracy is applied for advection term [31, 32, 33]. Because of explicit method, this scheme is suitable for MPI (massive parallel computing). Emissivity/opacity database is prepared for specified temperature, density and photon energy by using FLYCHEK code before starting the simulation[34]. The PICLS code simulates the plasma evolution and provides the average electron density n_e and bulk plasma temperature T_e to the RT(Radiation Transport) code which then calculates the emissivity and opacity by interpolating

the database values.

2.4 Emissivities of γ-rays

We would like to determine the the emissivity of Bremsstrahlung and radiative damping in intense laser-matter interaction. From chapter 1, we know that in intense laser matter interaction opacity is negligible. So, we use the optically thin approximation. Then, radiation transport equation can be written as

$$\left(\frac{1}{c}\frac{\partial}{\partial t} + \ \mathbf{n}\cdot\nabla\right) I = \eta \tag{2.16}$$

Emissivity of the Bremsstrahlung radiation is

$$\eta(\omega) = \frac{\partial \chi_R}{\partial \hbar\omega}\cdot n_e \cdot n_i \cdot c \cdot \hbar\omega \tag{2.17}$$

where, $n_{e(i)}$ is number density of electron(ion). $\frac{\partial \chi_R}{\partial \hbar\omega}$, cross-section of relativistic Bremsstrahlung, is (for details see chapter 3)

$$\frac{d\chi_R}{d\omega} = \frac{16}{3}\frac{Z^2e^2}{c}\left(\frac{e^2}{mc^2}\right)^2\left(\ 1 - \frac{\hbar\omega}{E} + \frac{3\hbar^2\omega^2}{4E^2}\ \right)\left[\ \ln\left(\frac{2EE'}{mc^2\hbar\omega}\right) - \frac{1}{2}\right]. \tag{2.18}$$

Emissivity of the radiative damping is

$$\eta(\omega) = dI \cdot n_e \tag{2.19}$$

where, dI , the differential intensity of emitted radiation, is (for details see chapter 4)

$$dI \;=\; \frac{1}{\hbar\omega_c}\,(\,\mathbf{P_{1st}} + \,\mathbf{P_{2nd}})\,F\left(\frac{\hbar\omega}{\hbar\omega_c}\right)\,d\hbar\omega. \tag{2.20}$$

Where P_{1st} and P_{2nd} are the power radiated by 1st and 2nd order damping respectively.

The frequency ω is normalized by the maximum frequency ω_c that electron can emit [65].

$$\omega_c = \frac{3}{2}\frac{eB}{mc}\gamma^3 \tag{2.21}$$

B is the magnetic field and

$$F(r,\chi) = 3^{5/2}(8\pi)^{-1} r\left[\int_{r_\chi}^{\infty} K_{5/3}(r')dr' + r r_\chi \chi^2 K_{2/3}(r_\chi)\right]. \tag{2.22}$$

$r_\chi = \frac{r}{(1-\chi r)}$, $K_{5/3}$ and $K_{2/3}$ are modified second order Bessel function.

The γ-ray emissivities are implemented in the radiation transport calculation. Using PICLS with the radiation transport module we

can study the γ-ray emission process during the intense laser matter interaction.

2.5 Discussion and conclusion of radiation transport code

Laser interactions with high-Z target materials generate hot, dense, radiating plasmas for which radiation effects could be very important, becoming one of the dominating energy-exchange mechanisms. In order to evaluate the effect of radiation on the laser-produced plasma development, a radiation transport model coupled with a particle-in-cell code, PICLS were developed. We have implemented an attenuation operator solver short-characteristics numerical scheme in order to solve the steady-state radiation transport equation. In solving the equation of radiation transport we used a database of emissivities and opacities as functions of photon frequency, computed by the 0-D code FLYCHK for chosen densities and temperatures. we use Constrained interpolation profile (CIP) scheme for advection, Multi-group method for photon energies and S_N method for direction. The γ-ray emissivities are implemented in the radiation transport calculation. Using PICLS with the radiation transport module we can study the γ-ray emission process during the intense laser matter interaction. This is done to transport energy inside the target as well as outside the target.

Chapter 3 Bremsstrahlung and Pair Production

3.1 Introduction

The generation of γ-ray/hard x-ray radiation from intense laser produced plasmas has been reported [35, 36, 37]. The observed photon energies are over 100 MeV. These γ-ray are emitted due to the bremsstrahlung of electrons accelerated by an intense laser on the surface. For normal incidence, electrons are accelerated along the target normal direction by the ponderomotive force [38]. The maximum energy of these electrons are observed to be higher than 500 MeV in the experiment [38]. The hot electron velocity distributions are usually non-isotropic and non-Maxwellian [67]. To evaluate the γ-ray emission from laser produced plasmas, we determined electron distributions in laser plasmas by electromagnetic particle-in-cell (PIC) simulations. For this purpose, the radiation cross-section for the relativistic Bremsstrahlung and that of Bethe-Heitler pair production are implemented in the radiation transport code coupled with PICLS. The particle simulations have been used to analyze the generation of fast electron by intense

lasers [38, 39, 40]. The high initial temperature is not appropriate for describing finite resistivity effects on return currents, which is important in the laser-solid interaction [41]. We set the initial plasma temperature to be several hundred eV. The average collision frequency of electron-ion scattering at this temperature is comparable to the plasma frequency in the solid density plasmas. In this chapter, we investigate the γ-ray emission, and simulate the laser plasma interaction from laser intensity $10^{18}\,\mathrm{W/cm^2}$ to $10^{23}\,\mathrm{W/cm^2}$ using a radiation transport code coupled with PICLS, which includes the collisional effects on electron transport and absorption where the relativistic binary collision and ionization model is used. This PICLS code is able to simulate the heat transport and the laser absorption for intense laser plasma correctly and effectively. We introduce the relativistic bremsstrahlung model as follows.

3.2 Theory

3.2.1 Bremsstrahlung

The elastic scattering cross section of a charged particle by a static Coulomb field is given by the Rutherford formula [42]:

$$\frac{d\sigma_s}{d\Omega'} = \left(\frac{2Ze^2}{pv}\right)^2 \frac{1}{(2\sin\theta'/2)^4}, \tag{3.1}$$

where $d\Omega'$ is the solid angle, θ' is the scattering angle of the particle, $p = \gamma\beta mc$ is the momentum and $v = \beta c$ is the velocity of electron. In a Coulomb collision with momentum transfer Q the incident particle is accelerated and emits radiation. The differential radiation cross section is defined as [42],

$$\frac{d^2\chi}{d\omega dQ} = \frac{dI(\omega, Q)}{d\omega} \cdot \frac{d\sigma_s}{dQ}(Q), \tag{3.2}$$

where, $dI(\omega, Q)/d\omega$ is the energy radiated per unit frequency interval in a collision with momentum transfer Q. The radiation cross section integrated over momentum transfer is

$$\frac{d\chi_R}{d\omega} = \frac{16}{3}\frac{Z^2e^2}{c}\left(\frac{e^2}{mc^2}\right)^2 \frac{1}{\beta^2}\int_{Q_{min}}^{Q_{max}} \frac{dQ}{Q}, \tag{3.3}$$

or

$$\frac{d\chi_R}{d\omega} = \frac{16}{3}\frac{Z^2e^2}{c}\left(\frac{e^2}{mc^2}\right)^2 \frac{1}{\beta^2}\ln\left(\frac{Q_{max}}{Q_{min}}\right), \tag{3.4}$$

The limits obtained from conservation of energy for relativistic particle must be modified. The changes are of two sorts. The first is

that the maximum effective Q value is no longer determined by kinematics. For larger Q the radiated intensity is logarithmic in Q. So, the Q_{max} is

$$Q_{max} = 2mc \tag{3.5}$$

The second modification is that the photon's momentum can no longer be ignored in determining the minimum momentum transfer. So, the Q_{min} is

$$Q_{min} = \frac{m^2c^3\hbar\omega}{2EE'}. \tag{3.6}$$

Where E and E' are the electron's energy before and after collision.

Substituting the values of Q_{max} and Q_{min} Eq. (3.4), we get

$$\frac{d\chi_R}{d\omega} = \frac{16}{3}\frac{Z^2e^2}{c}\left(\frac{e^2}{mc^2}\right)^2 \ln\left(\frac{\lambda'' EE'}{mc^2\hbar\omega}\right), \tag{3.7}$$

The radiation emitted in the collision of an electron of charge e, energy E and mass m with the Coulomb field of a fixed point charge Ze in terms of the radiation cross-section per unit frequency for the

relativistic Bremsstrahlung is (quantum formula) [42]

$$\frac{d\chi_R}{d\omega} = \frac{16}{3}\frac{Z^2e^2}{c}\left(\frac{e^2}{mc^2}\right)^2\left(1-\frac{\hbar\omega}{E}+\frac{3\hbar^2\omega^2}{4E^2}\right)\left[\ln\left(\frac{2EE'}{mc^2\hbar\omega}\right)-\frac{1}{2}\right], \tag{3.8}$$

where c is the speed of light, $\hbar\omega$ is the energy of photon, E' is the electron energy after the collision, $E' = E - \hbar\omega$, and Z is the atomic number of the target.

The doubly differential radiation cross section for energy radiated per unit frequency interval and per unit solid angle is [42]

$$\frac{d^2\chi_R}{d\omega d\Omega_\gamma} = \left[\frac{3}{2\pi}\,\gamma^2\,\frac{(\,1+\gamma^4\theta^4)}{(1+\gamma^2\theta^2)^4}\right]\frac{d\chi_R}{d\omega}, \tag{3.9}$$

where γ is the relativistic Lorentz factor and θ is the polar angle from the electron moving direction. Eq. (3.9) is plotted in Figure 3.1 with different energies of electrons. In intense laser matter interaction radiations are more collimated in the propagation direction of electron. so, θ can be neglected.

Emissivity of the Bremsstrahlung radiation is

$$\eta(\omega) = \frac{\partial\chi_R}{\partial\hbar\omega}\cdot n_e\cdot n_i\cdot c\cdot\hbar\omega \tag{3.10}$$

where, $n_{e(i)}$ is number density of electron(ion). $\partial\chi_R/\partial\hbar\omega$ is calculated from Eq. (3.9). This emissivity is implemented in radiation transport code.

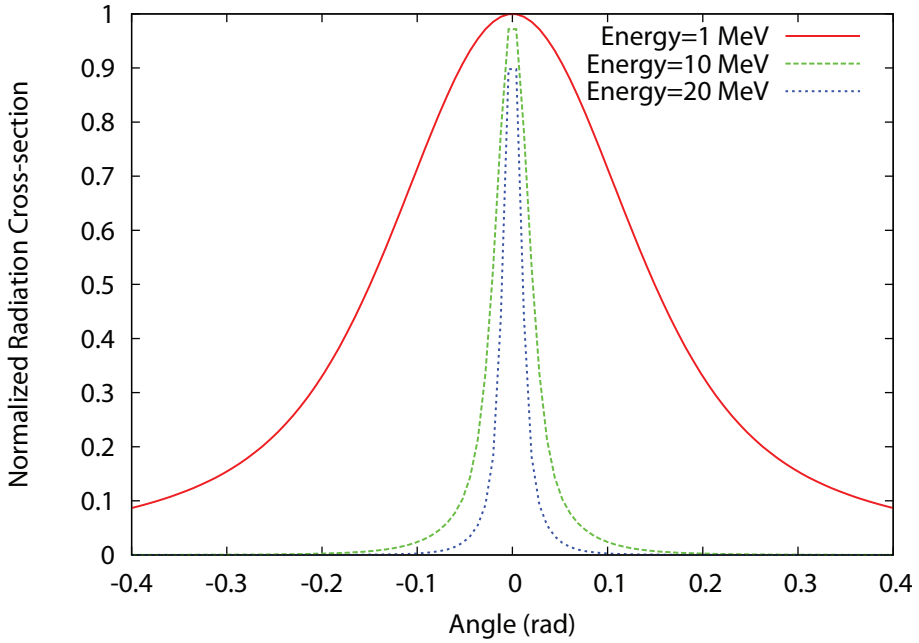

Figure 3.1: Angular distribution of radiation cross-section.

3.2.2 Pair Production

Pair production is the creation of an elementary particle and its antiparticle for example an electron and positron. There are mainly three processes to create pairs from the hot electrons. one is called the trident process, [43]

$$e^- + Z \rightarrow e^+ + 2e^- + Z, \tag{3.11}$$

and the other is called the Bethe-Heitler process, [43]

$$e^- + Z \rightarrow \gamma + e^- + Z, \tag{3.12}$$

$$\gamma + Z \rightarrow e^+ + e^- + Z. \tag{3.13}$$

Another process of pair production is the multiphoton Breit-Wheeler process, [44, 45, 46, 47]

$$e^- + m\gamma_l \rightarrow e^- + \gamma_h, \tag{3.14}$$

$$\gamma_h + n\gamma_l \rightarrow e^+ + e^-, \tag{3.15}$$

where, γ_l is a laser photon and γ_h is the γ-ray photon emission from electron. n and m are the numbers of photons. This multiphoton Breit-Wheeler process could be dominant when laser intensity is above $10^{23}\,\mathrm{W/cm^2}$. Below this intensities and thick target the Bethe-Heitler process is the dominant process because in thick target there are more collisions between electron and target and emitted photon and target.

The Bethe-Heitler pair-production cross section is [48]

$$\begin{aligned} K_n^{BH} &= \bar{\phi}[\frac{692+468\eta+76\eta^2+108\eta^3}{27(1+\eta)^3}K(\eta) - \frac{692+360\eta+692\eta^2}{27(1+\eta)^3}E(\eta) \\ &\quad -4\frac{(1-\eta)^2}{(1+\eta)^2}[\int_0^\eta \frac{K(\xi)}{1-\xi}d\xi - 4\int_0^\eta \frac{d\zeta}{1-\zeta^2}\int_0^\zeta \frac{K(\xi)}{1-\xi}d\xi]] \end{aligned} \tag{3.16}$$

where,

$$\eta = \frac{k-2}{k+2}, \tag{3.17}$$

$$\bar{\phi} = Z^2 \times 5.794662 \times 10^{-28} cm^2. \tag{3.18}$$

$K(\eta)$ or $K(\xi)$ and $E(\eta)$ are complete elliptic integrals of the first and second kinds, respectively. The series expansion of above equation is [49]

$$\begin{aligned} K_n^{BH} &= \bar{\phi}\frac{2\pi}{3}\left(\frac{k-2}{k}\right)^3[1+\frac{1}{2}\rho+\frac{23}{40}\rho^2 \\ &\quad +\frac{11}{60}\rho^3+\frac{29}{960}\rho^4+.....], k \leq 4, \end{aligned} \tag{3.19}$$

and

$$\begin{aligned} K_n^{BH} &= \bar{\phi}[\frac{28}{9}\ln 2k-\frac{218}{27}+\left(\frac{2}{k}\right)^2[6\ln 2k-\frac{7}{2}+\frac{2}{3}\ln^3 2k \\ &\quad -\ln^2 2k-\frac{1}{3}\pi^2\ln 2k+2\zeta(3)+\frac{\pi^2}{6}]-\left(\frac{2}{k}\right)^4 \\ &\quad [\frac{3}{16}\ln 2k+\frac{1}{8}]-\left(\frac{2}{k}\right)^6[\frac{29}{9.256}\ln 2k \\ &\quad -\frac{77}{27.512}]+.....], k \geq 4, \end{aligned} \tag{3.20}$$

where,

$$\rho = \frac{2k-4}{2+k+2\sqrt{2k}}, \tag{3.21}$$

$$\zeta(3) = \sum_{n=1}^{\infty}\frac{1}{n^3} = 1.2020569, \tag{3.22}$$

and k is photon energy in units of the electron rest mass energy.

We know the local γ-rays distribution (photon energy and number of photons) in the radiation transport calculation. so, we can compute the pair productions during the simulation. Number of pairs (np) in the calculation is

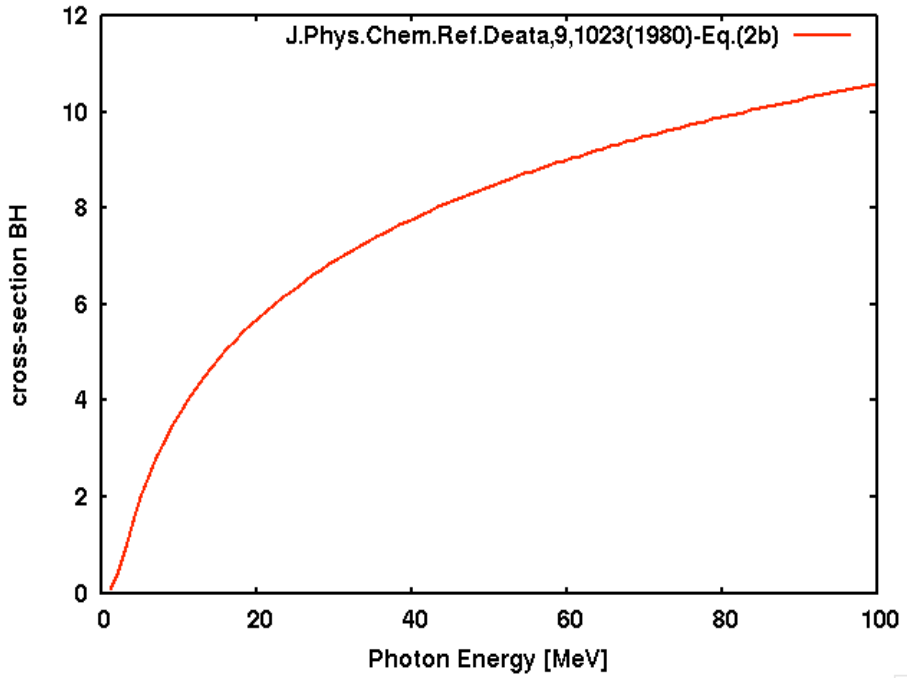

Figure 3.2: (color) Bethe-Heitler cross section of pair production.

$$np = K_n^{BH} \cdot n_i \cdot c \cdot dt \tag{3.23}$$

where, dt is the time step.

3.3 Simulation of super intense laser-matter interaction

We have implemented Eq. (3.8) and Eq. (3.9) in the radiation transport code in order to study the transport of γ-ray photon from Bremsstrahlung in intense laser - matter interaction from $I = 10^{18}\,\mathrm{W/cm^2}$ to $I = 10^{23}\,\mathrm{W/cm^2}$ (if $I < 10^{18}\,\mathrm{W/cm^2}$ the electron is non-relativistic). The numerical code used is the one- & two-dimensional (PIC) code PICLS[50],

which features binary collisions between charged particles and ionization processes in gaseous and solid density plasmas. The target is modeled as a 44μm thick copper slab with uniform density. A few micron thick preplasma is placed in front of the target. Input laser energy is fixed by changing duration, spot size and intensity of laser light. The ion density is set to $50n_c$, here $n_c = 10^{21}\,\mathrm{cm}^{-3}$ is the critical density for a laser wavelength 1μm. The mass (fully ionized charge) of Cu is $64M_p$ (29), where M_p is the proton mass. Then the mass density of the target becomes $\rho = 5.3\,\mathrm{g/cm}^3$, close to the mass density of solid copper. Initially we set the ion charge state $Z = 3$, and electron density is set to neutralize ion charges. The ionization models include field driven ionization in low density plasmas under strong fields and impact ionization which solves for the collisional cross section in dense plasmas [51]. The electron density increases dynamically during laser irradiation via ionization processes. The ionization energies are subtracted from the hot electrons when they ionize atoms via collisions with bound electrons. Initially particles are at rest, with initial plasma temperature set to zero. Our spatial (temporal) resolution is 1/50 of the wavelength (laser oscillation period τ). The simulation also accounts for the energy loss by emission of soft x-ray radiation from free-bound transition, though it is only a minor effect (less than 0.3% of the laser energy) under current

extreme laser intensities.

The target is attached to the transverse boundaries, and an absorbing boundary condition is used for particles — i.e. no hot electrons are reflected back inside the target — to represent the large transverse volume of target. The laser pulse is irradiating from the left boundary onto the target surface. The pulse profile is Gaussian distribution both temporally and radially.

Photon spectrum with different intensities is compared in the Figure 3.3 . As intensity increases, photon energy also increases. High energy tails of photon spectrum at different intensities are clearly seen in the figure. When laser intensity is greater than $10^{21}\,\mathrm{W/cm^2}$ high energy tail of photon spectrum is also greater than 100 MeV. These results are suitable for pair production.

In Figure 3.4, we show a 2D simulation using a laser pulse with an intensity $I = 10^{18}\,\mathrm{W/cm^2}$, a 660 fs pulse duration, and a $8\sqrt{10}\,\mu$m spot where (a) is the instantaneous magnetic fields [MG] at 1637 fs (b) is the electron energy density in logarithmic scale at 1637 fs and (c) is the γ-rays energy density in logarithmic scale at 726 fs. In (a) strong dipole magnetic fields appear inside the target. In (b) we can see the distribution of energy of electrons inside the target and in (c) we can see the energy density range of γ-rays as well angular distribution of

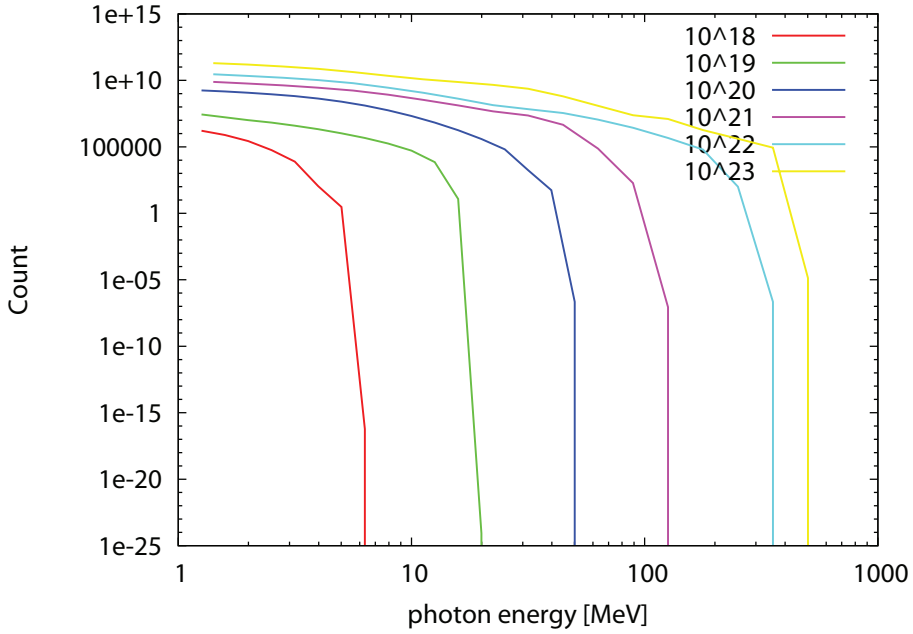

Figure 3.3: (color) 2D-PICLS results; comparison of photon spectrum by Bremsstrahlung from laser intensity $10^{18}\,\mathrm{W/cm^2}$ to $10^{23}\,\mathrm{W/cm^2}$ of ultra-fast heated copper thick target

radiation. Most of the γ-rays are scattered hemispherically in forward direction.

In Figure 3.5, we show a 2D simulation using a laser pulse with an intensity $I = 5 \times 10^{18}\,\mathrm{W/cm^2}$, a 660 fs pulse duration, and a $8\sqrt{2}\,\mu$m spot where (a) is the instantaneous magnetic fields [MG] at 1637 fs (b) is the electron energy density in logarithmic scale at 1637 fs and (c) is the γ-rays energy density in logarithmic scale at 660 fs. In (a) strong dipole magnetic fields appear inside the target. In (b) we can see the distribution of energy of electrons inside the target and in (c) we can see the energy density range of γ-rays as well angular distribution of

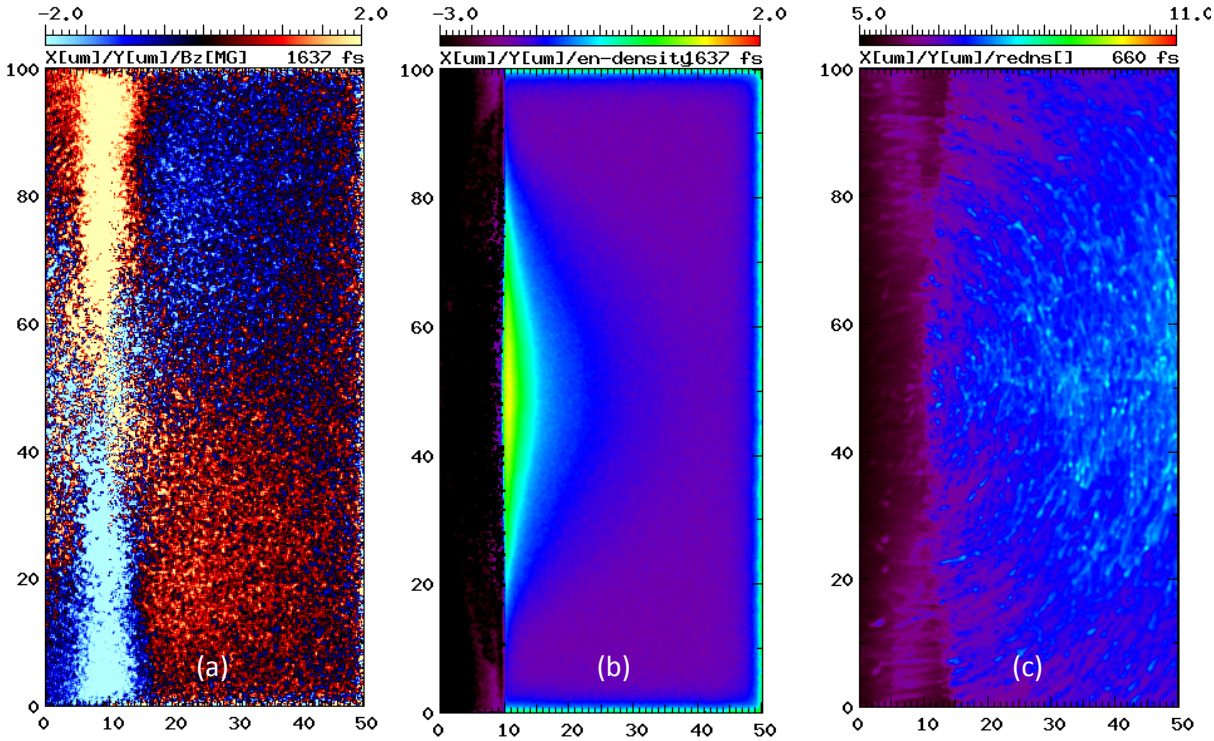

Figure 3.4: (color) 2D-PICLS results at laser intensity $10^{18}\,\mathrm{W/cm^2}$ of (a) instantaneous magnetic fields [MG], (b) electron energy density [MeV·$n_e/100n_c$ logarithmic scale], (c) γ-ray energy density, logarithmic scale]

radiation. Most of the γ-rays are scattered hemispherically in forward direction.

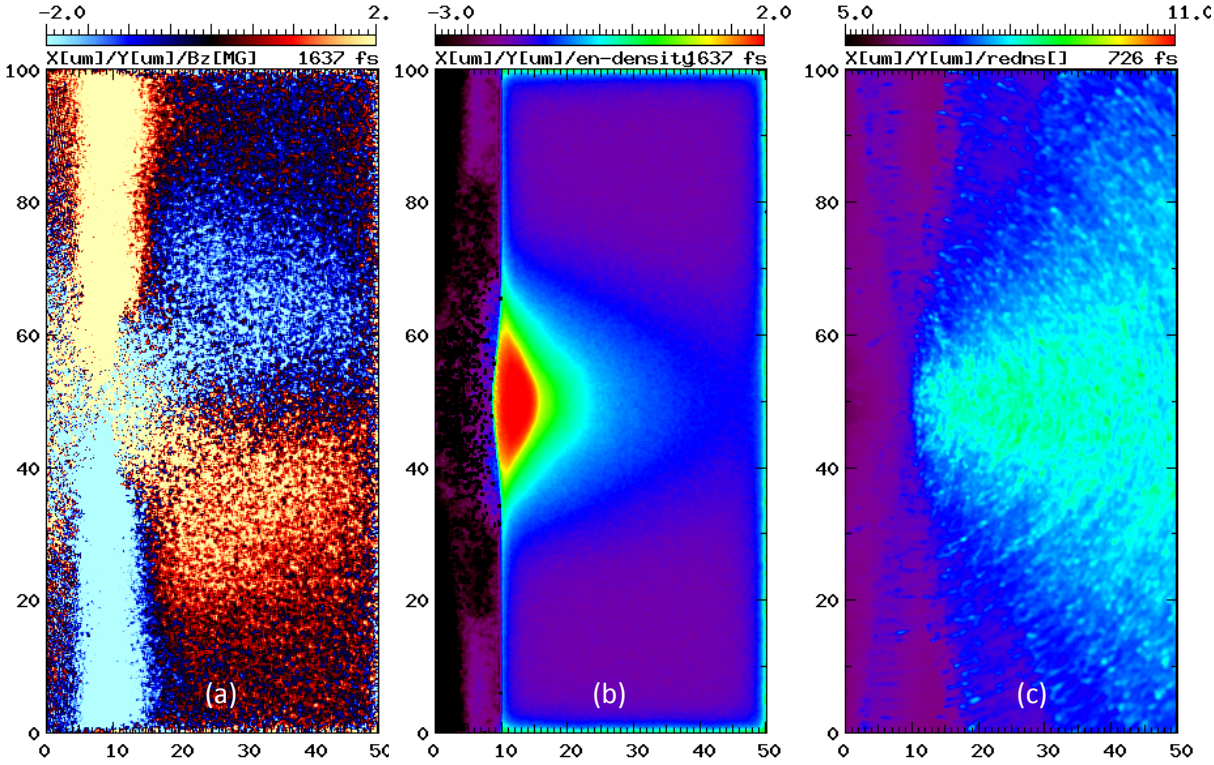

Figure 3.5: (color) 2D-PICLS results at laser intensity $5 \times 10^{18}\,\mathrm{W/cm^2}$ of (a) instantaneous magnetic fields [MG], (b) electron energy density [MeV$\cdot n_e/100n_c$ logarithmic scale], (c) γ-ray energy density, logarithmic scale]

In Figure 3.6, we show a 2D simulation using a laser pulse with an intensity $I = 10^{19}\,\mathrm{W/cm^2}$, a 660 fs pulse duration, and a 8 μm spot where (a) is the instantaneous magnetic fields [MG] at 1637 fs (b) is the electron energy density in logarithmic scale at 1637 fs and (c) is

the γ-ray electron density in logarithmic scale at 396 fs. In (a) strong dipole magnetic fields appear inside the target. In (b) we can see the distribution of energy of electrons inside the target and in (c) we can see the energy density range of γ-ray as well angular distribution of radiation. Most of the γ-rays are scattered hemispherically in forward direction.

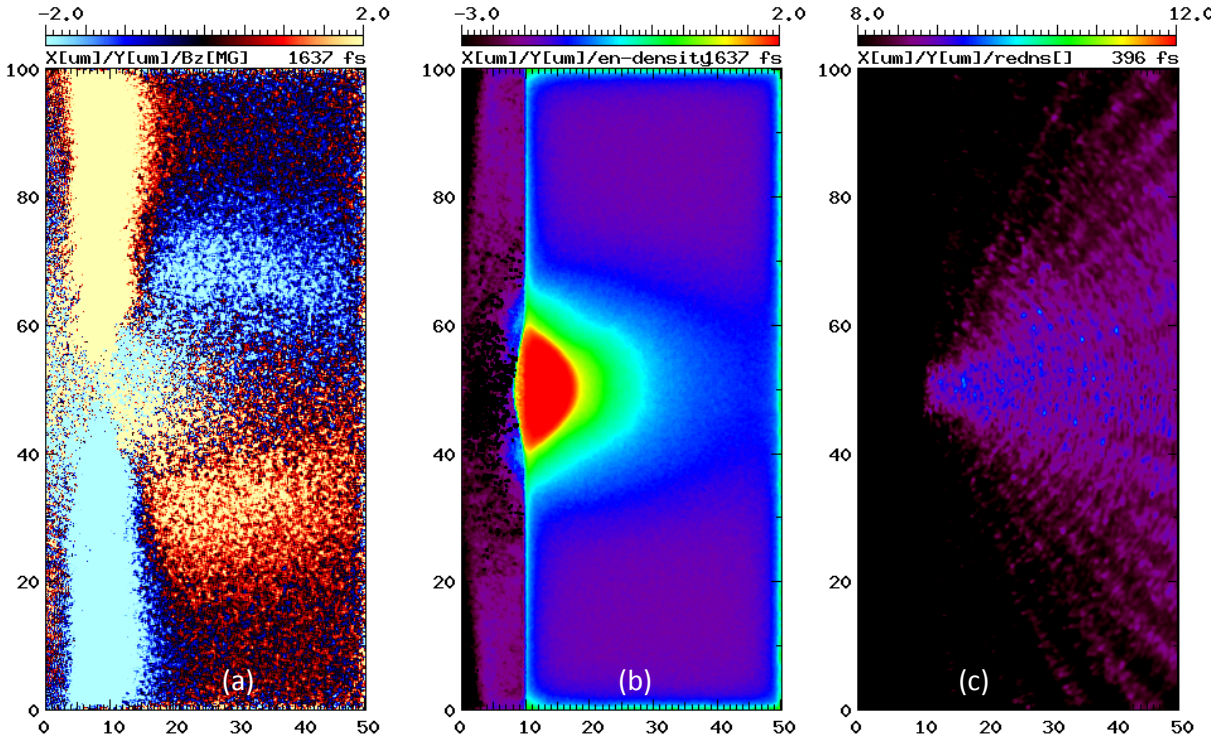

Figure 3.6: (color) 2D-PICLS results at laser intensity $10^{19}\,\mathrm{W/cm^2}$ of (a) instantaneous magnetic fields [MG], (b) electron energy density [MeV$\cdot n_e/100n_c$ logarithmic scale], (c) γ-ray energy density, logarithmic scale]

In Figure 3.7, we show a 2D simulation using a laser pulse with an intensity $I = 5 \times 10^{19}\,\mathrm{W/cm^2}$, a 130 fs pulse duration, and a 8 μm spot where (a) is the instantaneous magnetic fields [MG] at 1637 fs (b) is the electron energy density in logarithmic scale at 1637 fs and (c) is the γ-rays energy density in logarithmic scale at 238 fs. In (a) strong dipole magnetic fields appear inside the target. In (b) we can see the distribution of energy of electrons inside the target and in (c) we can see the energy density range of γ-rays as well angular distribution of radiation. Most of the γ-rays are scattered hemispherically in forward direction.

In Figure 3.8, we show a 2D simulation using a laser pulse with an intensity $I = 10^{20}\,\mathrm{W/cm^2}$, a 66 fs pulse duration, and a 8 μm spot where (a) is the instantaneous magnetic fields [MG] at 393 fs (b) is the electron energy density in logarithmic scale at 393 fs and (c) is the γ-ray electron density in logarithmic scale at 188 fs. In (a) strong dipole magnetic fields appear inside the target. In (b) we can see the distribution of energy of electrons inside the target and in (c) we can see the energy density range of γ-ray as well angular distribution of radiation. Most of the γ-rays are scattered hemispherically in forward direction.

In Figure 3.9, we show a 2D simulation using a laser pulse with

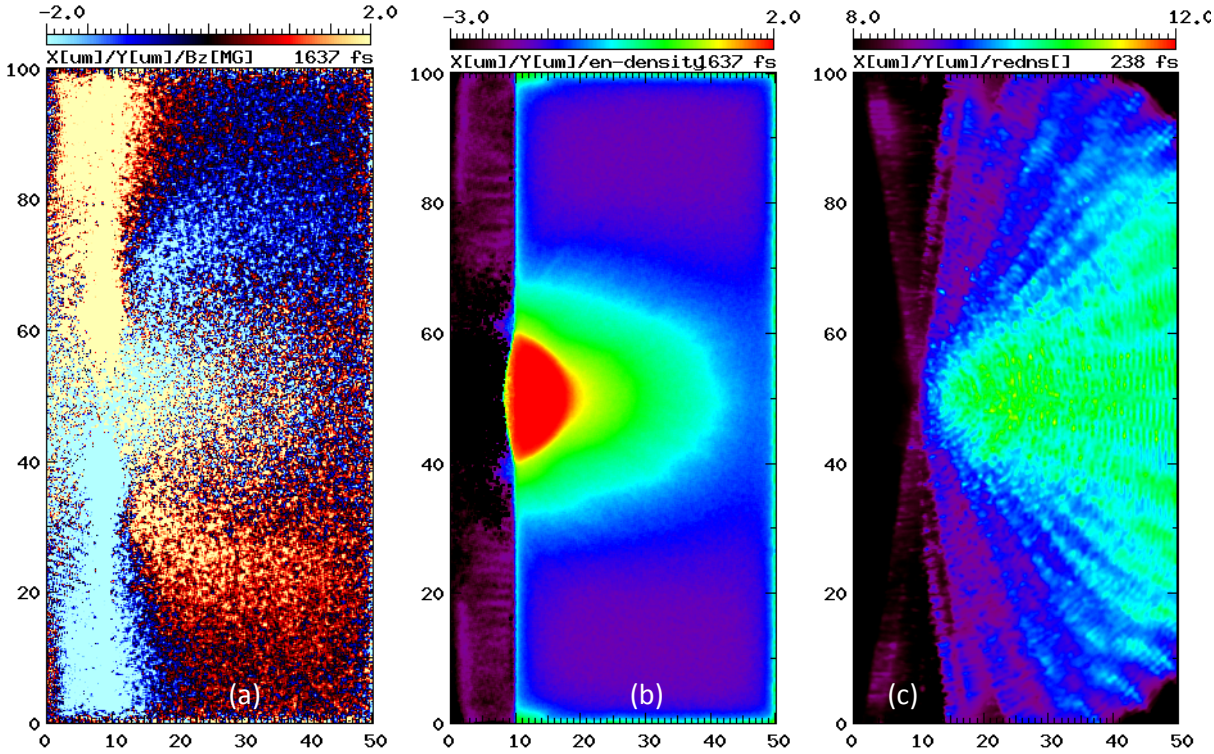

Figure 3.7: (color) 2D-PICLS results at laser intensity $5 \times 10^{19}\,\mathrm{W/cm^2}$ of (a) instantaneous magnetic fields [MG], (b) electron energy density [MeV$\cdot n_e/100n_c$ logarithmic scale], (c) γ-ray energy density, logarithmic scale]

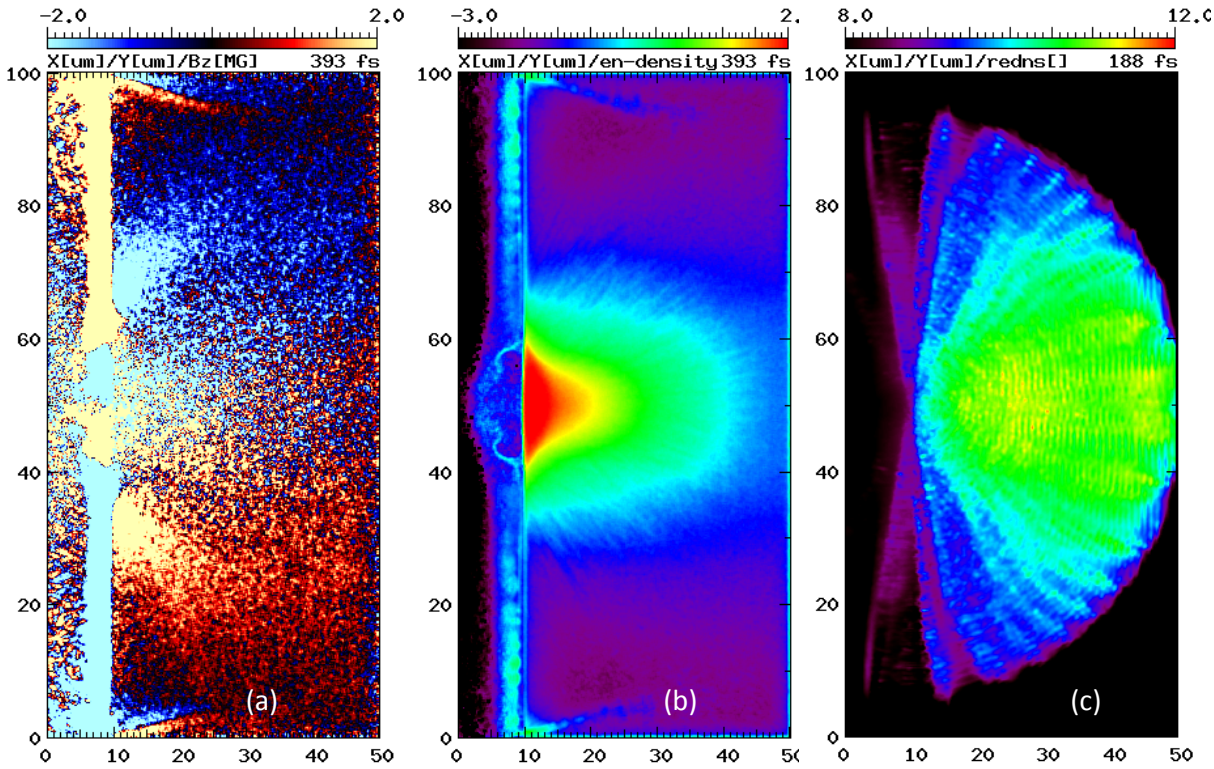

Figure 3.8: (color) 2D-PICLS results at laser intensity $10^{20}\,\mathrm{W/cm^2}$ of (a) instantaneous magnetic fields [MG], (b) electron energy density [MeV·$n_e/100n_c$ logarithmic scale], (c) γ-ray energy density, logarithmic scale]

an intensity $I = 10^{21}\,\mathrm{W/cm^2}$, a 66 fs pulse duration, and a $8\sqrt{10}\,\mu$m spot where (a) is the instantaneous magnetic fields [MG] at 393 fs (b) is the electron energy density in logarithmic scale at 393 fs and (c) is the γ-ray electron density in logarithmic scale at 182 fs. In (a) strong dipole magnetic fields appear inside the target. In (b) we can see the distribution of energy of electrons inside the target and in (c) we can see the energy density range of γ-ray as well angular distribution of radiation. Most of the γ-rays are scattered hemispherically in forward direction.

In Figure 3.10, we show a 2D simulation using a laser pulse with an intensity $I = 10^{22}\,\mathrm{W/cm^2}$, a 6 fs pulse duration, and a $8\sqrt{10}\,\mu$m spot where (a) is the instantaneous magnetic fields [MG] at 393 fs (b) is the electron energy density in logarithmic scale at 393 fs and (c) is the γ-rays energy density in logarithmic scale at 182 fs. In (a) strong dipole magnetic fields appear inside the target. In (b) we can see the distribution of energy of electrons inside the target and in (c) we can see the energy density range of γ-rays as well angular distribution of radiation. Most of the γ-rays are scattered hemispherically in forward direction. Most of the γ-rays are scattered hemispherically in forward direction.

In Figure 3.11, we show a 2D simulation using a laser pulse with

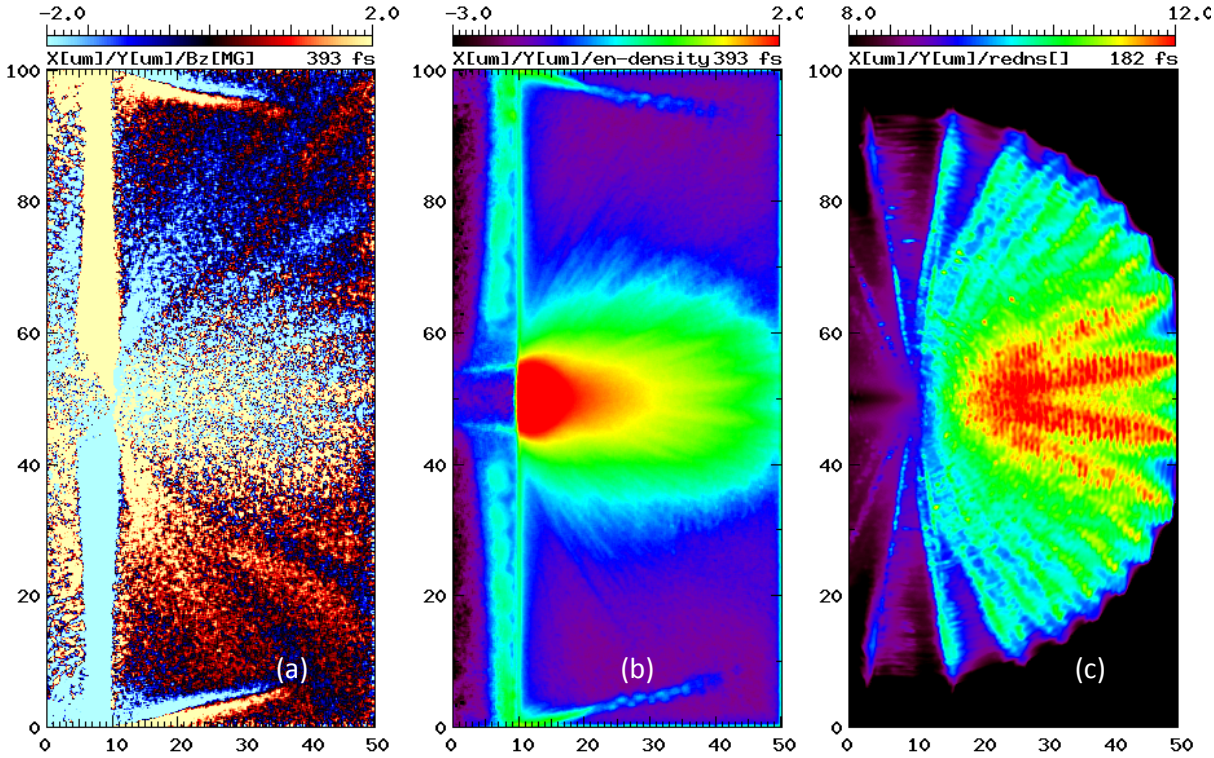

Figure 3.9: (color) 2D-PICLS results at laser intensity $10^{21}\,\mathrm{W/cm^2}$ of (a) instantaneous magnetic fields [MG], (b) electron energy density [MeV·$n_e/100n_c$ logarithmic scale], (c) γ-ray energy density, logarithmic scale]

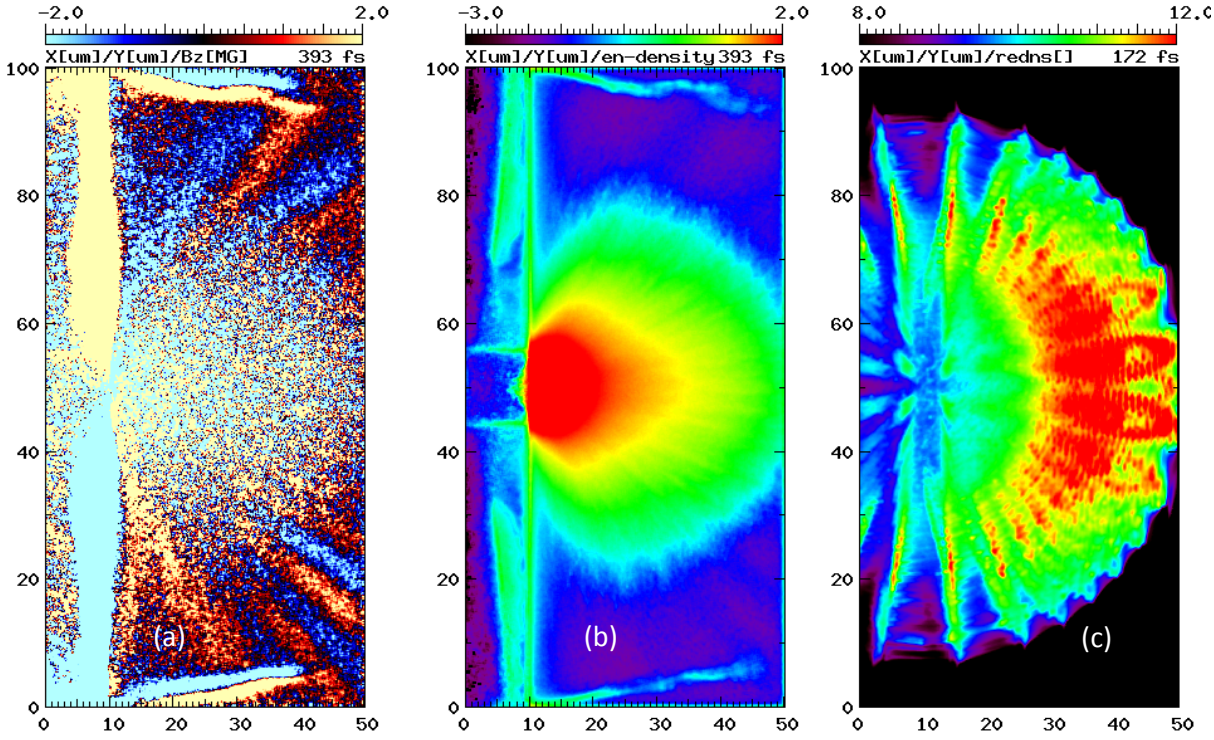

Figure 3.10: (color) 2D-PICLS results at laser intensity 10^{22} W/cm^2 of (a) instantaneous magnetic fields [MG], (b) electron energy density [MeV·$n_e/100n_c$ logarithmic scale], (c) γ-ray energy density, logarithmic scale]

an intensity $I = 10^{23}\,\mathrm{W/cm^2}$, a 6 fs pulse duration, and a $8\sqrt{100}\,\mu$m spot where (a) is the instantaneous magnetic fields [MG] at 393 fs (b) is the electron energy density in logarithmic scale at 393 fs and (c) is the γ-rays energy density in logarithmic scale at 182 fs. In (a) strong dipole magnetic fields appear inside the target. In (b) we can see the distribution of energy of electrons inside the target and in (c) we can see the energy density range of γ-rays as well angular distribution of radiation. Most of the γ-rays are scattered hemispherically in forward direction.

Low energy photon spectrum(from 10 KeV to 100 KeV) with laser intensities $10^{18}\,\mathrm{W/cm^2}$ and $10^{19}\,\mathrm{W/cm^2}$ are shown in Figure 3.12. As intensity increases, photon energy also increases. High energy tails of photon spectrum at different intensities are clearly seen in the figure.

In Figure 3.13 we compare γ-ray energy density at $10^{18}\,\mathrm{W/cm^2}$ and $10^{19}\,\mathrm{W/cm^2}$ for low energy photon. As laser intensity increase from $10^{18}\,\mathrm{W/cm^2}$ to $10^{19}\,\mathrm{W/cm^2}$ photon spectrum is increased by 10^2 order of magnitude. By comparing Figure 3.13, Figure 3.4(c) and Figure 3.6(c) we conclude that high energy photons are co-moving with the fast moving electrons and keep intensifying while the low energy photons are escape out.

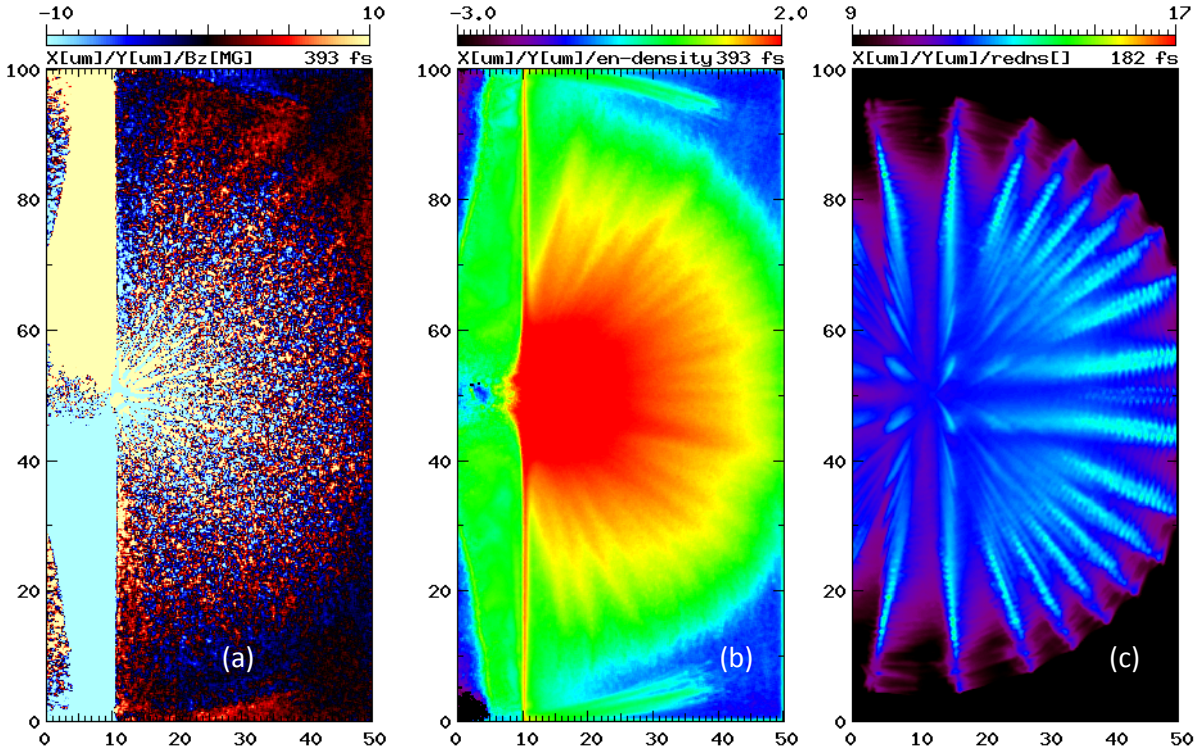

Figure 3.11: (color) 2D-PICLS results at laser intensity $10^{23}\,\mathrm{W/cm^2}$ of (a) instantaneous magnetic fields [MG], (b) electron energy density [MeV·$n_e/100n_c$ logarithmic scale], (c) γ-ray energy density, logarithmic scale]

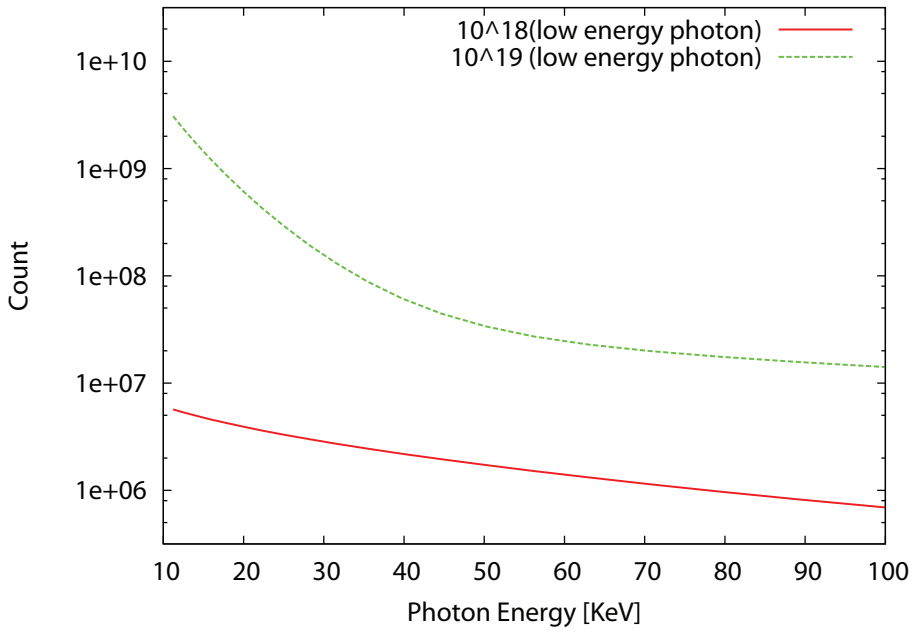

Figure 3.12: (color) 2D-PICLS results; comparison of low energy photon spectrum by Bremsstrahlung at laser intensities $10^{18}\,\mathrm{W/cm^2}$ and $10^{19}\,\mathrm{W/cm^2}$ of ultra-fast heated copper thick target

The plot of radiation efficiency(percentage) versus laser intensity via Bremsstrahlung is shown in Figure 3.14. From laser intensity $10^{18}\,\mathrm{W/cm^2}$ to $10^{20}\,\mathrm{W/cm^2}$ radiation efficiency is proportional to intensity of the laser which is consistent with Figure 11 of [67]. This scaling decreases from laser intensity $10^{21}\,\mathrm{W/cm^2}$ to $10^{23}\,\mathrm{W/cm^2}$ because there is less absorption(Figure 4.25) as well as high energy electrons are damped by radiative damping.

The plot of number of pairs per Joule versus laser intensity is shown in Figure 3.14. From laser intensity $10^{18}\,\mathrm{W/cm^2}$ to $10^{20}\,\mathrm{W/cm^2}$ number of pairs per joule is proportional to $I^{1.5}$ which is consistent with

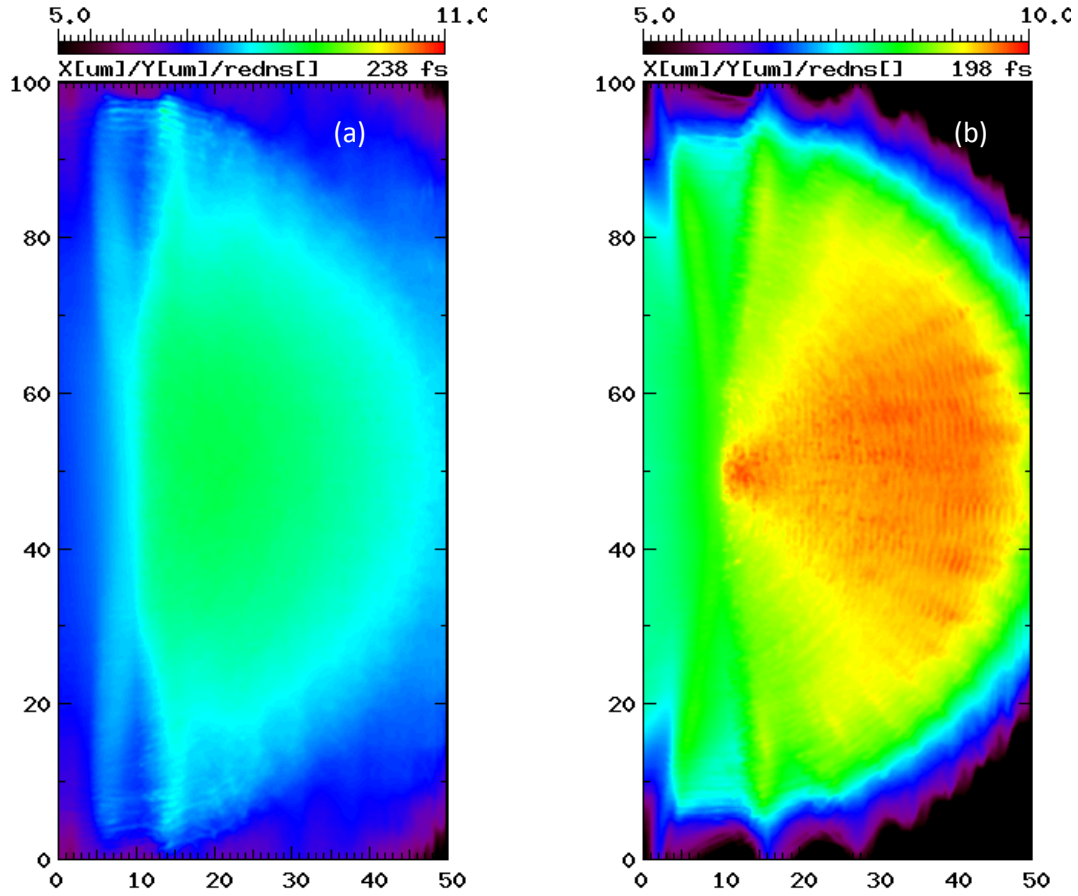

Figure 3.13: (color) 2D-PICLS results; (a) γ-ray energy density at $10^{18}\,\mathrm{W/cm^2}$ for low energy photon, logarithmic scale,(b) γ-ray energy density at $10^{19}\,\mathrm{W/cm^2}$ for low energy photon, logarithmic scale]

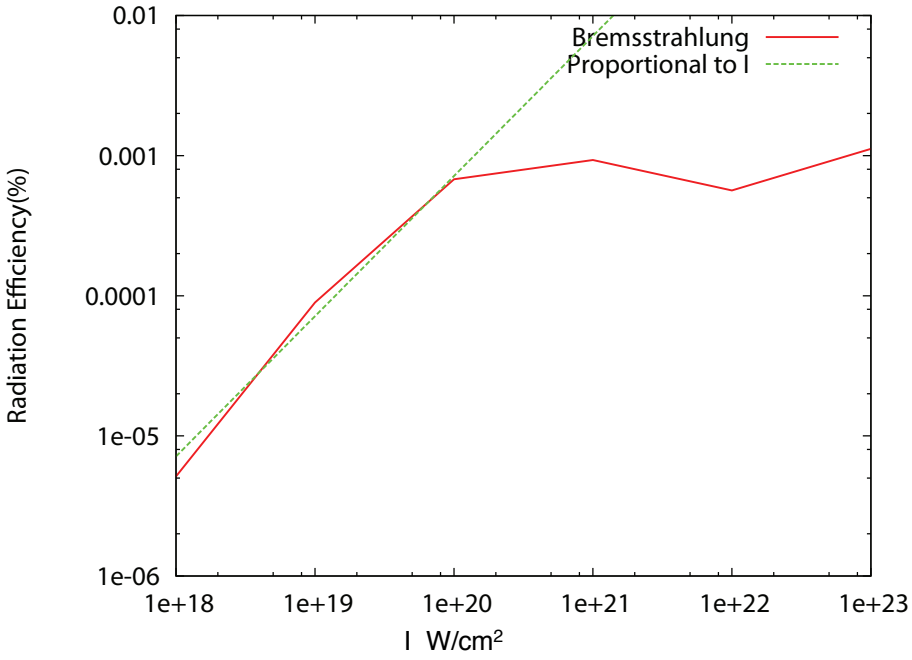

Figure 3.14: (color) 2D-PICLS results; Bremsstrahlung in intensity vs percentage radiation efficiency graph of ultra-fast heated copper thick target.

Figure 10 of [67]. From laser intensity $10^{20}\,\mathrm{W/cm^2}$ to $10^{23}\,\mathrm{W/cm^2}$ number of pairs per joule is proportional to $I^{0.3333}$. At higher intensity, the scale is dropping from the $I^{1.5}$ because there is less absorption(Figure 4.25) as well as high energy electrons are damped by radiative damping.

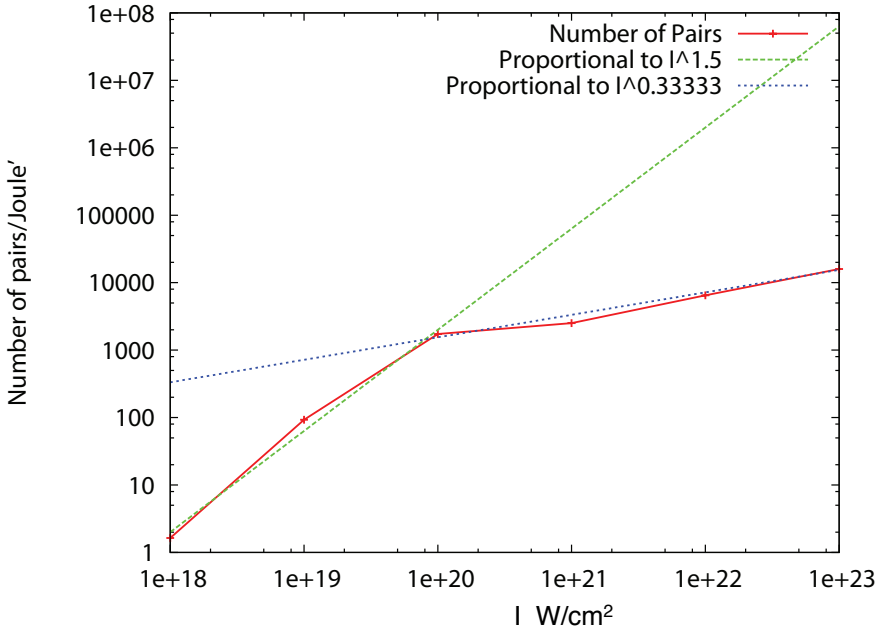

Figure 3.15: (color) 2D-PICLS results; variation of number of pairs per Joule with intensities via Bremsstrahlung of ultra-fast heated copper thick target.

3.4 Discussion and Conclusion of Bremsstrahlung and Pair Production

In conclusion, We have implemented the radiation cross-section of relativistic Bremsstrahlung and that of Bethe-Heitler pair production to simulate γ-ray production and their transport in ultrafast heated high Z matter by an intense short pulse laser. γ-rays are produced due to the Bremsstrahlung of electrons accelerated by the intense laser on the surface. We discuss the laser energy dependence of the emission energy and the intensity dependence of the angular distribution of γ-rays. By

solving the transport of γ-rays we find that high energy photons emitted by relativistic electrons are co-moving with the electrons and they are intensified continuously. As a result the γ-rays have the signature of the fast electrons temporal and spatial distribution. In terms of angular distribution of γ-rays, most of the γ-rays are scattered hemispherically in forward direction. We found that from the lower intensity simulations that Bremsstrahlung γ-ray emissions are increase continuously. However at $I > 10^{23}\,\mathrm{W/cm^2}$, Bremsstrahlung emissions start to saturate. From laser intensity $10^{18}\,\mathrm{W/cm^2}$ to $10^{20}\,\mathrm{W/cm^2}$ radiation efficiency is proportional to intensity of the laser. From laser intensity $10^{18}\,\mathrm{W/cm^2}$ to $10^{20}\,\mathrm{W/cm^2}$ number of pairs per joule is proportional to $I^{1.5}$. From laser intensity $10^{20}\,\mathrm{W/cm^2}$ to $10^{23}\,\mathrm{W/cm^2}$ number of pairs per joule is proportional to $I^{0.3333}$.

Chapter 4 Radiative Damping

4.1 Introduction

With the advent of high-powered, short pulse lasers, it becomes possible to extend laser intensities to 10^{21} W/cm^2. By applying a micro-focusing device such as the recently developed elliptical plasma mirror, it is possible to focus the beam to a micron-scale spot, thus enhancing the intensity more than an order of magnitude [52]. In a few years, the intensity on target will exceed 10^{22} W/cm^2, and electrons accelerated by such an intense laser field will reach energies beyond 100 MeV and start to strongly emit radiation. Then the radiation loss from an accelerated electron will no longer be negligible and will affect its motion, so-called *radiative damping*.

In order to study the effects of the radiative damping, a code was developed to solve a set of equations describing the evolution of a strong electromagnetic wave interacting with a single electron. Usually the equation of motion of an electron including radiative damping under the influence of electromagnetic fields is derived from the Lorentz-Abraham-Dirac (LAD) equation treating the damping as a

perturbation [53]. First order correction of the Lorentz-Abraham-Dirac (LAD) equation is known as Landau-Lifshitz (LL) equation. Until now, only the first order damping equation of the LAD equation has been used [12, 54, 55, 56, 57, 58]. The second order terms are thought to be small in comparison with the first order terms, and also deriving the second-order terms is challenging. For single particle calculation, in Ref. [59] the LAD equation was numerically solved for the stationary solution and in Ref. [60] it was numerically solved backward in time. In both references [59] and [60] it is found that there is the small deviations in LAD and LL equations in classical regime for single particle. However, since small deviation might be enhanced by collective effects in laser plasma interactions, the LL equation alone might not be sufficient to describe the motion of particles in a classical regime. Therefore, we have derived up to the fourth order terms, which are the largest contribution in each order, and have tested them by implementing up to the 2nd order term in a laser-plasma simulation code.

We have decided to use the LAD equation to study radiative damping. The LAD equation is based on classical electrodynamics, and its applicability to the extreme intense laser-matter interaction regime should be checked. The same discussion using the condition of the Schwinger parameter is in Ref. [59]. Quantum effects become important

for an electron accelerated to the relativistic energies within a length of the Compton wavelength $\lambda_C = \hbar/mc$, where m is the electron mass. So the critical electric field for quantum electrodynamics is called the Schwinger field E_S and is given by

$$E_S = \frac{m^2c^3}{e\hbar}. \tag{4.1}$$

Laser light with this electric field E_S has an intensity $I \simeq 10^{29}\,\mathrm{W/cm^2}$. The dimensionless parameter χ is defined as $\chi \equiv E/E_S$. As a simple estimate, we can say that if $\chi \ll 1$, classical electrodynamics is applicable. In order to discuss the dimensionless parameter χ for an electron moving with relativistic velocity in strong electromagnetic waves, it is convenient to rewrite it in terms of the Lorentz and gauge invariant parameter,

$$\chi = \frac{[(F^{ik}u_k)^2]^{1/2}}{E_S}. \tag{4.2}$$

Where, $u^i = \begin{bmatrix} \gamma \\ \beta_x\gamma \\ \beta_y\gamma \\ \beta_z\gamma \end{bmatrix}$ and $F^{ik} = \begin{bmatrix} 0 & -E_x & -E_y & -E_z \\ E_x & 0 & -B_z & B_y \\ E_y & B_z & 0 & -B_x \\ E_z & -B_y & B_x & 0 \end{bmatrix}$

Eq. (4.2) is rewritten in terms of the electric and magnetic fields and electron momentum P as

$$\chi = \frac{[(mc\gamma\mathbf{E} + \mathbf{P}\times\mathbf{B})^2 - (\mathbf{P}\cdot\mathbf{E})^2]^{1/2}}{mcE_S}. \tag{4.3}$$

From this equation, the dimensionless parameter is then estimated as $\chi = \gamma(1 - \beta_{\parallel})E/E_S$ for the electron in a plane electromagnetic wave, here $\beta_{\parallel}$ is the velocity along the wave propagation [58, 59]. This means χ is getting close to unity when $I \sim 10^{24}\,\mathrm{W/cm^2}$ with $\gamma(1 - \beta_{\parallel}) > 300$. In a relativistic laser-plasma interaction, electrons are mainly accelerated in the laser propagation direction, namely, $1 - \beta_{\parallel} \ll 1$, so that the threshold γ should be much greater than 300 for an intensity of $10^{24}\,\mathrm{W/cm^2}$. We are now focusing on laser-matter interactions below this intensity where the classical approach is assumed to be valid. In the regime $I > 10^{24}\,\mathrm{W/cm^2}$ where the classical approach is not applicable anymore, the non-perturbative generalizations of the LAD equation that account for quantum effects has been proposed by Sokolov *et al.* [65].

In the next section, we derive the full set of damping terms up to 4th order, and apply them to particle-in-cell simulations in Sec. 4.3.

4.2 Derivation of radiative damping terms

The radiative damping effect is ascribed to the physics of relativistic electron beams. It is usually negligible in overdense plasmas where

the laser fields are usually weak, while in underdense plasmas it is important because electrons are directly accelerated by the strong fields. The amount of energy emitted as radiation is negligible in the nonrelativisitic regime ($I < 10^{18}\,\mathrm{W/cm^2}$), but not in the strong relativistic regime ($I > 10^{18}\,\mathrm{W/cm^2}$). Relativistically, the equation of motion of the radiating electron is written in a four-dimensional form [53],

$$mc\,\frac{du^i}{ds} = \frac{e}{c}\,F^{ik}u_k \;+\; g^i\;, \tag{4.4}$$

where $m(e)$ is electron mass (charge), c is the speed of light, ds is the line element in four-dimensional space ($ds = \;cdt/\gamma$), u^i is the *i-th* component of the four velocity, F^{ik} is the electromagnetic field tensor, and g^i is the damping term given by

$$g^i \;= \frac{2e^2}{3c}\left[\frac{d^2u^i}{ds^2} - \;u^iu^k\;\frac{d^2u_k}{ds^2}\right]. \tag{4.5}$$

This equation describes the damping of a relativistic electron interacting with an electromagnetic field. To solve the equation of motion, we can re-express the damping term in terms of the fields. This can be done through a perturbation expansion of the equation of motion. If the damping term g^i in Eq. (4.4) is a small perturbation, then the zeroth order acceleration can be written as [60]

$$\left(\frac{du^i}{ds}\right)_0 = \frac{e}{mc^2}\;F^{ik}u_k\;, \tag{4.6}$$

where the RHS is the Lorentz force. The subscript 0 represents the zeroth order term. Then, Eq. (4.4) and Eq. (4.6) can be written as,

$$\left(\frac{du^i}{ds}\right)_1 = \left(\frac{du^i}{ds}\right)_0 + \frac{2e^2}{3mc^2}\ g_1^i\ , \tag{4.7}$$

and

$$g_1^i\ = \left[\left(\frac{d^2u^i}{ds^2}\right)_0 -\ u^iu^k\ \left(\frac{d^2u_k}{ds^2}\right)_0\right]. \tag{4.8}$$

The subscript 1 represents the first order term. In the same way we can write the second order equation as

$$\left(\frac{du^i}{ds}\right)_2 = \left(\frac{du^i}{ds}\right)_1 + \frac{2e^2}{3mc^2}\ g_2^i\ , \tag{4.9}$$

and

$$g_2^i\ = \left[\left(\frac{d^2u^i}{ds^2}\right)_1 -\ u^iu^k\ \left(\frac{d^2u_k}{ds^2}\right)_1\right]. \tag{4.10}$$

The subscript 2 represents the second order term. By repeating the same operations, we can obtain the higher order terms. The equation of motion including the damping terms is

$$\frac{d\gamma\beta}{dt} = \frac{e}{mc}(\mathbf{E} + \beta \times \mathbf{B}) + \sum_{i=1}^{\infty}\left(\frac{2e^2}{3mc^2}\right)\ \mathbf{g_i}\ , \tag{4.11}$$

where γ is the relativistic Lorentz factor and β is the normalized velocity. See the appendix for more details.

Following are the steps to derive the damping terms up to the 4th order. Differentiating Eq. (4.6) with respect to s and inserting the values in Eq. (4.8) , we have the 1st-order term $\mathbf{g_1}$ by re-expressing the

four dimensional form with the fields as

$$\begin{aligned}\mathbf{g_1} &= \left(\frac{e}{mc^2}\right)\gamma\left(\frac{\partial}{\partial t}+\ \mathbf{v}\cdot\nabla\right)(\ \mathbf{E}+\boldsymbol{\beta}\times\mathbf{B}) \\ &+\left(\frac{e}{mc^2}\right)^2 c\left[(\boldsymbol{\beta}\cdot\ \mathbf{E})\mathbf{E}+(\ \mathbf{E}+\boldsymbol{\beta}\times\mathbf{B})\times\mathbf{B}\right] \\ &-\left(\frac{e}{mc^2}\right)^2\gamma^2 c\boldsymbol{\beta}\left[(\ \mathbf{E}+\boldsymbol{\beta}\times\mathbf{B})^2-(\boldsymbol{\beta}\cdot\mathbf{E})^2\right]. \quad (4.12)\end{aligned}$$

Similarly, inserting g_1 in Eq. (4.7), differentiating it with respect to s and substituting the values in Eq. (4.10), we have the 2nd-order term $\mathbf{g_2}$ in terms of the fields as [62]

$$\begin{aligned}\mathbf{g_2} &= \left(\frac{2e^2}{3mc^2}\right)\left[\left(\frac{e}{mc^2}\right)\gamma^2\beta^2 c\left(\frac{1}{c^2}\frac{\partial^2}{\partial t^2}+\nabla^2\right)(\mathbf{E}+\boldsymbol{\beta}\times\mathbf{B})\right. \\ &+\ 2\left(\frac{e}{mc^2}\right)^2\gamma c\left[(\boldsymbol{\beta}\cdot\mathbf{E})\frac{1}{c}\frac{\partial}{\partial t}(\mathbf{E}-\boldsymbol{\beta}\times\mathbf{B})-(\mathbf{E}+\boldsymbol{\beta}\times\mathbf{B})\cdot\nabla(\mathbf{E}-\boldsymbol{\beta}\times\mathbf{B})\right] \\ &+\ \left(\frac{e}{mc^2}\right)^2\gamma c\left[(\boldsymbol{\beta}\cdot\mathbf{E})\frac{1}{c}\frac{\partial}{\partial t}(\mathbf{E}+\boldsymbol{\beta}\times\mathbf{B})-(\mathbf{E}-\boldsymbol{\beta}\times\mathbf{B})\cdot\nabla(\mathbf{E}+\boldsymbol{\beta}\times\mathbf{B})\right] \\ &+\ \left(\frac{e}{mc^2}\right)^3\ 2c(\ B^2-E^2\ )(\mathbf{E}+\boldsymbol{\beta}\times\mathbf{B}) \\ &+\ \left(\frac{e}{mc^2}\right)^2\gamma^3[\boldsymbol{\beta}\cdot(\mathbf{E}-\boldsymbol{\beta}\times\mathbf{B})-(\boldsymbol{\beta}\cdot\mathbf{E})]\left(\frac{\partial}{\partial t}+\mathbf{v}\cdot\nabla\right)(\mathbf{E}+\boldsymbol{\beta}\times\mathbf{B}) \\ &-\ 2\left(\frac{e}{mc^2}\right)^3\gamma^2 c[(\mathbf{E}+\boldsymbol{\beta}\times\mathbf{B})^2-(\boldsymbol{\beta}\cdot\mathbf{E})^2](\mathbf{E}+\boldsymbol{\beta}\times\mathbf{B}) \\ &+\ 2\left(\frac{e}{mc^2}\right)^2\gamma^3[(\boldsymbol{\beta}\cdot\mathbf{E})-\boldsymbol{\beta}\cdot(\mathbf{E}+\boldsymbol{\beta}\times\mathbf{B})]\left(\frac{\partial}{\partial t}+\mathbf{v}\cdot\nabla\right)(\mathbf{E}+\boldsymbol{\beta}\times\mathbf{B}) \\ &+\ 2\left(\frac{e}{mc^2}\right)^3\gamma^2 c\left[(\mathbf{E}+\boldsymbol{\beta}\times\mathbf{B})^2+(\boldsymbol{\beta}\cdot\mathbf{E})^2\right](\mathbf{E}-\boldsymbol{\beta}\times\mathbf{B}) \\ &-\ \left(\frac{e}{mc^2}\right)^3\gamma^4 c\beta^2\left[(\mathbf{E}+\boldsymbol{\beta}\times\mathbf{B})^2-(\boldsymbol{\beta}\cdot\mathbf{E})^2\right](\mathbf{E}+\boldsymbol{\beta}\times\mathbf{B})]. \quad (4.13)\end{aligned}$$

In Eq. (4.13), the higher order term is smaller than the previous order term by a factor of the classical electron radius $r_e \equiv e^2/mc^2 \sim 10^{-13}$

such that the 2nd-order term was previously thought to be negligible in comparison with the 1st-order term.

The magnitude of each damping term has been verified in both the 1st and 2nd-order equations for a particle interacting with a micron wavelength laser. In the 1st-order terms, a group of terms with a factor of γ^2 (third group in Eq. (4.12)) is the largest, and acts like friction on the electron motion. While in the 2nd-order terms, a group of terms with a factor of γ^4 (last group in Eq. (4.13)) has the largest contribution in damping the Lorentz force. Hereafter, we only use the third group of the 1st-order terms and the last group of the 2nd-order terms for laser-plasma interaction simulations. Note here that the terms with time derivative (1st term in $\mathbf{g_1}$ and $\mathbf{g_2}$) would be large for a particle motion interacting with x-ray which has extremely high frequency. Nevertheless, for laser-plasma interactions involving infra-red lasers, they are totally negligible.

Because the equations are already pretty complicated, we only take into account the largest damping terms of the four dimensional form (see Appendix A) to get the 3rd order and 4th order terms which corresponds to the last terms of Eq. (4.13) with γ^4 dependence. Then the 3rd order and 4th order terms are obtained as

$$\mathbf{g_3} = -\left(\frac{2e^2}{3mc^2}\right)^2 [\left(\frac{e}{mc^2}\right)^4 \gamma^6\beta^2 c \left[(\ \mathbf{E}+\boldsymbol{\beta}\times\mathbf{B})^2 - (\boldsymbol{\beta}\cdot\mathbf{E})^2\right]^2 \boldsymbol{\beta}], \tag{4.14}$$

and

$$\mathbf{g_4} = -\left(\frac{2e^2}{3mc^2}\right)^3 [\left(\frac{e}{mc^2}\right)^5 \gamma^8\beta^4 c \left[(\ \mathbf{E}+\boldsymbol{\beta}\times\mathbf{B})^2 - (\boldsymbol{\beta}\cdot\mathbf{E})^2\right]^2 (\mathbf{E}+\boldsymbol{\beta}\times\mathbf{B})]. \tag{4.15}$$

We estimate the laser intensity for which radiative damping becomes significant in comparison with the Lorentz force. In the order of magnitude estimation, the Lorentz force f_0 is approximately eE, using the normalized vector potential $a_0 \equiv eE/mc\omega_0$,

$$f_0 = \ mc\omega_0 a_0. \tag{4.16}$$

The third group of 1st-order terms f_1 is approximately

$$f_1 = \frac{2e^2\omega_0^2\gamma^2 a_0^2}{3c^2}, \tag{4.17}$$

then the last group of the 2nd-order terms f_2 is estimated as

$$f_2 = \frac{4e^4\omega_0^3\gamma^4 a_0^3}{9mc^5}, \tag{4.18}$$

Similarly, 3nd-order terms f_3 and 4th-order terms f_4 are written as

$$f_3 = \frac{8e^6\omega_0^4\gamma^6 a_0^4}{27m^2c^8}, \tag{4.19}$$

$$f_4 = \frac{16e^8\omega_0^5\gamma^8 a_0^5}{81m^3c^{11}}, \tag{4.20}$$

where ω_0 is the laser frequency. The ratio of the 1st-order term and the Lorentz force is then

$$\frac{f_1}{f_0} = \frac{2r_e\omega_0\gamma^2 a_0}{3c} = \ 1.18 \times 10^{-8}\gamma^2 a_0 \ . \tag{4.21}$$

If γ increases linearly with the laser amplitude ($\gamma = a_0$) under the plane wave assumption, f_1/f_0 reaches unity when $a_0 \sim 400$, which corresponds to $I \sim 10^{23}$ W/cm^2. If $\gamma = a_0^2/2$ ($\mathbf{J} \times \mathbf{B}$ acceleration), then $f_1/f_0 \simeq 1$ when $I \simeq 10^{21}$ W/cm^2. For laser-plasma interactions, γ scales in the intermediate regime between these two cases. Therefore, the radiative damping starts at $I \sim 10^{22}$ W/cm^2.

Generally, the ratio of the adjacent higher order terms can be generalized as

$$\frac{f_{i+1}}{f_i} = \frac{2r_e\omega_0\gamma^2 a_0}{3c} = \ 1.18 \times 10^{-8}\gamma^2 a_0 \ , i = 0, 1, 2, 3, ... \tag{4.22}$$

Note here that although this gives the critical laser intensity above which the damping terms are no longer negligible, these are just simple scalings. For the actual interaction, f_1 will never be greater than f_0, and f_2 will never overcome f_1 since electrons keep losing energy via radiative damping before they reach these limits.

4.3 Simulation of super intense laser-matter interaction

We have implemented the 1st-order term (3rd group in Eq. (4.12)) and the 2nd-order damping term (last group in Eq. (4.13)) in the Particle-in-Cell (PIC) code in order to study radiation effects in the super intense laser - matter interaction for extreme intensity, $I \geq 10^{22}\,\mathrm{W/cm^2}$. The numerical code used is the one- & two-dimensional (PIC) code PICLS [50], which features binary collisions between charged particles and ionization processes in gaseous and solid density plasmas [63]. We have implemented the friction force (1st-order) and the damping of the Lorentz force (2nd-order) equations within the leap-frog scheme (time centered scheme) to integrate the kinetic equation. The friction (1st order) is taken into account at the centered time, and damping of the Lorentz force (2nd order) is simply done by reducing the Lorentz force by a factor calculated by the equation.

The target is modeled as a 5μm thick copper slab with uniform density. A few micron thick preplasma is placed in front of the target. The ion density is set to $50n_c$, here $n_c = 10^{21}\,\mathrm{cm^{-3}}$ is the critical density for a laser wavelength 1μm. The mass (fully ionized charge) of Cu is $64M_p$ (29), where M_p is the proton mass. Then the mass density of the target is set to $\rho = 5.3\,\mathrm{g/cm^3}$, close to the mass density of solid copper.

Initially we set the ion charge state $Z = 3$, and electron density is set to neutralize ion charges. We placed a $5\,\mu$m preplasma in front of the target with an exponential profile of a $2\,\mu$m scale length and a $50\,n_c$ peak density for electrons when the preplasma gets fully ionized. In total, 340200 particles are used for a fully ionized target of which 189000 make up the preplasma. This results in a cell density of 9 ions and 261 electrons per cell.

The ionization models include field driven ionization in low density plasmas under strong fields and impact ionization which solves for the collisional cross section in dense plasmas [51]. The electron density increases dynamically during laser irradiation via ionization processes. The ionization energies are subtracted from the hot electrons when they ionize atoms via collisions with bound electrons. Initially particles are at rest, with initial plasma temperature set to zero. Our spatial (temporal) resolution is 1/140 of the wavelength (laser oscillation period τ). The simulation also accounts for the energy loss by emission of soft x-ray radiation from free-bound transition, though it is only a minor effect (less than 0.3% of the laser energy) under the current simulation condition.

First, 1D simulations were performed to see the effect of radiative damping by the 1st order term alone and then by the 1st +

2nd order terms where we specifically looked at electron and ion phase space, energy spectrum and energy density. The laser intensity is varied from 10^{19} to $10^{24}\,\mathrm{W/cm^2}$ while keeping the pulse duration constant at 100 fs, namely, the laser energy increases with intensity.

Figure 4.1 shows the phase plot and energy spectrum of electrons with and without radiative damping at 181.5 fs when the pulse peak hits the target with an intensity of $I = 10^{23}\,\mathrm{W/cm^2}$. Strong damping of high energy electrons ($p_x/m_e c > 1000$) in the phase plots are observed at this time. The 2nd order damping term also has a small contribution to the overall damping which can be seen in the electron energy spectrum plot (blue-line).

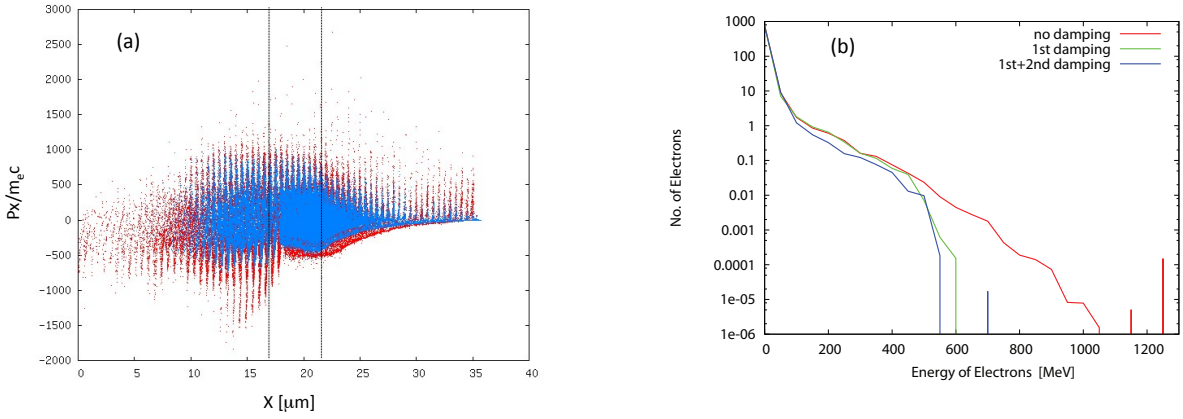

Figure 4.1: 1D-PIC result with $I = 10^{23}\,\mathrm{W/cm^2}$: (a) Distribution of electrons in phase space with no radiative damping (Red) and with 1st + 2nd order radiative damping (blue) at t = 181.5 fs when the pulse peak hit the target (b) Comparison of electron energy spectrum among three cases at the same time.

Figure 4.2 shows the phase plot and energy spectrum of electrons with and without radiative damping at 214.5 fs when the pulse starts to be reflected. Strong damping of high energy electrons, especially those that are accelerated backward by the reflected pulse ($|p_x/m_e c| > 1000$), are observed in the phase plots at this time. The 2nd order damping term has a significant impact on radiative damping as seen in the electron energy spectrum plot. At this time the laser pulse starts to be reflected and electrons co-moving with the pulse can interact in longer time with fields, since then we can see the 2nd-order damping effect more significantly.

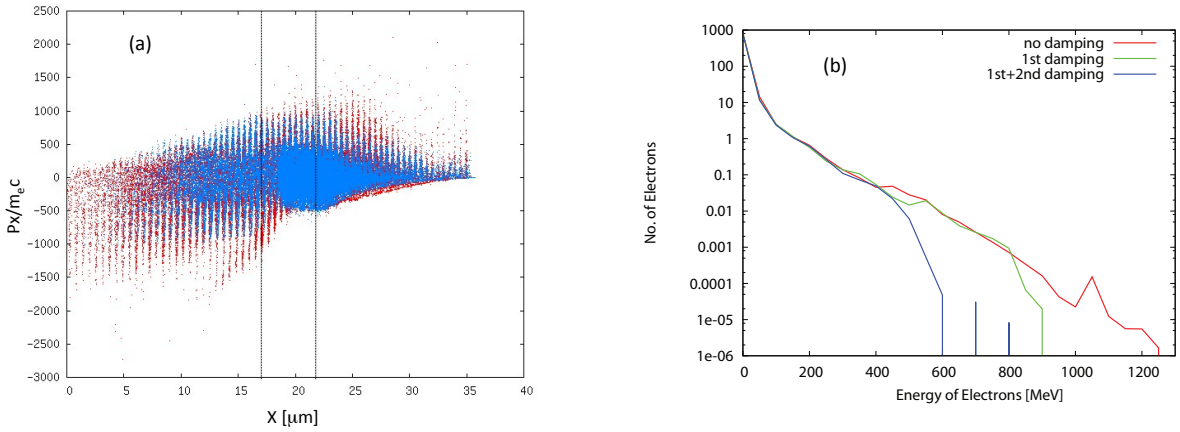

Figure 4.2: 1D-PIC result with $I = 10^{23}\,\mathrm{W/cm^2}$: (a) Distribution of electrons in phase space with no radiative damping (Red) and with 1st + 2nd order radiative damping (blue) at t = 214.5 fs when the pulse starts to be reflected (b) Comparison of electron energy spectrum among three cases at the same time.

Figure 4.3 (a) shows the phase plot of ions of the same laser

intensity at the same time with figure 4.1. The interface speed, which is determined by the photon pressure, is clearly seen to be slower in the case with 2nd-order damping compared to the one with the 1st-order term alone. As we discussed in the previous section, the 2nd order term reduces the Lorentz force, including the $J \times B$ force, so that the effective photon pressure decreases at the absorption point. This reduction of the ponderomotive force also affects the target heating or energy stored inside the target as seen in figure 4.3 (b). This result indicates that the 2nd-order term is important in the discussion of ion acceleration or the collisionless shock formation by the photon pressure with the laser intensity $\geq 10^{23}\,\mathrm{W/cm^2}$.

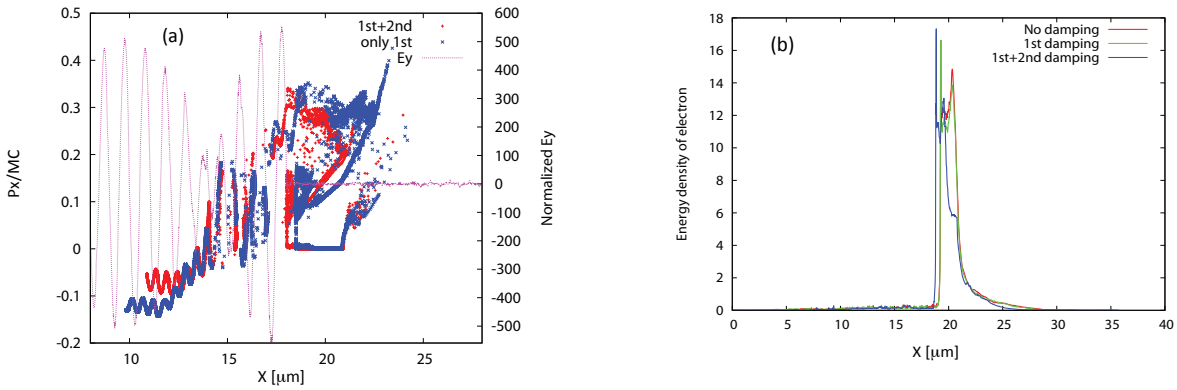

Figure 4.3: 1D-PIC result with $I = 10^{23}\,\mathrm{W/cm^2}$: (a) Longitudinal phase of ions at t = 181.5 fs when the pulse peak hits the target. (b) Electron energy density [MeV·$n_e/800n_c$] distribution observed at t = 214.5 fs when the pulse starts to be reflected.

Figure 4.4 shows the plot of laser intensity versus radiation ef-

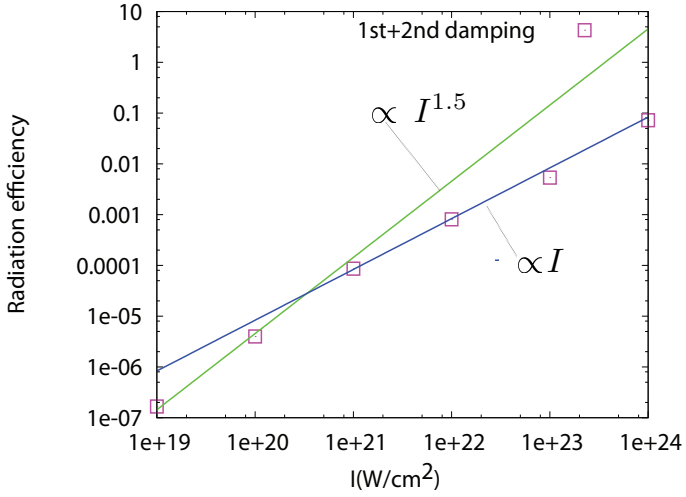

Figure 4.4: Laser intensity versus radiation efficiency.

ficiency, normalized energy by the incident laser energy. Radiation efficiency means conversion efficiency of laser light to radiated light. The radiation efficiency increases as $I^{1.5}$ in the range of laser intensities $I = 10^{19-20}\,\mathrm{W/cm^2}$ while it increases as I in the range of laser intensities $I > 10^{21}\,\mathrm{W/cm^2}$. Lasers with intensities below $10^{20}\,\mathrm{W/cm^2}$ interact with the pre-plasma, so that they have a higher scaling than that of the higher intensity pulses. When $I > 10^{20}\,\mathrm{W/cm^2}$, the laser pulse begins to interact directly with the solid surface. As a result, the hot electron energy scaling against the laser intensity drops due to the interaction at the sharp interface with electron densities reaching $n_e > 1000 n_c$ in the current setup [64].

The radiation power via radiative damping is compared with ra-

diations via Bremsstrahlung in the 1D simulations. A Bremsstrahlung model is used in the PICLS code which is solving the relativistic Bremsstrahlung equation by the Monte-Carlo method [67], and was recently modified for inline calculations by taking out the emission energy from electrons. The results are plotted in Fig. 4.5. We found that from the lower intensity simulations that Bremsstrahlung hard x-ray emissions are dominant. However at $I > 10^{22}\,\mathrm{W/cm^2}$, Bremsstrahlung emissions start to saturate and the radiative damping becomes a dominant source of hard x-rays. This is because of electrons in the high energy tail with large γ factors will be damped by radiative damping and thus cannot increase the Bremsstrahlung radiation emissions which scale as γ^4. Transition intensity (The laser intensity at which radiative damping is equal to Bremsstrahlung) of radiative damping and Bremsstrahlung is also decreases when we lower the Z of the target because if we lower the Z of the target, Bremsstrahlung is decreasing.

These results have a strong impact on pair production by laser-matter interaction at these extreme intensities ($> 10^{22}\,\mathrm{W/cm^2}$) since we have a large energy conversion to hard x-rays via the radiative damping processes, which can boost pair production via the Bethe-Heitler process [54, 68].

In order to check the classical limit, we calculate the χ param-

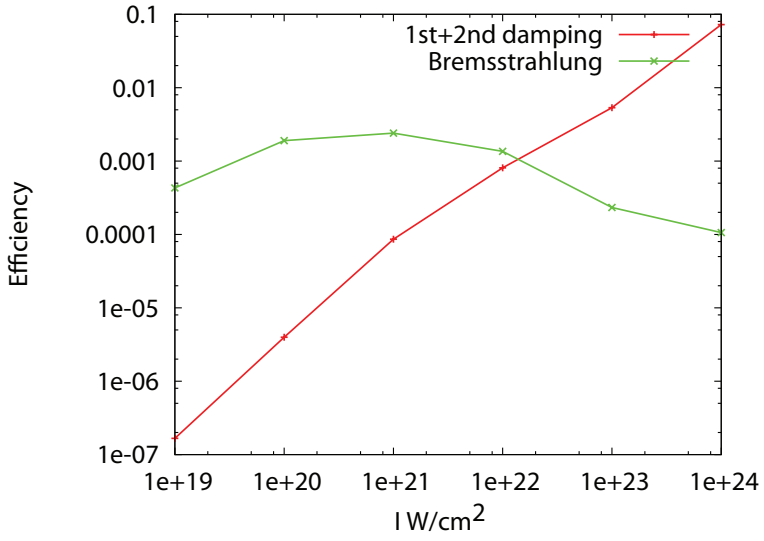

Figure 4.5: Comparison of radiation efficiencies between via the radiative damping and via the Bremsstrahlung by changing the laser intensity.

eter. Figure 4.6(a) shows the χ for each electrons at $I = 10^{23}\,\mathrm{W/cm^2}$ when the pulse peak hits the target. In figure 4.6(b) we also plot the number of electrons having $\chi > 1$ divided by the total number of electrons in the preplasma (number of electrons interacting with the laser light) by changing the laser intensity. From these graphs less than 0.015% electrons have χ greater than 1 at intensity $10^{23}\,\mathrm{W/cm^2}$. So, the intensity $10^{23}\,\mathrm{W/cm^2}$ starts to show the quantum effects, but they are still mostly in the classical regime.

We have also performed a 2D simulation using a laser pulse with an intensity $I = 10^{23}\,\mathrm{W/cm^2}$, a 100 fs pulse duration, and a $3\,\mu$m spot in order to see the multidimensional effects of extreme intensity interactions. The simulation parameters are basically the same as for 1D, and

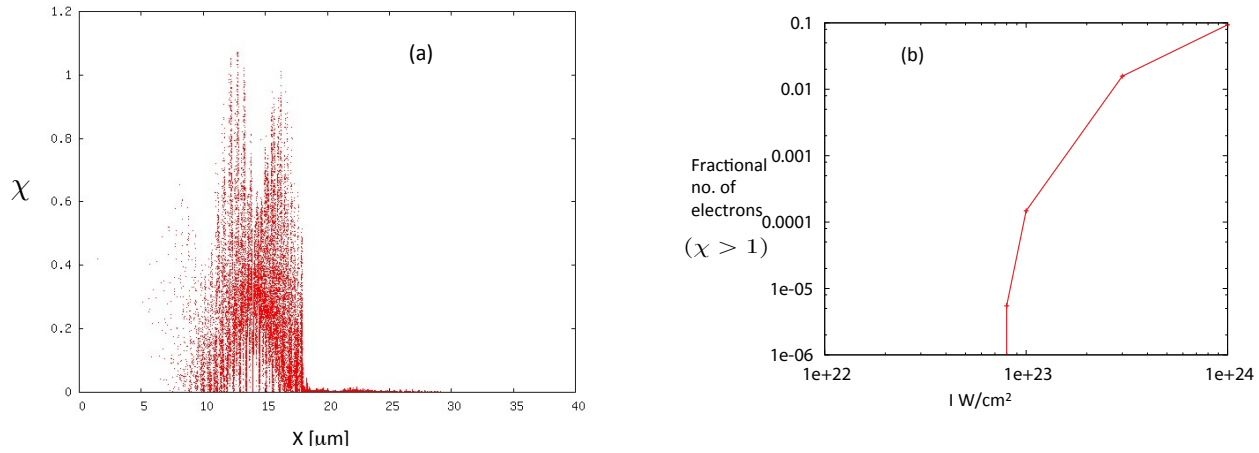

Figure 4.6: (a) Plot of χ versus position at $I = 10^{23}\,\mathrm{W/cm^2}$ when the pulse peak hit the target (b) Plot of number of electrons having $\chi > 1$ divided by the total no of electrons in preplasma versus laser intensity when the pulse peak hit the target.

both collision and ionization models were applied. We have included radiative damping up to the 2nd order term. The target, a copper slab with $5\,\mu$m thickness, as we used in the 1D simulations, is attached to the transverse boundaries. We apply an absorbing boundary condition for both particles and fields to simulate the large transverse volume of real targets. A pre-plasma with the same condition as in the 1D simulations is placed in front of the target. The temporal laser pulse profile is a Gaussian distribution. The pulse is irradiated from the left boundary and is focused on the target surface in a $3\,\mu$m spot.

Figure 4.7 shows snapshots at 250 fs when the irradiation is almost over. The surface magnetic field can be seen propagating laterally at nearly the speed of light. An extremely strong magnetic dipole with

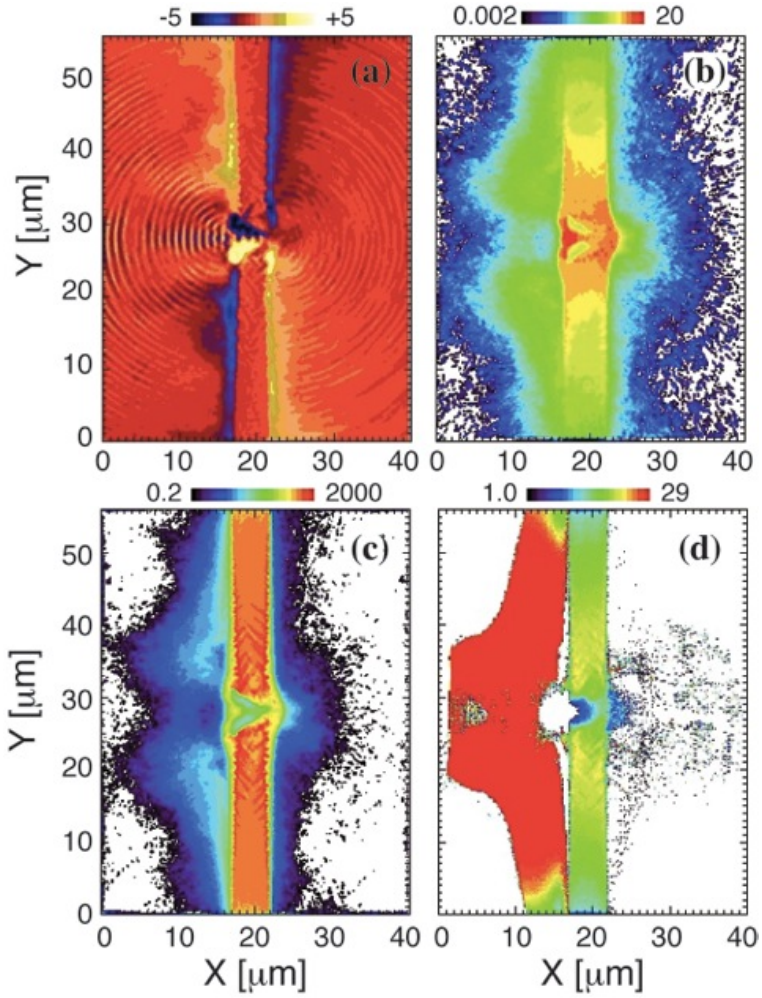

Figure 4.7: (color) 2D-PICLS results at 250 fs of (a) instantaneous magnetic fields [Gigagauss], (b) electron energy density [MeV·$n_e/100n_c$ logarithmic scale], (c) electron density [n_e/n_c, logarithmic cale], (d) average ionization degree $\bar{Z}$ of Cu

field strength $\sim$5 Gigagauss also appears inside the target, as seen in Fig. 4.7(a). Under such a strong magnetic field, the electron cyclotron frequency cloud exceeds $100\omega_0$, where ω_0 is the laser frequency. Because of the relativistic electron motion when $\gamma > 100$, the effective cyclotron frequency will be closer to ω_0. The simulation should also have sufficient resolution to track these cyclotron orbits. The current simulation resolution is $\tau/50$, which is fine enough to resolve the correct motion of electrons in such a strong magnetic field. Interestingly, this strong dipole magnetic field pushes the plasma, as seen in Fig. 4.7(c) and (d), but also traps extremely hot electrons inside the magnetic bubble, Fig. 4.7(b). The synchrotron radiation becomes significant in these regions.

Note here that the global trends of these results are basically the same and do not change much by omitting radiative damping in the simulation. The differences appear more clearly in plots of the electron energy spectra, as can be seen in Fig. 4.8. Strong damping of high energy electrons (> 1 GeV) is observed at the time when the pulse peak hits the target surface (150 fs), which is consistent with the 1D result.

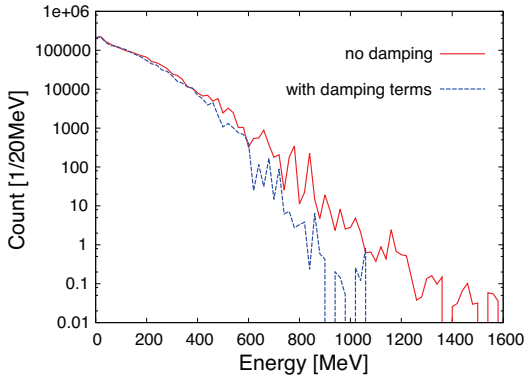

Figure 4.8: (color) 2D-PICLS results at 150 fs: Comparison of electron energy spectrum with and without damping.

4.4 Radiation power equation and angular distribution.

The radiation power equation for the specific photon energy is derived to calculate the emissivity in the radiation transport calculation. The angular distribution is also given. The emission power equation is derived by integrating the momentum equation, so that the equation should be consistent with the momentum calculation. We will benchmark the new equation in a single particle simulation in the next section.

4.4.1 Theory

We have derived the power radiated by 1st and 2nd order damping. Damping force multiplied by the velocity of light is the radiation power. In section 4.2, we derived damping force up to 4th order. So, Total

power radiated by the 1st order damping is

$$\mathbf{P_{1st}} = \left(\frac{2e^4}{3m^2c^3}\right)\gamma^2\beta\left[(\mathbf{E}+\boldsymbol{\beta}\times\mathbf{B})^2-(\boldsymbol{\beta}\cdot\mathbf{E})^2\right]. \quad (4.23)$$

Total power radiated by the 2nd order damping is

$$\mathbf{P_{2nd}} = \left(\frac{2e^2}{3mc^2}\right)^2\left(\frac{e^3}{m^2c^5}\right)\gamma^4c^2\beta\left[(\mathbf{E}+\boldsymbol{\beta}\times\mathbf{B})^2-(\boldsymbol{\beta}\cdot\mathbf{E})^2\right] |(\mathbf{E}+\boldsymbol{\beta}\times\mathbf{B})|. \quad (4.24)$$

The ratio of the power radiated by 2nd order damping and that of 1st order damping is

$$\frac{\mathbf{P_{2nd}}}{\mathbf{P_{1st}}} = 1.18\times10^{-8}\gamma^2a_0, \quad (4.25)$$

which is same as the ratio of the adjacent higher order terms of the momentum equation.

The differential cross-section of the emission power is then summarized as with the spectrum and angular direction of the emission,

$$\frac{dI}{d\omega d\Omega} = \delta\left(\Omega-\frac{\mathbf{p_e}}{p_e}\right)F\left(\frac{\omega}{\omega_c}\right)\frac{1}{\omega_c}(\mathbf{P_{1st}}+\mathbf{P_{2nd}}). \quad (4.26)$$

The angular distribution of the high energy γ- ray has a narrow peak in the direction of the electron momentum and can be approximated by the δ-function. The function F represents the frequency spectrum as

$$F(r) = 3^{5/2}(8\pi)^{-1}r\int_r^\infty K_{5/3}(r')dr', \quad (4.27)$$

where, r ($r = \omega/\omega_c$) is the normalized frequency by the maximum frequency ω_c which is given as

$$\omega_c = \frac{3}{2}\frac{eB}{mc}\gamma^3. \tag{4.28}$$

$K_{5/3}$ is a modified second order Bessel function. This frequency spectrum is applicable to synchrotron radiation as well as radiative damping in laser matter interaction.

When the wavelength of an electron is less than the compton wavelength($\lambda_C = \hbar/mc$), quantum electrodynamics (QED) effect becomes important. The physical meaning of QED effect is that an electron can not emit more than its own energy. In QED regime, χ could be closer or greater than unity, and which likely occurs with intensity of the laser greater than $10^{24}\,\mathrm{W/cm^2}$.The frequency spectrum in QED regime is [65, 69, 44, 70, 71].

$$F(r,\chi) = 3^{5/2}(8\pi)^{-1} r \left[\int_{r_\chi}^{\infty} K_{5/3}(r')dr' + r r_\chi \chi^2 K_{2/3}(r_\chi)\right], \tag{4.29}$$

where, $r_\chi = \frac{r}{(1-\chi r)}$ and $K_{2/3}$ is also a modified second order Bessel function. The second term in the above equations intend to cut off the high energy tail of the spectrum.

The integral of the spectral function is normalized by unity,

$$\int F(r)dr = 1. \tag{4.30}$$

Therefore, if we integrate Eq. (4.29) with respect to frequency and solid angle, we will get the total power radiated by 1st order and 2nd order damping.

4.5 Benchmark the emission power equation of radiative damping against the momentum damping

In this section we test the emission power equation of the radiative damping by comparing its result with the one by the momentum damping. Momentum damping means momentum of the electron is damped directly by 1st order and 2nd order damping terms, the emission power equation describes the energy loss in the damping process. As a test we calculate a single particle motion in an intense short laser pulse. We chose a Gaussian laser pulse with the form [60]

$$E(x,t) = \hat{y}E_0 h(\phi)\cos(2\pi(\omega t - kx)), \tag{4.31}$$

$$B(x,t) = \hat{z}B_0 h(\phi)\cos(2\pi(\omega t - kx)), \tag{4.32}$$

where the temporal phase $\phi = \omega_0(t - x/c)$, and the pulse profile function is

$$h(\phi) = \exp[-(\frac{\phi}{\omega_0 \Delta\tau})^2], \tag{4.33}$$

where $\Delta\tau$ is the pulse width, ω_0 is the laser frequency and $k = \omega/c$ is the wave number.

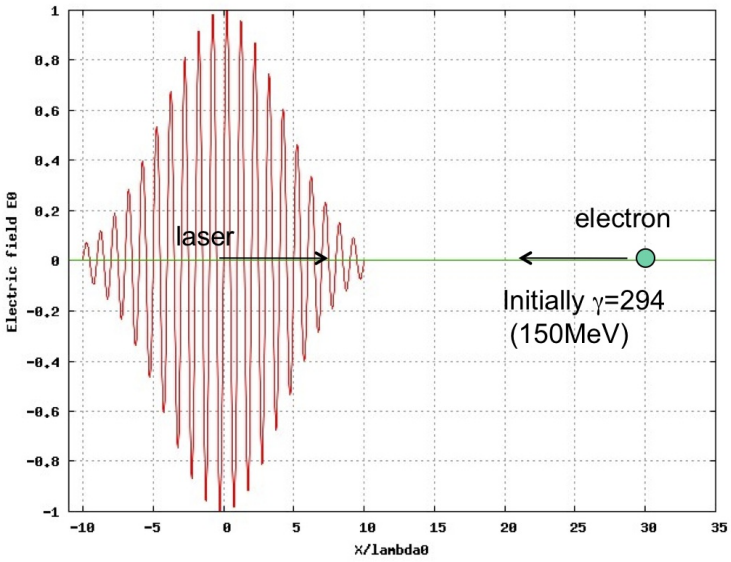

Figure 4.9: Numerical Experiment: Simulation of Single Particle Orbit-Radiative damping.

Figure 4.9 shows the initial setup of the simulation. In this figure, an intense laser pulse is propagating from left to right and a high energy electron of which energy is 150 MeV, is propagating from right to left. They interact with each other in the interaction region and the electron will lose its energy by the radiative damping via the intense laser fields.

In this simulation, the laser pulse of irradiance varies from 10^{20} W/cm^2 to 10^{23} W/cm^2. The Wavelength of the laser is 1 μm. The pulse width of the laser is 20 fs.

Figure 4.10 to 4.13 compare the trace of the electron's trajectory

in the normalized energy(γ)-time plane for a case of the momentum damping and cases of the emission power calculation without QED and with QED (Quantum) effects.

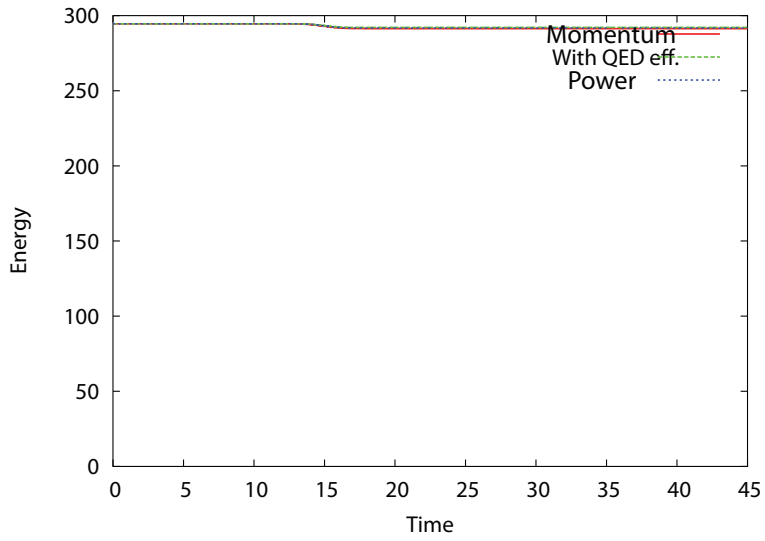

Figure 4.10: The trace of the electron motion in the energy(γ)-time(normalized by laser time period) plane for a case of the momentum damping and cases of the emission power calculation without QED and with QED (Quantum) effects at $10^{20}\,\mathrm{W/cm^2}$. Red is a case of the momentum damping, blue is a case of emission power calculation without QED effect and green is that with QED effect

Figure 4.10 and figure 4.11 show the results of the cases at laser intensity $10^{20}\,\mathrm{W/cm^2}$ and $10^{21}\,\mathrm{W/cm^2}$, respectively. At these intensities there is no significant difference among the three cases, so that the all curves are almost identical. The damped energy increases apparently by increasing the laser intensity.

Figure 4.12 and figure 4.13 show the results with the higher

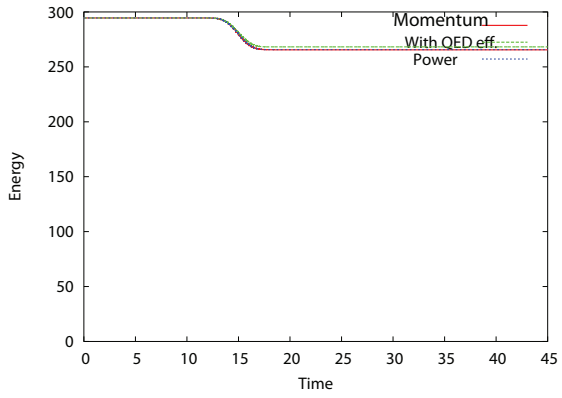

Figure 4.11: The trace of the electron motion in the energy(γ)-time(normalized by laser time period) plane for a case of the momentum damping and cases of the emission power calculation without QED and with QED (Quantum) effects at $10^{21}\,\mathrm{W/cm^2}$. Red is a case of the momentum damping, blue is a case of emission power calculation without QED effect and green is that with QED effect

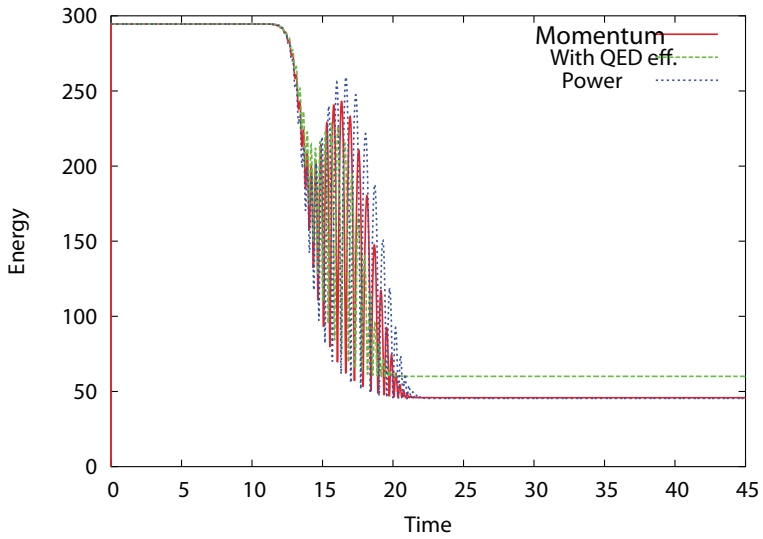

Figure 4.12: The trace of the electron motion in the energy(γ)-time(normalized by laser time period) plane for a case of the momentum damping and cases of the emission power calculation without QED and with QED (Quantum) effects at $5 \times 10^{22}\,\mathrm{W/cm^2}$. Red is a case of the momentum damping, blue is a case of emission power calculation without QED effect and green is that with QED effect

laser intensities, $5 \times 10^{22}\,\mathrm{W/cm^2}$ and $10^{23}\,\mathrm{W/cm^2}$ respectively. At these intensities the case of emission power calculation with the QED effect is slightly differed than the other two without the QED effect. Note here that the two cases having no QED effect, but damped by the different ways, momentum or power, have the similar results, which confirms our power loss equation is consistent with the momentum calculation.

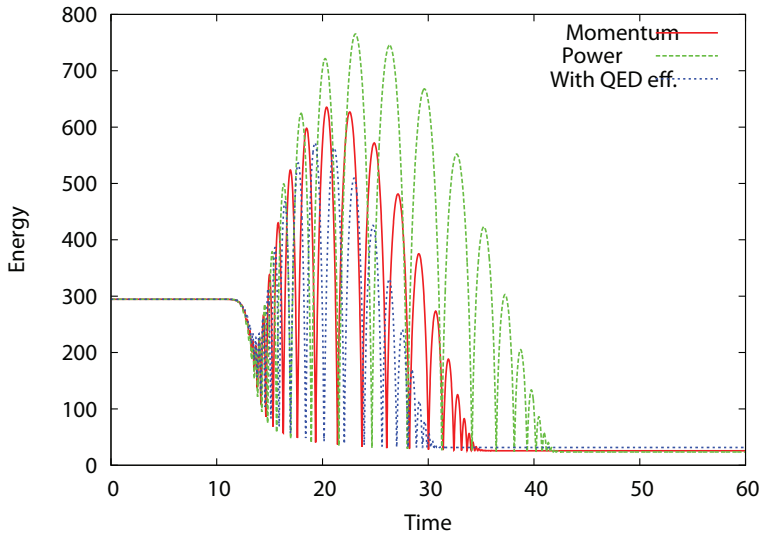

Figure 4.13: The trace of the electron motion in the energy(γ)-time(normalized by laser time period) plane for a case of the momentum damping and cases of the emission power calculation without QED and with QED (Quantum) effects at $10^{23}\,\mathrm{W/cm^2}$. Red is a case of the momentum damping, green is a case of emission power calculation without QED effect and blue is that with QED effect

Figure 4.14 is the total power versus photon energy curves at different intensities of laser light. As intensity increases, total power with respect to photon energy also increases as expected from the dependence of the damping, proportional to $E^2 \sim I$.

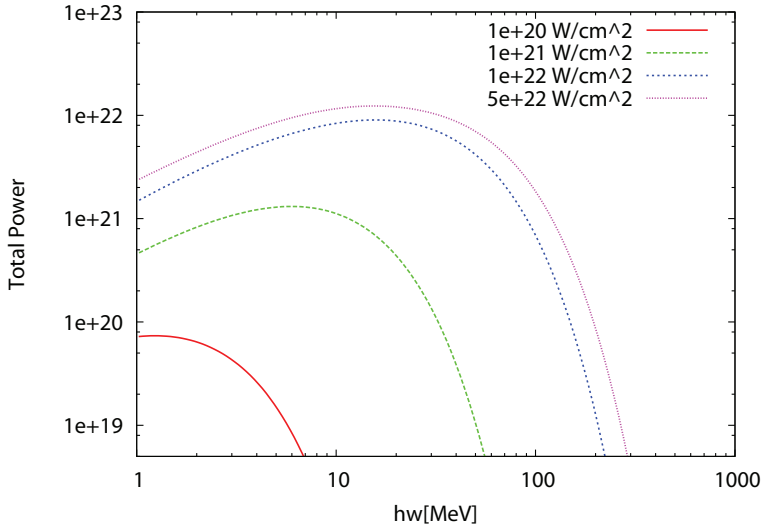

Figure 4.14: Total power of photon versus photon energy graph at different intensities of laser light.

4.5.1 Simulation of super intense laser-matter interaction

The numerical code used to study the extremely increase laser matter interaction is the one- & two-dimensional particle -in-cell (PIC) code PICLS [50], which features binary collisions between charged particles and ionization processes in gaseous and solid density plasmas. We had derived the radiative damping terms including the higher orders and implemented in PICLS. In order to evaluate the effect of radiation on the laser-produced plasma development, a radiation transport model coupled with a particle-in-cell code was developed. Pair production model for bremsstrahlung is also include in radiation transport code. The target is modeled as a 44μm thick copper slab with uniform density. A few micron thick preplasma is placed in front of the target. The

ion density is set to $50n_c$, here $n_c = 10^{21}\,\mathrm{cm}^{-3}$ is the critical density for a laser wavelength 1μm. The mass (fully ionized charge) of Cu is $64M_p$ (29), where M_p is the proton mass. Then the mass density of the target becomes $\rho = 5.3\,\mathrm{g/cm}^3$, close to the mass density of solid copper. Initially we set the ion charge state $Z = 3$, and electron density is set to neutralize ion charges. We placed a $4\,\mu$m preplasma in front of the target with an exponential profile of a $2\,\mu$m scale length and a $50\,n_c$ peak density for electrons when the preplasma gets fully ionized.

The ionization models include field driven ionization in low density plasmas under strong fields and impact ionization which solves for the collisional cross section in dense plasmas [51]. The electron density increases dynamically during laser irradiation via ionization processes. The ionization energies are subtracted from the hot electrons when they ionize atoms via collisions with bound electrons. Initially particles are at rest, with initial plasma temperature set to zero. Our spatial (temporal) resolution is 1/50 of the wavelength (laser oscillation period τ). The simulation also accounts for the energy loss by emission of soft x-ray radiation from free-bound transition, though it is only a minor effect (less than 0.3% of the laser energy) under the current simulation condition.

In the following, the simulation results by changing the laser

intensity, spot size and duration, while the laser energy is about constant to see the optimal condition of the γ-ray production from the given laser energy. In Figure 4.15, we show a 2D simulation using a laser pulse with an intensity $I = 10^{21}\,\mathrm{W/cm^2}$, a 66 fs pulse duration, and a $8/\sqrt{10}\,\mu$m spot where Figure 4.15(a) is the instantaneous magnetic fields [Megagauss] at 393 fs Figure 4.15(b) is the electron energy density in logarithmic scale at 393 fs and Figure 4.15(c) is the hard x-ray electron density in logarithmic scale at 132 fs. The laser pulse is irradiating from the left boundary onto the target surface. In Figure 4.15(a) strong dipole magnetic fields appear inside the target. In Figure 4.15(b) extremely energetic electrons are distributed inside the target in the form of energy density in logarithmic scale. In Figure 4.15(c) $\gamma - rays$ are transport both forward and backward direction in terms of energy density in logarithmic scale.

In Figure 4.16, we show a 2D simulation using a laser pulse with an intensity $I = 10^{22}\,\mathrm{W/cm^2}$, a 6 fs pulse duration, and a $8/\sqrt{10}\,\mu$m spot where Figure 4.16(a) is the instantaneous magnetic fields [Megagauss] at 393 fs Figure 4.16(b) is the electron energy density in logarithmic scale at 393 fs and Figure 4.16(c) is the hard x-ray electron density in logarithmic scale at 132 fs. The laser pulse is irradiating from the left boundary onto the target surface. In Figure 4.16(a) strong dipole

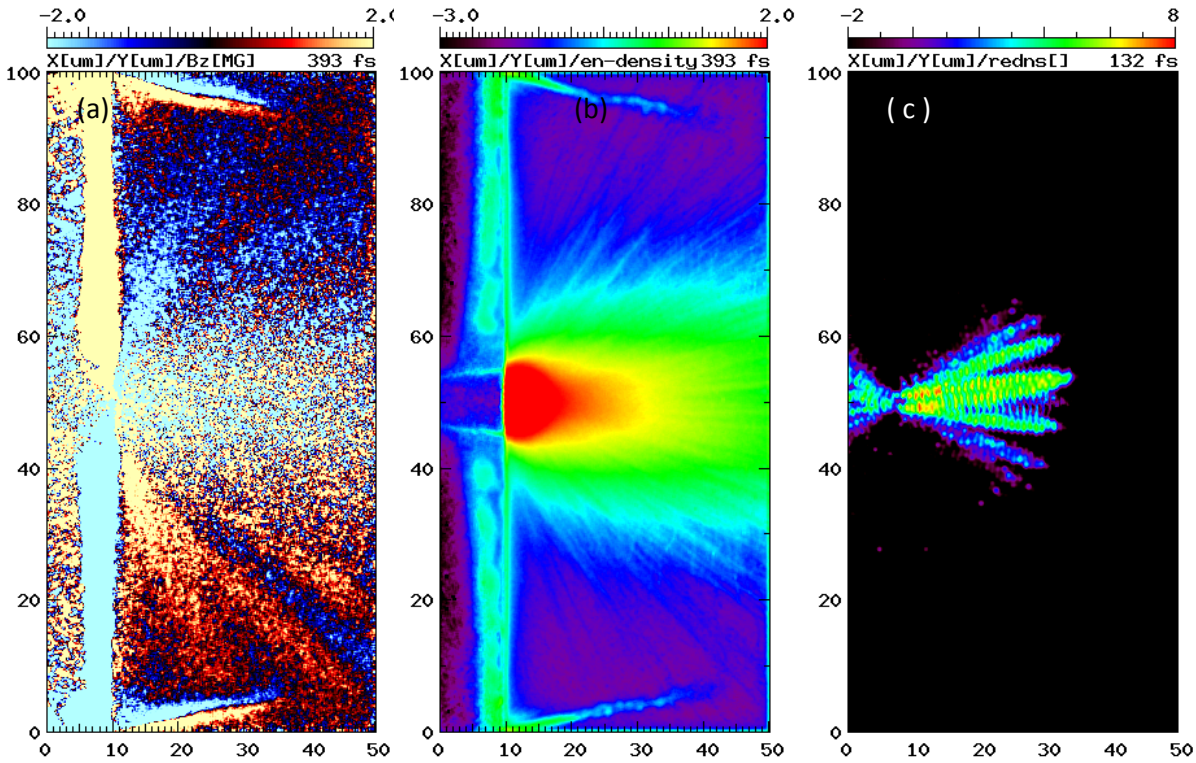

Figure 4.15: (color) 2D-PICLS results at laser intensity 10^{21} W/cm^2 of (a) instantaneous magnetic fields [Megagauss], (b) electron energy density [MeV·$n_e/100n_c$ logarithmic scale], (c) hard x-ray electron density, logarithmic scale]

magnetic fields appear inside the target. In Figure 4.16(b) extremely energetic electrons are distributed inside the target in the form of energy density in logarithmic scale. In Figure 4.16(c) γ-rays are transport both forward and backward direction in terms of energy density in logarithmic scale.

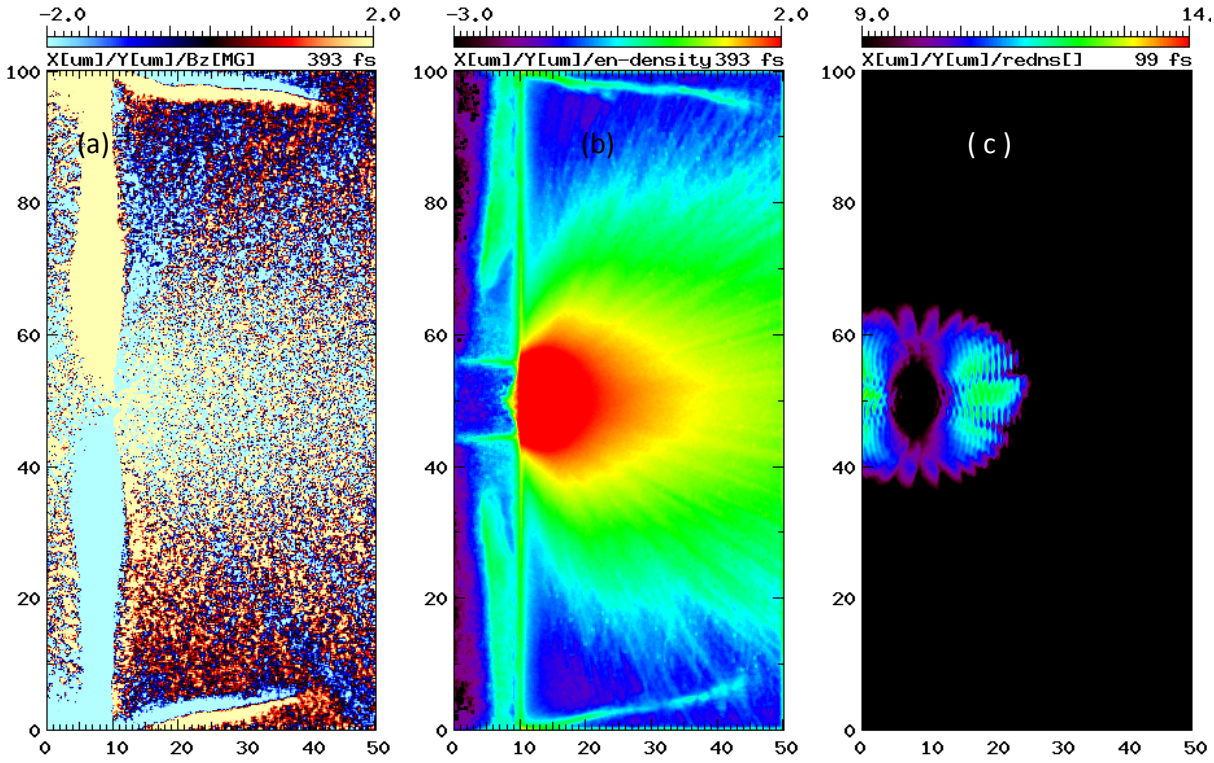

Figure 4.16: (color) 2D-PICLS results at laser intensity $10^{22}\,\mathrm{W/cm^2}$ of (a) instantaneous magnetic fields [Megagauss], (b) electron energy density [MeV$\cdot n_e/100n_c$ logarithmic scale], (c) hard x-ray electron density, logarithmic scale]

In Figure 4.17, we show a 2D simulation using a laser pulse with

an intensity $I = 10^{23}\,\mathrm{W/cm^2}$, a 6 fs pulse duration, and a 0.8 μm spot. The target is attached to the transverse boundaries, and an absorbing boundary condition is used for particles — i.e. no hot electrons are reflected back inside the target — to represent the large transverse volume of target. The laser pulse is irradiating from the left boundary onto the target surface. The pulse profile is a Gaussian distribution both temporally and radially. The surface magnetic field can be seen propagating laterally at nearly the speed of light, and also extremely strong dipole magnetic fields appearing inside the target, as seen in Fig. 4.17(a). Under such strong magnetic fields the electron cyclotron frequency exceeds $100\omega_0$, where ω_0 is the laser frequency. Because of the relativistic electron motion when $\gamma > 100$, the effective cyclotron frequency will be closer to ω_0, but the frequency will remain very high. The simulation should also have the resolution to track these cyclotron orbits. The current simulation resolution is $\tau/50$, which is sufficient to resolve the correct motion of electrons in the strong magnetic field. Interestingly, this strong magnetic buble push the plasma but they also trap extremely hot electrons inside the dipole magnetic fields as shown in above figure. The synchrotron radiation becomes significant in these regions.

The radiation efficiency via radiative damping is compared with

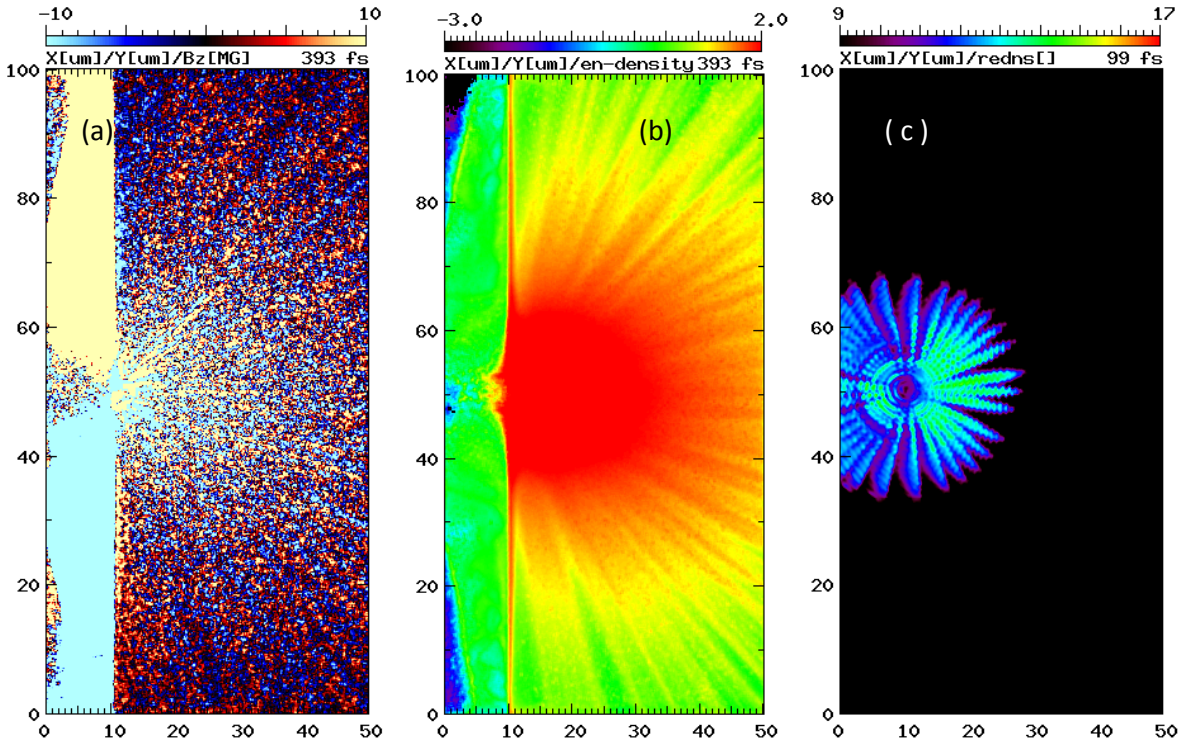

Figure 4.17: (color) 2D-PICLS results at laser intensity $10^{23}\,\mathrm{W/cm^2}$ of (a) instantaneous magnetic fields [Megagauss], (b) electron energy density [MeV·$n_e/100n_c$ logarithmic scale], (c) hard x-ray electron density, logarithmic scale]

radiations via Bremsstrahlung in the 2D simulations. The results are plotted in Figure 4.18. It was found that when laser intensity is lower than $10^{22}\,\mathrm{W/cm^2}$ hard x-rays via Bremsstrahlung are dominant. However at $I > 10^{22}\,\mathrm{W/cm^2}$, Bremsstrahlung starts to saturate and the radiative damping could become a major source of hard x-rays. This is because of electrons in the high energy tail with large γ factors were damped by radiative damping and thus cannot contribute to the Bremsstrahlung which scale as γ^4. The transition intensity is defined as the intensity at which Bremsstrahlung and the emission in radiative damping becomes the same. Above that the transition intensity radiative damping is higher than Bremsstrahlung. Note here that the radiative damping does not depend on the target material, e.g, charge state or the target thickness, while Bremsstrahlung does. The transition intensity could be multiplied by changing target condition. Having a lower Z material, a lower density or a smaller target, emission via Bremsstrahlung could be lower, resulting the transition intensity becomes lower.

These results have a strong impact on pair production by laser-matter interaction at these extreme intensities ($> 10^{22}\,\mathrm{W/cm^2}$) since we have a large energy conversion to hard x-rays via the radiative damping processes, which can boost pair production via the Bethe-Heitler pro-

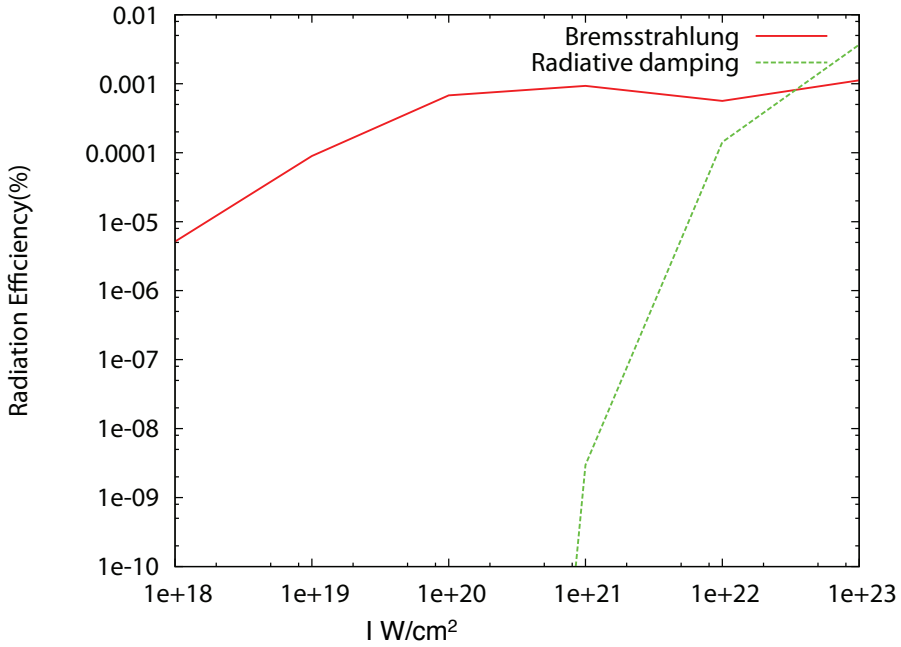

Figure 4.18: (color) 2D-PICLS results; comparing Bremsstrahlung and radiative damping in intensity vs percentage radiation efficiency graph of ultra-fast heated copper thick target.

cess [54, 68]. So, we also study and compare number of pairs produced by Bremsstrahlung and by radiative damping with different intensities by Bethe-Heitler process of ultra-fast heated copper thick target in figure 4.19. We found that from the lower intensity simulations that number of pairs per unit energy(joule) from Bremsstrahlung are dominant. However at $I > 10^{23}\,\mathrm{W/cm^2}$, number of pairs per unit energy(joule) from Bremsstrahlung start to saturate and the number of pairs per unit energy(joule) from radiative damping are dominant.

Figure 4.20 shows the phase plot of electrons when the pulse peak hits the target with the radiative damping at an intensity of (a)

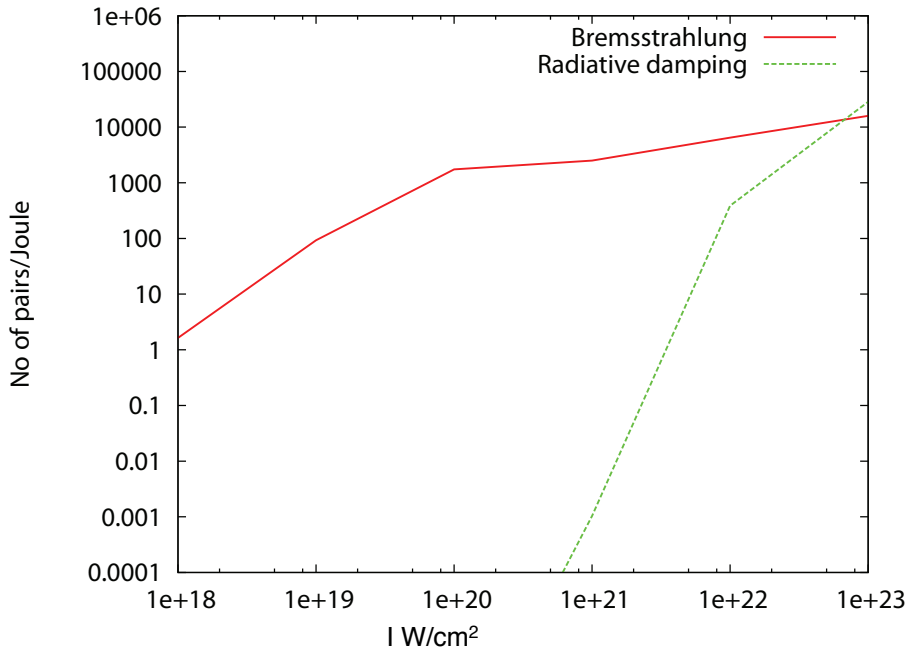

Figure 4.19: (color) 2D-PICLS results; comparing Bremsstrahlung and radiative damping in intensity vs no. of pairs per unit energy(joule) graph of ultra-fast heated copper thick target.

$I = 10^{21}\,\mathrm{W/cm^2}$, (b) $I = 10^{22}\,\mathrm{W/cm^2}$, (c) $I = 10^{23}\,\mathrm{W/cm^2}$. 2ω bunched groups of hot electrons by JxB are shown in this diagram. The oscillation is proportional to normalized laser amplitude.

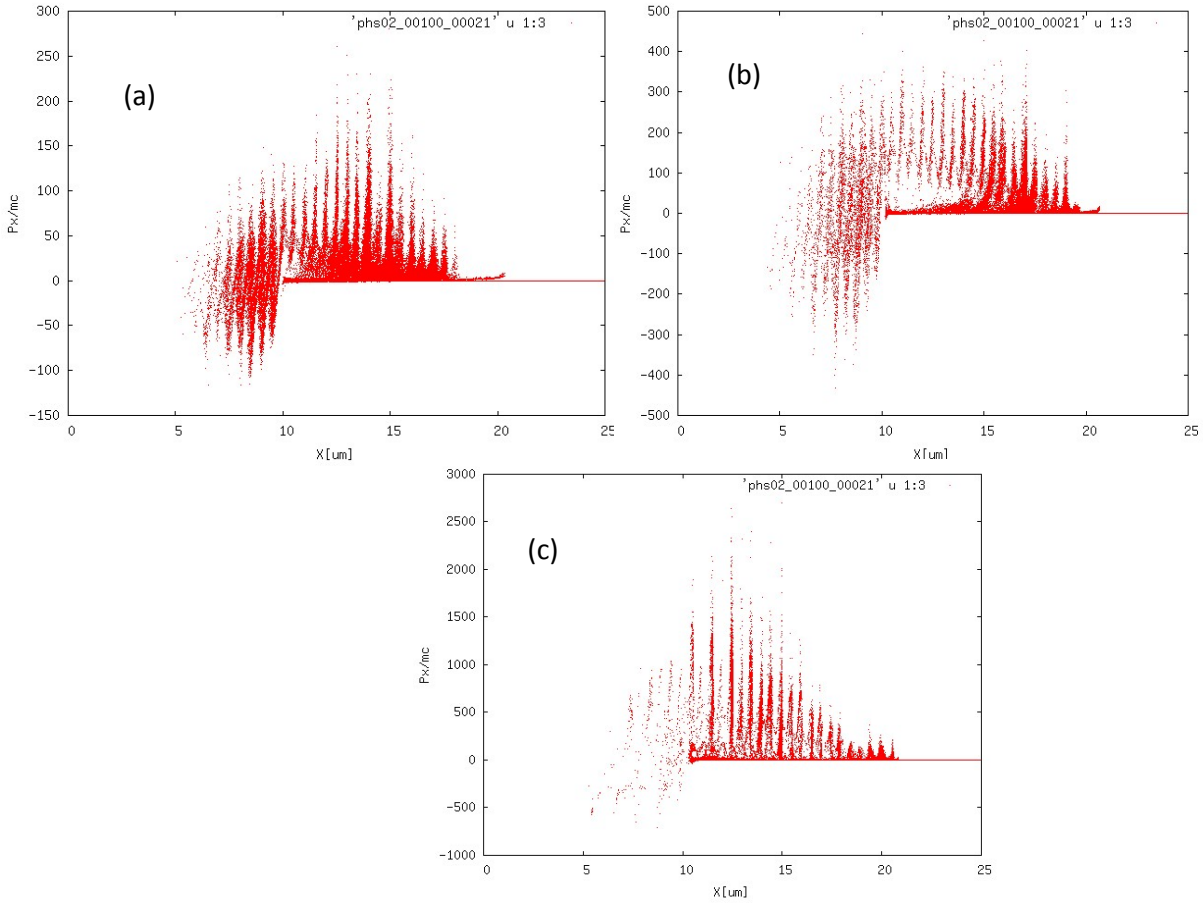

Figure 4.20: (color) 2D-PICLS results: distribution of electrons in phase space when the pulse peak hit the target at (a) $I = 10^{21}\,\mathrm{W/cm^2}$, (b) $I = 10^{22}\,\mathrm{W/cm^2}$, (c) $I = 10^{23}\,\mathrm{W/cm^2}$:

.

The plot of electron energy versus number of electrons is known as energy spectrum of electron. The electron spectrum is over plotted for each laser intensities ranging from 10^{20} W/cm^2 to 10^{23} W/cm^2 as shown in figure 4.21. As laser intensity increases, electron's energy as

well as number of electrons also increases. High energy tails of electron at intensity 10^{23} W/cm^2 is almost 1300MeV, that of electron at intensity 10^{22} W/cm^2 is almost 350 MeV, that of electron at intensity 10^{21} W/cm^2 is almost 100 MeV, that of electron at intensity 10^{20} W/cm^2 is less than 50 MeV.

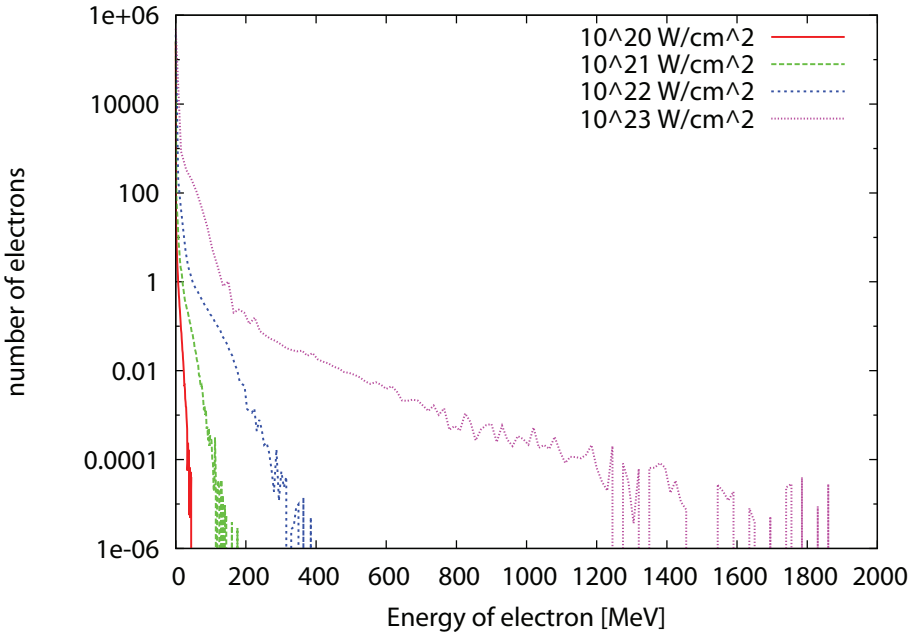

Figure 4.21: (color) 2D-PICLS results; comparing spectrum of electron with different intensities in ultra-fast heated copper thick target.

The photon spectrum with different intensities is compared in the figure 4.22. As intensity increases, photon energy also increases. High energy tail of photon spectrum at intensity 10^{21} W/cm^2 is close to 5 MeV. High energy tail of photon spectrum at intensity 10^{22} W/cm^2 is close to 200Mev. High energy tail of photon spectrum at intensity 10^{23} W/cm^2 is almost 1GeV. These high energy γ-rays are suitable for

pair production.

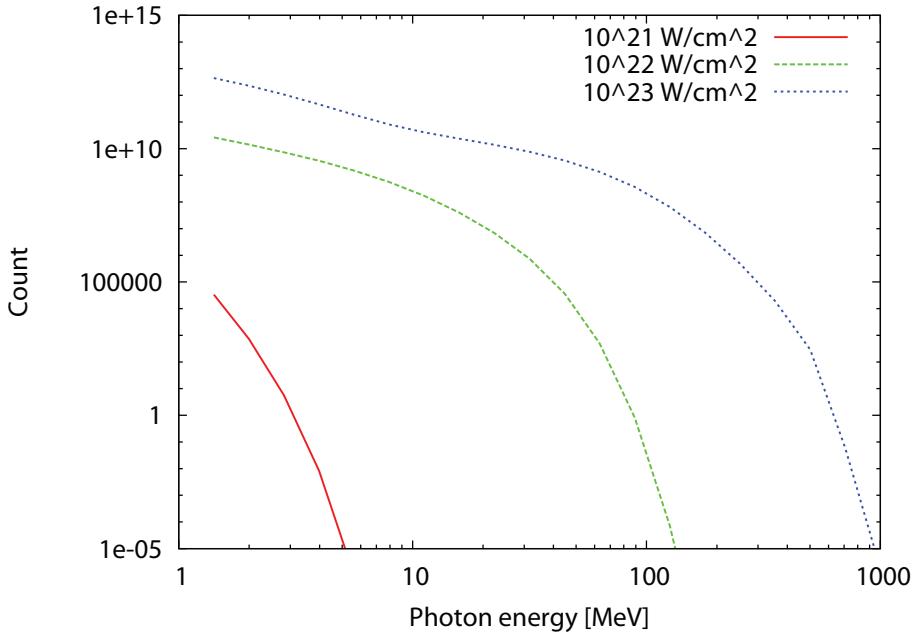

Figure 4.22: (color) 2D-PICLS results; comparing photon spectrum with different intensities of ultra-fast heated copper thick target.

Figure 4.23 shows the time history of radiation in ultra-fast heated copper thick target at intensities (a) $10^{22}\,\mathrm{W/cm^2}$ and (b) $10^{23}\,\mathrm{W/cm^2}$. Red line represents Bremsstrahlung and green line represents radiative damping. Bremsstrahlung is continuously increasing due to the reason that hot electrons continuously interact with ions even after the pulse starts to be reflected but radiative damping first increases due to strong laser fields when the main pulse hits the target. Radiative damping also increases when high energy electrons are accelerated backward by the reflected pulse.Then, radiative damping becomes constant.

Figure 4.24 shows the average ionization degree at different laser

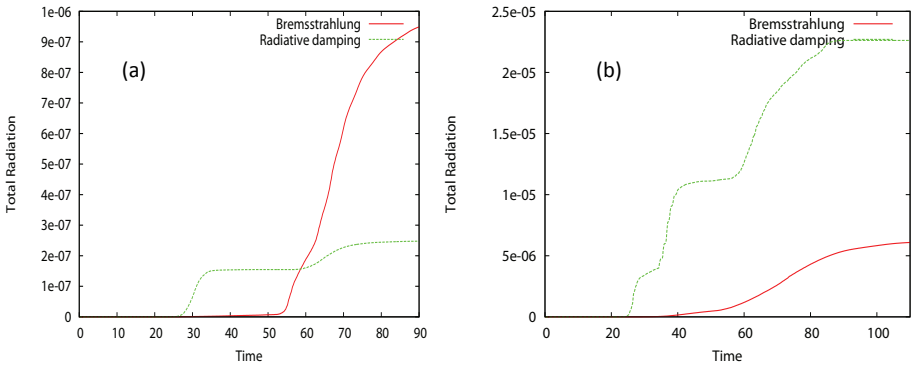

Figure 4.23: (color) 2D-PICLS results; time history of radiation in ultra-fast heated copper thick target at intensities (a) 10^{22} W/cm^2 and (b) 10^{23} W/cm^2. Unit of time is [fs]

intensities. From the figure of average ionization degree we can conclude that ionization degree increases with increase in laser intensity.

4.5.2 Absorption

When laser light is incident on the target, laser light is absorbed by the target. There are different mechanism responsible for laser light absorption. Target (type of material, density and thickness) and laser parameters determine which mechanism will dominate. Laser light is mainly absorbed by collisional absorption for low intensities such as 10^{12} W/cm^2 to 10^{17} W/cm^2 [66]. For an intense laser pulse other mecha-

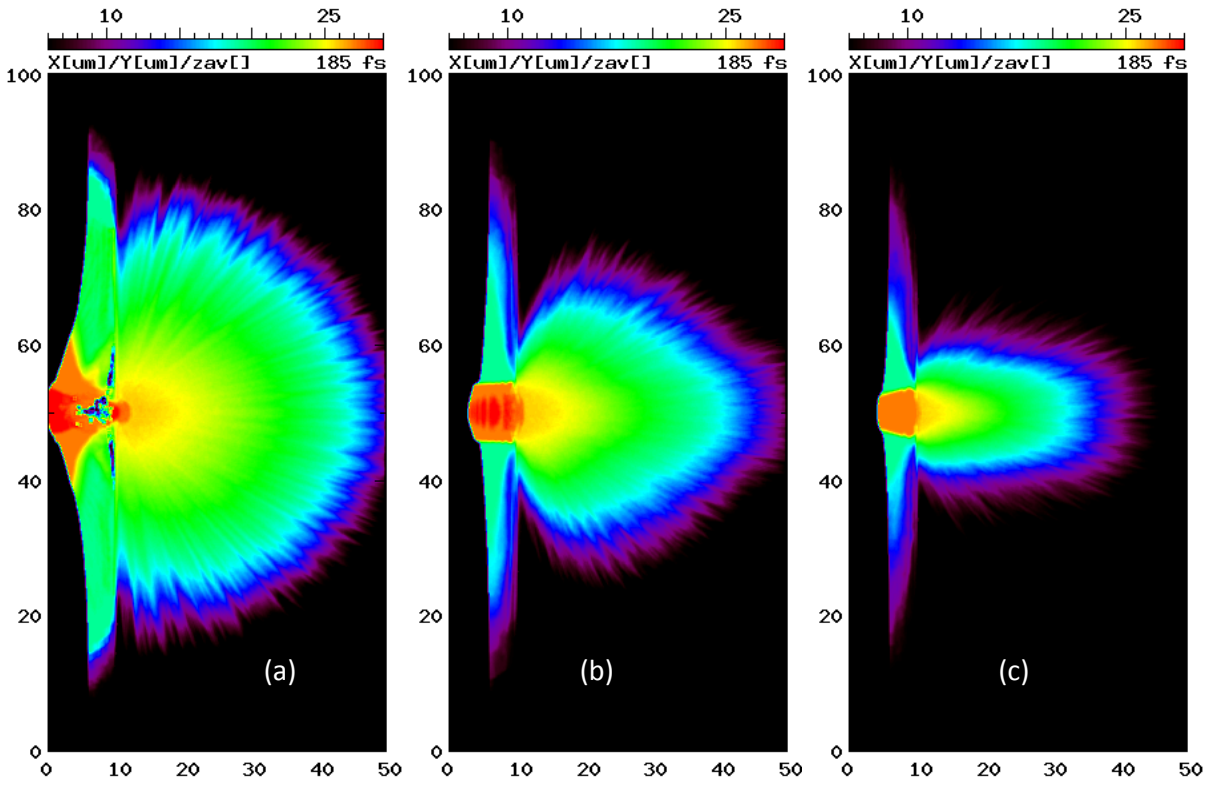

Figure 4.24: (color) 2D-PICLS results; comparing average ionization degree at (a) laser intensity $10^{23}\,\mathrm{W/cm^2}$, (b) laser intensity $10^{22}\,\mathrm{W/cm^2}$, (c) laser intensity $10^{21}\,\mathrm{W/cm^2}$ in ultra-fast heated copper thick target.

nisms (J × B Heating) dominate over collisional absorption. Collisional absorption contributes very little into total absorption of laser light for ultra intense laser plasma interaction.

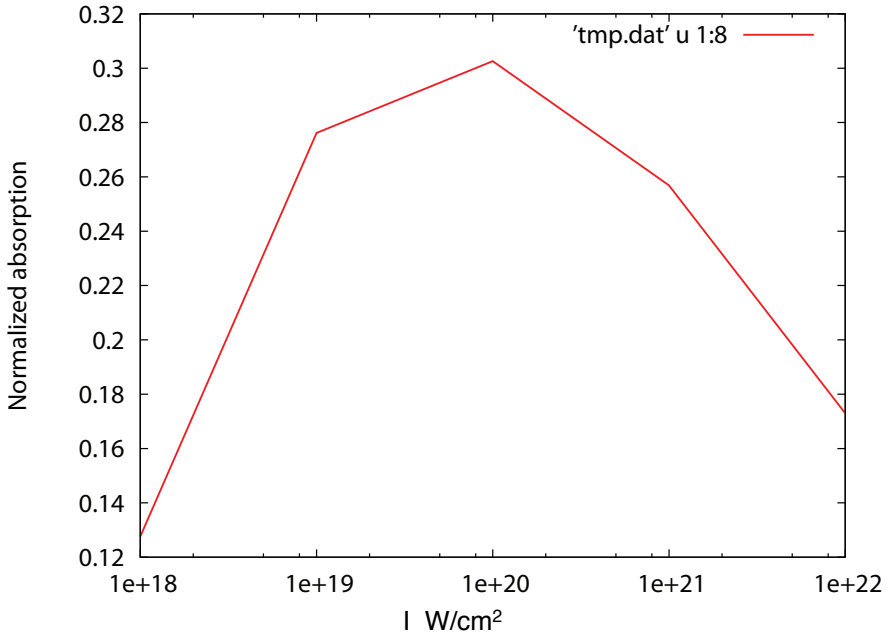

Figure 4.25: (color) 2D-PICLS results; comparing normalized absorption with different intensities in ultra-fast heated copper thick target.

Figure (4.25) shows the plot of laser intensity versus normalized absorption. This figure shows that laser energy absorption depends on intensity. Almost 13% of laser energy is absorbed by the plasma at laser intensities 10^{18} W/cm^2. Almost 27% of laser energy is absorbed by the plasma at laser intensities 10^{19} W/cm^2. Almost 30% of laser energy is absorbed by the plasma at laser intensities 10^{20} W/cm^2. Almost 26% of laser energy is absorbed by the plasma at laser intensities 10^{21} W/cm^2.

Almost 17% of laser energy is absorbed by the plasma at laser intensity 10^{22} W/cm^2. Here we see that laser energy absorption is higher at low intensities such as 10^{19}, 10^{20} W/cm^2 than that of high intensities such as 10^{21} and 10^{22}. The reason is that when the intensity is extremely high, a laser pulse directly interacts with solid density target. The laser pulse blow off the low density preplasma due to extremely high photon pressure. So, the absorption is saturated in the very high intensity regime.

4.6 Discussion and conclusion of Radiative damping

In conclusion, we have derived up to the 4th order radiative damping terms from the Lorentz-Abraham-Dirac equation by expanding the radiation terms. The second order term is found to be the damping term of the Lorentz force while the first order term represents friction in the equation of motion for the laser-matter interaction. Implementing the 2nd-order damping in PIC scheme is straightforward, by just reducing the Lorentz force by the factor given in Eq. (4.13). It was found that the 1st-order damping term is reasonable up to the intensity 10^{22} W/cm^2, however the 2nd-order term becomes non-negligible and efficiently damps higher energy electrons beyond that intensity in underdense plasmas. Because the second order term restricts electron

acceleration during the laser interaction, electrons are prevented from over-accelerating. The ion acceleration or the collision less shock formation via photon pressure at the absorption point will be overestimated at $I > 10^{23}\mathrm{W/cm^2}$ without the 2nd-order term, since it reduces the ponderomotive force. The radiation efficiency was found to increase nonlinearly for $I < 10^{22}\mathrm{W/cm^2}$ and appears to increase as I in the range of laser intensities $I > 10^{22}\,\mathrm{W/cm^2}$. Radiative damping becomes highly significant when $I \geq 10^{22}\,\mathrm{W/cm^2}$ while Bremsstrahlung emissions will saturate, thus radiative damping will be a dominant source of hard x-rays in these extreme intensity regimes.

We have also derived power radiated by 1st and 2nd order radiative damping terms including angular distribution of photons and implemented PIC code as well as radiation transport code. In angular distribution, photons are scattered both in forward direction as well as backward direction. Radiative damping does not depend on the target material, e.g. charge state or the target thickness, while Bremsstrahlung does. The transition intensity could be multiplied by changing target condition. Having a lower Z material, a lower density or a smaller target, emission via Bremsstrahlung could be lower, resulting the transition intensity becomes lower. These results have a strong impact on pair production by laser- matter interaction at these

extreme intensities ($> 10^{22}\mathrm{W/cm^2}$) since we have a large energy conversion to hard x-rays via the radiative damping as well as Bremsstrahlung processes, which can boost pair production via the Bethe-Heitler process.

Chapter 5 Summary and Discussion

In extreme intense laser-matter interaction, the radiative damping is supposedly significant, namely, electrons accelerated by the laser fields lose their energies and emit γ-rays. So that we will see intense γ-ray flash from the laser produced plasmas via two competing processes, Bremsstrahlung an radiative damping. However It is not clearly understood which process is dominant at what laser or what target conditions. My research is focusing on making the radiation models to understand the γ-ray emissions and studying the extremely intense laser-matter interaction to optimize the γ-ray emissions under the given laser and target conditions.

Since these relativistic plasmas are non-thermal and non-equilibriated, it is necessary to develop a kinetic plasma code with the radiation physics. We had developed a collisional particle-in-cell code, PICLS, which coupled to a radiation transport module to consider the γ-ray emissions. The emissivities of γ-rays had been derived for the relativistic Bremsstrahlung and the radiative damping. In the radiative damping, especially, not only the first order damping term, but up

to 4-th order damping terms had been derived from he Lorentz-Dirac equation as the first time. Especially, the 2nd term is found to be important since it is a damping term of the Lorentz force, indicating the particle acceleration including ions would be much less efficient than what we expected when the laser intensity become greater than $10^{23}\,\mathrm{W/cm^2}$.

The laser energy dependence of the γ-ray energy and the intensity dependence of the angular distribution of γ-rays are studied. By solving the emission and transport of γ-ray it was found that the radiative damping is not significant until the laser intensity exceeds $10^{23}\,\mathrm{W/cm^2}$. While the Bremsstrahlung is dominant as γ-rays emission process, which can also boost by changing the target with higher Z material or increasing the mass (volume) of the target. As an application of γ-ray production, the pair creation, forming a pair plasma, is attractive. The number of positrons via pair creation from the Bethe-Heitler process is also computed in the code. The optimal parameters of laser and target to increase γ-ray yields and positron yields are identified.

In chapter 2, we discussed about particle-in-cell simulation and radiation transport model. The PICLS implementation provides an advanced solver for many simulation aspects of directional splitting

of Maxwells equations provides a simple copy and accumulate scheme which cleanly decouples dimensions in up to 3D simulations. Particle motions are relativistically accurate. Monte Carlo collisions are relativistically accurate and provide exact energy conservation. High density plasmas are collisionally simulated without prohibitive computation requirements. In order to evaluate the effect of radiation on the laser-produced plasma development, radiation transport model coupled with a particle-in-cell code, PICLS were developed. An attenuation operator solver short-characteristics numerical scheme had been implemented in order to solve the steady-state radiation transport equation . Constrained interpolation profile (CIP) scheme for advection, Multigroup method for photon energies and SN method for direction were used.

In chapter 3, we have implemented the radiation cross-section of relativistic Bremsstrahlung to simulate γ-ray production and their transport in ultrafast heated high Z matter by an intense short pulse laser. γ-rays are produced due to the Bremsstrahlung of electrons accelerated by the intense laser on the surface. By solving the transport of γ-rays we find that high energy photons emitted by relativistic electrons are co-moving with the electrons and they are intensified continuously. As a result the γ-rays have the signature of the fast electrons

temporal and spatial distribution. In terms of angular distribution of γ-rays, most of the γ-rays are scattered hemispherically in forward direction.

In chapter 4, we have derived up to the 4th order radiative damping terms from the Lorentz-Abraham-Dirac equation by expanding the radiation terms. The second order term is found to be the damping term of the Lorentz force while the first order term represents friction in the equation of motion for the laser-matter interaction. It was found that the 1st-order damping term is reasonable up to the intensity 10^{22} W/cm^2, however the 2nd-order term becomes non-negligible and efficiently damps higher energy electrons beyond that intensity in underdense plasmas. The ion acceleration via photon pressure at the absorption point will be overestimated at $I > 10^{23}$W/cm^2 without the 2nd-order term, since it reduces the ponderomotive force. The radiation efficiency was found to increase nonlinearly for $I < 10^{22}$W/cm^2 and appears to increase as I in the range of laser intensities $I > 10^{22}\,$W/cm^2. Radiative damping becomes highly significant when $I \geq 10^{22}\,$W/cm^2 while Bremsstrahlung emissions will saturate, thus radiative damping will be a dominant source of hard x-rays at $I > 10^{23}\,$W/cm^2. We have also derived power radiated by 1st and 2nd order radiative damping terms including angular distribution of photons and implemented

PIC code as well as radiation transport code. In angular distribution, photons are scattered both in forward direction as well as backward direction. Radiative damping does not depend on the target material, e.g. charge state or the target thickness, while Bremsstrahlung does. The transition intensity could be multiplied by changing target condition. Having a lower Z material, a lower density or a smaller target, emission via Bremsstrahlung could be lower, resulting the transition intensity becomes lower.

These results have a strong impact on pair production by laser-matter interaction at these extreme intensities ($> 10^{22}\,\mathrm{W/cm^2}$) since we have a large energy conversion to hard x-rays via the radiative damping as well as Bremsstrahlung processes, which can boost pair production via the Bethe-Heitler process.

When we remove the pre-plasma, the main pulse of the laser directly interacts with the solid target and there is less absorption.

Comparing numbers and energy distribution of pair productions by trident, Bethe-Heitler and multiphoton Breit-Wheeler processes in ultra-intense laser matter interaction is the future work.

Bibliography

[1] R. Pandit and Y. Sentoku, "Effects of Radiation Damping in Extreme Ultra-intense Laser-Plasma Interaction", ProQuest, 1498698 (2011).

[2] Adapted from public domain graphic.

[3] Paul Gibbson, Short Pulse Laser Interactions with Matter: An Introduction, Imperial College Press (2005).

[4] S. Tremaine, Galactic Dynamics, (Princeton University Press,2008), second edition.

[5] David Attwood, Soft X-Rays and Extreme Ultraviolet Radiation, Cambridge University Press.

[6] H. P. Summers and R. W. P. McWhirter 1979 J. Phys. B: At. Mol. Phys. 12 2387

[7] D. Duston and J. Davis, Phys. Rev. A 23, 2602 (1981)

[8] M. Lamoureux and N. Avdonina, Phys. Rev. E 55, 912 (1997)

[9] D. Mihalas and B. W. Mihalas, Foundations of radiation hydrodynamics, Dover Publications Inc., Mineola, New York, 1999

[10] H. K. Chung et al., High Energy Density Physics **1** (2005) 3-12.

[11] W. J. Karzas and R. Latter, Astrophysical Journal Supplement **6**, 167 (1961)

[12] A. Zhidkov, J. Koga, A. Sasaki, M. Uesaka, Phys. Rev. Lett. **88**, 185002 (2002).

[13] K. B. Wharton, S. P. Hatchett, S. C. Wilks, M. H. Key, J. D. Moody, V. Yanovsky, A. A. Offenberg, B. A. Hammel, M. D. Perry, and C. Joshi, Phys. Rev. Lett. 81, 822 (1998).

[14] Y. Sentoku, K. Mima, S. Kojima, and H. Ruhl, Phys. plasmas 7, (2000).

[15] G. Bonnaud, P. Gibbon, J. Kindel, and E. Williams, Laser Part. Beams 9, 331 (1991).

[16] S. Kato, B. Bhattacharyya, A. Nishiguchi, and K. Mima, Phys. Fluids B 5, 564 (1993).

[17] Q. L. Dong, J. Zheng, and H. Teng, T. J. Liang, L. Z. Zhao, and Z.Y. Wei, Phys. Plasmas 8, 2925 (2001).

[18] High Energy Density Physics, National Report.

[19] Y. Sentoku, W. Kruer, M. Matsuoka, A. Pukhov, Fusion Science and Technology, vol. 49 APR. 2006.

[20] C. L. Birdsall and A. B. Langdon, "Plasma Physics Via Computer Simulation", McGraw, (1985).

[21] R. Shanny, J. M. Dawson, and J. M. Greene, One-Dimensional Model of a Lorentz Plasma, Phys. Fluids **10**, 6, 1281 (1967)

[22] T. Takizuka and H. Abe, A binary collision model for plasma simulation with a particle code, J. Comput. Phys., **25**, 205 (1977).

[23] Y. Sentoku, K. Mima, Y. Kishimoto and M. Honda, Magnetic instability by the relativistic laser pulses in overdense plasmas, J. Phys. Soc. Japan, **67**, 4084 (1998).

[24] R. H. Miller, M. R. Combi, A Coulomb Collision Algorithm for Weighted Particle Simulations, Geophys. Res. Lett. 21, 1735 (1994).

[25] K. Nambu, S. Yonemura, Weighted particles in Coulomb collision simulations based on the theory of a cumulative scattering angle, J. Comput. Phys., **145**, 639 (1998).

[26] J. A. Elliot, *Plasma kinetic theory* (1993)

[27] D. Mihalas, W. H. Freeman and Co., *Stellar Atmospheres* Second

Edition, ISBN 071670359 9, (1978).

[28] P. Kunasz and L. H. Auer, J. Quant. Spectrosc. Radiat. Transfer 39, 67 (1988)

[29] M. van Noort, I. Hubeny and T. Lanz, ApJ 568, 1066 (2002)

[30] C. E. Lee, Los Alamos Scientific Laboratory Report LA-2595 (1962).

[31] T. Yabe, et al., Computer Physics Communications **66**, 233 (1991)

[32] F. Xiao et al., Comput. Phys. Commun. **93**, 1 (1996)

[33] F. Xiao et al., Comput. Phys. Commun. **94**, 103 (1996).

[34] H. K. Chung, M. H. Chen, W. L. Morgan, Y. Ralchenko, HEDP 1, 3 (2005)

[35] J. D. Kmetec, C. L. Gordon, III, J. J. Macklin, B. E. Lemoff, G. S. Brown, and S. E. Harris, Phys. Rev. Lett. **68**, 1527 (1992)

[36] M. Schnurer, M. P. Kalashnikov, P. V. Nickles, Th. Schlegel, and W. Sandner, Phys. Plasmas **2**, 3106 (1995).

[37] F. N. Beg, A. R. Bell, A. E. Dangor, C. N. Danson, A. P. Fews, M. E. Glinsky, B. A. Hammel, P. Lee, P. A. Norreys, and M. Tatarakis, Phys. Plasmas **4**, 447 (1997).

[38] S. C. Wilks, W. L. Kruer, M. Tabak, and A. B. Langdon, Phys. Rev. Lett. **69**, 1383 (1992).

[39] F. Brunel, Phys. Rev. Lett. **59**, 52 (1987).

[40] P. Gibbon, Phys. Rev. Lett. **73**, 667 (1994).

[41] A. R. Bell, J. R. Davis, S. Guerin, and H. Ruhl, Plasma Phys. Controlled Fusion **39**, 653 (1997).

[42] J. D. Jackson, *Classical Electrodynamics* (Wiley, New York, 1999)

[43] K. Nakashima and H. Takabe, Phys. Plasmas **9**, 5 (2002)

[44] C. P. Ridgers et al., Phys. Rev. Lett. **108**, 165006 (2012).

[45] V. I. Ritus, J. Russ. Laser Res. **6**, 497 (1985)

[46] J. G. Kirk, A. R. Bell and I. Arka, Plasma Phys. Controlled Fusion **51**, 085008 (2009).

[47] T. Erber, Rev. Mod. Phys. **38**, 626 (1966).

[48] J. H. Hubbell et al., J. Phys. Chem. Ref. Data **9**, 4 (1980)

[49] L. C. Maximon, J. Res. Natl. Bur. Stand., Sect. B, 72, 79-88 (1968)

[50] Y. Sentoku, and A. J. Kemp, J. Comput. Phys. **227**, 6846 (2008).

[51] W. Lotz, Z. Physik **232**, 101 (1970).

[52] M. Nakatsutsumi, A. Kon, S. Buffechoux, P. Audebert, J. Fuchs, R. Kodama, Opt. Lett. **35**, 2314 (2010).

[53] L. D. Landau and E. M. Lifshits, *The Classical Theory of Fields* (Pergamon, New York, 1994).

[54] A. R. Bell and J. G. Kirk, Phys. Rev. Lett. **101**, 200403 (2008).

[55] I. V. Sokolov, N. M. Naumova, J. A. Nees, G. A. Mourou, V. P. Yanovsky, Phys. Plasmas **16**, 093115 (2009).

[56] I. V. Sokolov, J. Exp. Theor. Phys. **109**, 207 (2009).

[57] G. W. Ford and R. F. O'Connell, Phys. Lett. A **174**, 182 (1993).

[58] R. Capdessus, E. d'Humieres, and V. T. Tikhonchuk, Phys. Rev. E **86**, 036401 (2012)

[59] S. V. Bulanov, T. Zh. Esirkepov, M. Kando, J. K. Koga, S. S. Bulanov, Phys. Rev. E **84**, 056605 (2011)

[60] J. Koga, Phys. Rev. E **70**, 046502 (2004).

[61] I. V. Sokolov et al., Phys. Plasmas **18**, 093109 (2011)

[62] R. R. Pandit and Y. Sentoku, Phys. Plasmas **19**, 073304 (2012)

[63] Y. Sentoku, E. dHumie‘res, L. Romagnani, P. Audebert, and J. Fuchs, Phys. Rev. Lett. **107**, 135005 (2011).

[64] A. J. Kemp, Y. Sentoku, and M. Tabak, Phys. Rev. Lett. **101**, 075004 (2008).

[65] I. V. Sokolov, N. M. Naumova, and J. A. Nees, Phys. Plasmas **18**, 093109 (2011).

[66] J. Kupersztych, M. Raynaud, and C. Riconda, Phys. Plasma 11, 1669 (2004)

[67] Y. Sentoku, K. Mima, T. Taguchi, S. Miyamoto, Y. Kishimoto, Phys. Plasmas **5**, 4366 (1998).

[68] Hui Chen, S. C. Wilks, D. D. Meyerhofer, J. Bonile, C. D. Chen, S. N. Chen, C. Courtois, L. Elberson, G. Gregori, W. Kruer, O. Landoas, J. Mithen, J. Myatt, C. D. Murphy, P. Nilson, D. Price, M. Schneider, R. Shepherd, C. Stoeckl, M. Tabak, R. Tommasini, and P. Beiersdorfer, Phys. Rev. Lett. **105**, 015003 (2010).

[69] A. G. R. Thomas et al., Phys. Rev. X **2**, 041004 (2012).

[70] C. P. Ridgers et al., Journal of computational physics **260** (2014) 273-285

[71] T. G. Blackburn et al., Phys. Rev. Lett. **112**, 015001 (2014).

[72] J. D. Jackson, Classical Electrodynamics, p3 (1998).

[73] J. Villasenor and O. Buneman, Rigorous charge conservation for

local electromagnetic field solvers, Comput. Phys. Comm., 69, (1992).

Publications

- R. Pandit and Y. Sentoku, Higher Order Terms of Radiative Damping in Extreme Intense Laser-Matter Interaction, Physics of Plasmas 19, 073304 (2012).
- H. Sawada, Y. Sentoku, R. Pandit, F. Beg, H. Chen, P. K. Patel et al., Characterization of intense laser-produced fast electrons using hard x-rays via bremsstrahlung, Journal of Physics B: At.Mol.Opt.Phys. (Manuscript Submitted).

Presentations

- R. Pandit, Y. Sentoku, Numerical modeling of radiation physics in kinetic plasmas [III] - gamma-ray transport via Bremsstrahlung in ultra-fast heated high Z matter, 56th Annual Meeting of the APS Division of Plasma Physics, New Orleans, Louisiana, October 27-October 31, 2014.
- R. Pandit, Y. Sentoku, Spectrum and angular distribution of γ-rays from radiative damping in extremely relativistic laser-plasma interaction, 55th Annual Meeting of the APS Division of Plasma Physics, Denver, CO, Nov 11- Nov 15, 2013.
- R. Pandit, Y. Sentoku, Spectral and Angular Distribution of Photons via Radiative Damping in Super Intense Laser-Matter Interaction, 54th Annual Meeting of the APS Division of Plasma Physics, Providence, RI, Oct 29 - Nov 2, 2012.
- R. Pandit, Y. Sentoku, Effects of radiation damping in extreme ultra-intense laser-plasma interaction, 53rd Annual Meeting of the American Physical Society Division of Plasma Physics, Salt Lake City, UT, November 14-18, 2011.
- Y. Sentoku, R. Pandit, Effects of radiation damping in ultra-intense laser matter interaction at extreme intensity regime, 53rd An-

nual Meeting of the American Physical Society Division of Plasma Physics, Salt Lake City, UT, November 14-18, 2011.

- R. Pandit, Y. Sentoku, Spectral and Angular Distribution of Photons via Radiative Damping in Super Intense Laser-Matter Interaction, Invited talk, RHEDP Conference, April 2 - 5, 2013, South Lake Tahoe, NV.

- Y. Sentoku, R. Pandit, R. Royle, I. Paraschiv, R. Mancini, Numerical modeling of radiation physics in kinetic plasmas [I] - overview and introduction of radiation transport in PIC, 56th Annual Meeting of the APS Division of Plasma Physics, New Orleans, Louisiana, October 27- October 31, 2014.

- R. Pandit, Y. Sentoku, γ-ray production and transport in ultrafast heated high Z matter, American Physical Society Far West Section meeting, Reno, NV, October 23- October 25, 2014.

APPENDIX A

In chapter 4, explicit expressions for the spatial part of the damping force for both 1st and 2nd order are written directly from the equation of motion of the radiating electron in four-dimensional form. But for the benefit of the reader, it is better to expand the full derivations of the spatial part of the damping force. So, in this appendix, equations (4.12) and (4.13) are derived by taking equations (4.4) and (4.5).

The *i-th* component of the four velocity u^i is

$$u^i = \begin{bmatrix} \gamma \\ \beta_x\gamma \\ \beta_y\gamma \\ \beta_z\gamma \end{bmatrix}$$

Where, relativistic factors β and γ are $\beta = \frac{v}{c}$ and $\gamma = \frac{1}{\sqrt{1-\beta^2}}$. Here, v is the velocity of the particle and c is the speed of light.

The electromagnetic field tensor F^{ik} is

$$F^{ik} = \begin{bmatrix} 0 & -E_x & -E_y & -E_z \\ E_x & 0 & -B_z & B_y \\ E_y & B_z & 0 & -B_x \\ E_z & -B_y & B_x & 0 \end{bmatrix}$$

In the general rule of tensors, raising or lowering a space index

changes the sign of the component, while raising or lowering the time index does not.

u_i and F_{ik} are the covariant forms of tensors u^i and F^{ik} respectively.

$F_{ik} = (E, B)$ and $F^{ik} = (-E, B)$, E is the electric field and B is the magnetic field.

There are several ways to solve equations (4.4) and (4.5) which lead to the description of the damping of a relativistic electron interacting with an electromagnetic fields. One of the methods is to re-express the damping term in terms of the fields which can be done through a perturbation expansion. Let us suppose that the damping term g^i is a small perturbation, then the zeroth order term of the acceleration is equation (4.6). Then equation(4.4) becomes

$$\left(\frac{du^i}{ds}\right)_1 = \left(\frac{du^i}{ds}\right)_0 + \frac{2e^2}{3mc^2}\, g_1^i \qquad \text{(A-1)}$$

where

$$g_1^i = \left[\left(\frac{d^2u^i}{ds^2}\right)_0 - u^i u^k \left(\frac{d^2u_k}{ds^2}\right)_0\right] \qquad \text{(A-2)}$$

Here the subscript 0 and 1 refer to the zeroth and first order terms respectively.

Again, the zeroth order acceleration is

$$\left(\frac{du^i}{ds}\right)_0 = \frac{e}{mc^2}\ F^{ik}u_k \tag{A-3}$$

The spatial part of the product of F^{ik} and u_k is

$$F^{ik}u_k = \gamma(\mathbf{E} + \boldsymbol{\beta} \times \mathbf{B}) \tag{A-4}$$

Differentiating equation (A-3) with respect to s, we then get

$$\left(\frac{d^2u^i}{ds^2}\right)_0 = \frac{e}{mc^2}\frac{\partial F^{ik}}{\partial x^l}\ u_k u^l\ + \frac{e^2}{m^2c^4}\ F^{ik}F_{kl}u^l\ . \tag{A-5}$$

Substituting the value of $\left(\frac{d^2u^i}{ds^2}\right)_0$ from equation (A-5) into equation (A-2) and keeping in mind that the product of the tensor $\frac{\partial F_{ik}}{\partial x^l}$ which is antisymmetric in the indices i, k, and the symmetric tensor u^iu^k is exactly zero. So,

$$g_1^i\ = \left[\frac{e}{mc^2}\frac{\partial F^{ik}}{\partial x^l}\ u_k u^l\ + \frac{e^2}{m^2c^4}\ F^{ik}F_{kl}u^l\ - \frac{e^2}{m^2c^4}\left(\ F^{ml}u_l\right)\left(F_{km}u^k\right)u^i\ \right]. \tag{A-6}$$

The explicit expression for the spatial part of equation (A-6) is equation (4.12). Similarly, we can derive the second order damping term,

$$\left(\frac{du^i}{ds}\right)_2 = \left(\frac{du^i}{ds}\right)_1 + \frac{2e^2}{3mc^2}\ g_2^i \tag{A-7}$$

where

$$g_2^i\ = \left[\left(\frac{d^2u^i}{ds^2}\right)_1 -\ u^iu^k\ \left(\frac{d^2u_k}{ds^2}\right)_1\right] \tag{A-8}$$

Differentiating equation (A-1) with respect to s by taking only the first order term, we then get

$$\begin{aligned}\left(\frac{d^2u^i}{ds^2}\right)_1 \;=\; & \left(\frac{2e^2}{3mc^2}\right)\Big[\frac{e}{mc^2}\frac{\partial^2F^{ik}}{\partial x^l\partial x^l}\;u_ku^lu^l \\ & +\Big(\frac{e}{mc^2}\Big)^2\frac{\partial F^{ik}}{\partial x^l}\;u^l\;\;F_{km}u^m\;+\Big(\frac{e}{mc^2}\Big)^2\frac{\partial F^{ik}}{\partial x^l}\;u^l\;\;F_{kl}u^l \\ & +\Big(\frac{e}{mc^2}\Big)^2\frac{\partial F_{kl}}{\partial x^i}\;u^l\;\;F^{ik}u^i\;+\Big(\frac{e}{mc^2}\Big)^3\;F^{ik}F_{kl}F^{lm}u_m \\ & -\Big(\frac{e}{mc^2}\Big)^2\frac{\partial F_{km}}{\partial x^l}\;u^lu^k\;\;F^{ml}u_lu^i\;-\Big(\frac{e}{mc^2}\Big)^3\;F^{km}F_{km}F^{ml}u_mu_lu^i \\ & -\Big(\frac{e}{mc^2}\Big)^2\frac{\partial F^{ml}}{\partial x^k}\;u^iu^k\;\;F_{km}u_lu^k\;-\Big(\frac{e}{mc^2}\Big)^3\;F_{km}F^{ml}F_{lm}u^mu^ku^i \\ & -\Big(\frac{e}{mc^2}\Big)^3\;F_{km}F^{ml}F^{ik}u_ku_lu^k\;\Big] \qquad (\mathrm{A}-9)\end{aligned}$$

Substituting the value of $\left(\frac{d^2u^i}{ds^2}\right)_1$ from equation (A-9) into equation (A-8) and keeping in mind that the product of the tensor $\frac{\partial F_{ik}}{\partial x^l}$ which is antisymmetric in the indices i, k, and the symmetric tensor u^iu^k is also exactly zero. So,

$$
\begin{aligned}
g_2^i \;=\; & \left(\frac{2e^2}{3mc^2}\right)\Big[\frac{e}{mc^2}\frac{\partial^2 F^{ik}}{\partial x^l \partial x^l}\; u_k u^l u^l \\
& + \Big(\frac{e}{mc^2}\Big)^2 \frac{\partial F^{ik}}{\partial x^l}\; u^l \;\; F_{km}u^m \;+ \Big(\frac{e}{mc^2}\Big)^2 \frac{\partial F^{ik}}{\partial x^l}\; u^l \;\; F_{kl}u^l \\
& + \Big(\frac{e}{mc^2}\Big)^2 \frac{\partial F_{kl}}{\partial x^i}\; u^l \;\; F^{ik}u^i \;+ \Big(\frac{e}{mc^2}\Big)^3 \;\; F^{ik}F_{kl}F^{lm}u_m \\
& - \Big(\frac{e}{mc^2}\Big)^2 \frac{\partial F_{km}}{\partial x^l}\; u^l u^k \;\; F^{ml}u_l u^i \;- \Big(\frac{e}{mc^2}\Big)^3 \;\; F^{km}F_{km}F^{ml}u_m u_l u^i \\
& - \Big(\frac{e}{mc^2}\Big)^2 \frac{\partial F^{ml}}{\partial x^k}\; u^i u^k \;\; F_{km}u_l u^k \;- \Big(\frac{e}{mc^2}\Big)^3 \;\; F_{km}F^{ml}F_{lm}u^m u^k u^i \\
& - \Big(\frac{e}{mc^2}\Big)^3 \;\; F_{km}F^{ml}F^{ik}u_k u_l u^k \;- \Big(\frac{e}{mc^2}\Big)^2 \frac{\partial F^{ik}}{\partial x^l}\; u^i u^k \;\; F_{ki}u^l u_k \\
& - \Big(\frac{e}{mc^2}\Big)^3 \;\; F_{ki}F^{ik}F_{ki}u^i u^i u^k \;+ \Big(\frac{e}{mc^2}\Big)^3 \;\; (F^{ik}u_k)(F_{kl}u^k)(F^{li}u_i)u_i u^i \\
& + \Big(\frac{e}{mc^2}\Big)^3 \;\; (F^{ik}u_k)(F_{kl}u^l)(F_{ik}u^k)u^i u^k \\
& + \Big(\frac{e}{mc^2}\Big)^3 \;\; (F_{kl}u^l)(F^{ik}u_i)(F_{ki}u^i)u^i u^k \;\Big] \qquad (\mathrm{A}-10)
\end{aligned}
$$

Expressing the equation (A-10) in terms of space components only leads to some groups of terms canceling out. The remaining group of terms result in equation (4.13). To derive the 3rd order terms, we only used the last terms in equation (A-10).